UNIVERSITY OF CALIFORNIA
SANTA CRUZ

SEARCH FOR SUPERSYMMETRY USING A PHOTON, B-JETS, AND $E_{\mathrm{T}}^{\mathrm{miss}}$ FINAL STATE WITH THE ATLAS DETECTOR IN PROTON-PROTON COLLISIONS AT 8 TEV CENTER-OF-MASS ENERGY

A dissertation submitted in partial satisfaction of the
requirements for the degree of

DOCTOR OF PHILOSOPHY

in

PHYSICS

by

Andrew David Kuhl

March 2015

The Dissertation of Andrew David Kuhl
is approved:

Professor Jason Nielsen, Chair

Professor Bruce Schumm

Professor Abraham Seiden

Dean Tyrus Miller
Vice Provost and Dean of Graduate Studies

Table of Contents

List of Figures vii

List of Tables x

Abstract xii

Dedication xiv

Acknowledgments xv

I Theoretical Motivation 1

1 Introduction 2

2 The Standard Model 6
2.1 Fermions . . . 6
2.2 Gauge Bosons . . . 8
2.3 Higgs Boson . . . 9
2.4 Standard Model Limitations . . . 10
2.4.1 Dark Matter . . . 11
2.4.2 Hierarchy Problem . . . 11

3 Supersymmetry 13
3.1 The Minimal Supersymmetric Model . . . 13
3.2 Superpartner Naming Conventions . . . 16
3.3 Neutralino Mixing . . . 18
3.4 R-Parity . . . 19
3.5 Gauge-Mediated Supersymmetry Breaking . . . 20
3.6 Photon + b + $E_{\mathrm{T}}^{\mathrm{miss}}$ Phenomenology in GGM . . . 21

4 Previous Results 26
4.1 ATLAS 7 TeV Result . . . 26

II Experimental Setup **29**

5 The Large Hadron Collider **30**
5.1 LHC design . . . 31
5.1.1 Injection System . . . 32
5.1.2 LHC Experiments . . . 32
5.1.3 Magnet Quenching Incident . . . 34
5.2 LHC Performance . . . 34

6 The ATLAS Detector **36**
6.1 Inner Detector . . . 39
6.1.1 Pixel Detector . . . 40
6.1.2 Semiconductor Tracker (SCT) . . . 42
6.1.3 Transition Radiation Tracker (TRT) . . . 43
6.2 Calorimeters . . . 44
6.2.1 Electromagnetic Calorimeter . . . 46
6.2.2 Hadronic Calorimeter . . . 48
6.3 Muon Spectrometer . . . 49
6.4 Magnet Systems . . . 51
6.4.1 Central Solenoid . . . 51
6.4.2 Toroidal Magnets . . . 51
6.5 Luminosity Calculation . . . 52
6.6 Trigger System . . . 53

III The Analysis **56**

7 Data and Monte Carlo Samples **57**
7.1 Dataset and Trigger Studies . . . 57
7.2 Monte Carlo simulated samples . . . 60
7.2.1 Background Simulation . . . 61
7.2.2 Signal Simulation . . . 71

8 Object Selection **77**
8.1 Jets . . . 77
8.2 *b*-tagging . . . 79
8.3 Photons . . . 79
8.4 Leptons . . . 81
8.5 Missing transverse momentum . . . 81
8.6 Total Transverse Energy . . . 82
8.7 Overlap removal . . . 82

9 Event Selection and Optimization **84**
9.1 Signal region definitions . . . 84
9.2 Optimization . . . 90
9.2.1 Photon p_{T} cut . . . 91
9.2.2 Number of jets in the event . . . 92
9.2.3 b-tag requirement . . . 92
9.2.4 Lepton veto . . . 95
9.2.5 $E_{\mathrm{T}}^{\mathrm{miss}}$ cut . . . 96
9.2.6 $M_{\mathrm{T}}^{\gamma,E_{\mathrm{T}}^{\mathrm{miss}}}$ cut . . . 96
9.2.7 $E_{\mathrm{T}}^{\mathrm{miss}}$ isolation cut . . . 97
9.2.8 $M_{b\bar{b}}$ cut . . . 98
9.2.9 H_{T} cut . . . 99

10 The Background Model **101**
10.1 Background Estimations . . . 101
10.1.1 General properties of $t\bar{t}$ and $W+\gamma$/jets background . . . 101
10.1.2 Processes containing $W \to l\nu$ in which an electron fakes a γ . . . 102
10.1.3 Background containing $W \to l\nu$ processes with prompt photon and jets faking a photon. . . . 117
10.1.4 QCD Events . . . 125
10.1.5 $Z \to \nu\nu$ background . . . 131
10.1.6 Total backgrounds . . . 131
10.2 Validation Regions . . . 132

11 Systematic Uncertainties **143**
11.1 Experimental Uncertainties . . . 143
11.1.1 Experimental signal uncertainties . . . 145
11.1.2 Experimental background uncertainties . . . 148
11.2 Theoretical Uncertainties . . . 149

12 Results and Interpretation **152**
12.1 Summary of background predictions and observed data events . . . 152
12.2 Interpretation . . . 155
12.2.1 Limit Setting Formalism . . . 155
12.2.2 Upper Limit on the Number of Non-SM Events . . . 157
12.2.3 GGM Mass Exclusion Limits . . . 158
12.3 Conclusion . . . 166

Bibliography **167**

IV Appendices **177**

A Monte Carlo Sample Details **178**

B Signal Contamination **183**
B.1 Signal contamination in the lepton control region 183
B.2 Signal contamination in the QCD CR3 control region 185

C Theory Systematic Uncertainties **187**
C.1 $t\bar{t}$ +γ 188
C.2 W+γ 190

List of Figures

3.1 Branching ratios of NLSP neutralino to SM bosons 23
3.2 Feynman diagrams for $\gamma + b\bar{b}+E_{\mathrm{T}}^{\mathrm{miss}}$ final state 25

4.1 $E_{\mathrm{T}}^{\mathrm{miss}}$ distribution for 7 TeV signal region 28
4.2 7 TeV gluino and squark grid limits 28

5.1 LHC ring schematic 33
5.2 Instantaneous and integrated luminosity of 8 TeV run 35

6.1 Computer-generated image of ATLAS detector with dimensions 37
6.2 Cutaway and radial views of the ATLAS inner detector 40
6.3 Cross section of r-z plane of the ATLAS inner detector 41
6.4 Cutaway view of the ATLAS calorimeter system 45
6.5 Schematic of the sampling layers of LAr calorimeter 47
6.6 Cutaway view of the ATLAS muon system 50

7.1 Trigger efficiency in data 59
7.2 Trigger efficiency in MC 59
7.3 Photon p_{T} comparison $t\bar{t}$ vs. $t\bar{t}$ $+\gamma$ 63
7.4 Photon p_{T} comparison single top vs. single top + γ 65
7.5 Photon p_{T} comparison W vs. $W\gamma$ 67
7.6 Signal cross sections by production mechanism 74
7.7 Total signal production cross sections 74

9.1 p_{T}^{γ} optimization histograms 91
9.2 N_{jets} SRL optimization histograms 92
9.3 N_{jets} SRH optimization histogram 93
9.4 Single b-tag optimization histograms 94
9.5 Double b-tag optimization histograms 94
9.6 N_{leps} optimization histograms 95
9.7 $E_{\mathrm{T}}^{\mathrm{miss}}$ optimization histograms 96
9.8 $M_{\mathrm{T}}^{\gamma,E_{\mathrm{T}}^{\mathrm{miss}}}$ optimization histograms 97

9.9 $E_{\mathrm{T}}^{\mathrm{miss}}$ isolation optimization histograms . . . 98
9.10 $M_{b\bar{b}}$ optimization histograms . . . 99
9.11 H_{T} optimization histograms . . . 100

10.1 ee invariant mass distribution . . . 107
10.2 ee invariant mass distribution with fit . . . 107
10.3 eg invariant mass distribution with fit . . . 107
10.4 Data/MC comparison of $E_{\mathrm{T}}^{\mathrm{miss}}$ and $M_{b\bar{b}}$ in eCRL . . . 111
10.5 Data/MC comparison of $E_{\mathrm{T}}^{\mathrm{miss}}$ and H_{T} in eCRH . . . 111
10.6 $E_{\mathrm{T}}^{\mathrm{miss}}$ and $M_{b\bar{b}}$ MC shape comparison in SRL and eCRL . . . 112
10.7 $E_{\mathrm{T}}^{\mathrm{miss}}$ and H_{T} MC shape comparison in SRH and eCRH . . . 112
10.8 electron p_{T} comparison . . . 116
10.9 $E_{\mathrm{T}}^{\mathrm{miss}}$ distributions in LCR1L and eLCR1L . . . 123
10.10 $M_{b\bar{b}}$ distributions in LCR5L and eLCR5L . . . 123
10.11 $E_{\mathrm{T}}^{\mathrm{miss}}$ distributions in LCR2H and eLCR2H . . . 124
10.12 H_{T} distributions in LCR2H and eLCR2H . . . 124
10.13 $E_{\mathrm{T}}^{\mathrm{miss}}$ comparison in tagged and untagged regions . . . 129
10.14 VR1L result histograms . . . 134
10.15 VR2L result histograms . . . 135
10.16 VR3L result histograms . . . 136
10.17 VR4L result histograms . . . 137
10.18 VR1H result histograms . . . 139
10.19 VR2H result histograms . . . 140
10.20 VR3H result histograms . . . 141
10.21 VR4H result histograms . . . 142

11.1 Photon ID uncertainty in gluino grid . . . 146
11.2 JER uncertainty in gluino grid . . . 146
11.3 JES uncertainty in gluino grid . . . 147
11.4 $E_{\mathrm{T}}^{\mathrm{miss}}$ soft term uncertainty in gluino grid . . . 147
11.5 b-tagging uncertainty in gluino grid . . . 147

12.1 SRL result histograms . . . 153
12.2 SRH result histograms . . . 154
12.3 Efficiency of low mass cuts in gluino grid by production mechanism . . . 158
12.4 Total efficiency and yield of low mass cuts in gluino grid . . . 159
12.5 Efficiency of high mass cuts in gluino grid by production mechanism . . . 159
12.6 Total efficiency and yield of high mass cuts in gluino grid . . . 160
12.7 Expected $\mathrm{CL_s}$ contours for SRH by production mechanism . . . 161
12.8 Expected $\mathrm{CL_s}$ contours for SRL by production mechanism . . . 161
12.9 Expected combined $\mathrm{CL_s}$ contours for SRL and SRH . . . 162
12.10 Observed combined $\mathrm{CL_s}$ contours for SRL and SRH . . . 162
12.11 Expected and observed combined $\mathrm{CL_s}$ limits for SRL and SRH . . . 163
12.12 Selection of analysis for combined limit . . . 163

12.13Final gluino limit with merged SRL and SRH results 164

B.1 Signal contamination in LCR5L 184
B.2 Signal contamination in LCR2H 184
B.3 Signal contamination in QCR3L 185
B.4 Signal contamination in QCR3H 186

List of Tables

3.1 Standard Model particles and their superpartners 17

7.1 Luminosity by run period 58
7.2 $t\bar{t}$ MC samples 62
7.3 Single top MC samples 66
7.4 $W + \gamma$ MC samples 68
7.5 $Z + \gamma$ MC samples 68
7.6 Diboson MC samples 69
7.7 γ+jet MC samples 70
7.8 Multijet QCD MC samples 71
7.9 M_1 and μ for each neutralino mass 72
7.10 Gluino grid cross sections 76
7.11 Gaugino production cross sections 76

9.1 SRL cut flow 86
9.2 SRH cut flow 89
9.3 Signal region cuts 90

10.1 Z→ee MC samples 103
10.2 e→ γ fake rate in data and MC 108
10.3 e→ γ fake rate as function of p_{T} 108
10.4 e→ γ fake rate as function of fit width 108
10.5 e→ γ fake rate as function of fit shape 109
10.6 Low mass electron control regions 110
10.7 High mass electron control regions 110
10.8 eCRL cut flow 113
10.9 eCRH cut flow 113
10.10 Low mass electron control region predictions 113
10.11 High mass electron control region predictions 114
10.12 electron p_{T} dependent eCRL scale factors 116
10.13 electron p_{T} dependent eCRH scale factors 116
10.14 Low mass lepton control regions 118

10.15High mass lepton control regions . . . 118
10.16Low mass lepton control region yields . . . 119
10.17High mass lepton control region yields . . . 120
10.18Low mass lepton control region predictions . . . 122
10.19High mass lepton control region predictions . . . 125
10.20Low mass QCD control regions . . . 127
10.21High mass QCD control regions . . . 127
10.22Low mass QCD validation region . . . 127
10.23High mass QCD validation region . . . 127
10.24Low mass QCD correction factors . . . 129
10.25High mass QCD correction factors . . . 130
10.26QCD predictions . . . 130
10.27Background predictions . . . 132
10.28Low mass validation region cuts . . . 133
10.29Low mass signal and validation region background predictions . . . 133
10.30High mass validation region cuts . . . 138
10.31High mass signal and validation region background predictions . . . 138

11.1 Signal systematics . . . 148
11.2 Background systematics . . . 149

12.1 Signal region results . . . 152
12.2 Model-independent limits . . . 157

A.1 $W \to e\nu$ MC samples . . . 179
A.2 $W \to \mu\nu$ MC samples . . . 180
A.3 $W \to \tau\nu$ MC samples . . . 181
A.4 $Z \to \nu\nu$ MC samples . . . 182

C.1 $t\bar{t}$ +γ truth sample cut flows . . . 188
C.2 $t\bar{t}$ +γ truth sample relative uncertainties . . . 189
C.3 $t\bar{t}$ +γ PDF uncertainty . . . 189
C.4 W+γ truth sample cut flows . . . 190
C.5 W+γ truth sample relative uncertainties . . . 191
C.6 W+γ PDF uncertainty . . . 192

Abstract

Search for supersymmetry using a photon, b-jets, and $E_{\mathrm{T}}^{\mathrm{miss}}$ final state with the ATLAS detector in proton-proton collisions at 8 TeV center-of-mass energy

by

Andrew David Kuhl

A search for supersymmetric particle production in a photon, b-jet and $E_{\mathrm{T}}^{\mathrm{miss}}$ final state is conducted using 20.3 $\mathrm{fb}^{-1}$of proton-proton collision data collected by the ATLAS detector at a center-of-mass energy of $\sqrt{s} = 8$ TeV at the LHC in 2012. Two signal regions are defined, with one geared toward high-mass gluino production decaying to a moderate-to-high-mass neutralino and the other geared toward direct gaugino production. Several variables are optimized for sensitivity to the targeted scenario, including photon p_{T}, $E_{\mathrm{T}}^{\mathrm{miss}}$, N_{jets}, and $N_{b-\mathrm{jets}}$, among others. The Standard Model contribution is estimated using data-driven methods, and no significant excess above Standard Model expectations is observed in either of the signal regions. In one signal region, a total of 12 candidate events are observed while 18.8 $\pm$ 5.3 events are expected from Standard Model backgrounds. In the other signal region, a total of 2 candidate events are observed while 3.63 $\pm$ 1.25 events are expected from Standard Model backgrounds.

The result of this analysis is interpreted in a general gauge mediation framework with a lightest neutralino that is a mixture of bino and higgsino. Limits are set in a 2D plane of gluino mass vs neutralino mass. Neutralino masses between 150 GeV and 450 GeV are excluded at 95% CL for all gluino masses, and gluino masses up to at least

1200 GeV (and up to 1350 GeV in some cases) are excluded at 95% CL for neutralino masses between 450 GeV and 50 GeV less than the gluino mass.

To Danielle, Connor, and baby number 2,

for the love and support and motivation you provide.

Acknowledgments

Thank you to Jason Nielsen for teaching me everything I know about particle physics, as well as the many contributions he made to the work in this dissertation. In addition to Jason, I would like to thank everyone in the ATLAS groups at SCIPP and ANL for the opportunity to work at these excellent institutions while researching for this dissertation. I would also like to thank ATLAS colleagues Ehud Duchovni, Ofir Gabizon, and Dmitry Milstein for their contributions to the 7 TeV version of this analysis. Without these contributions, the work in this dissertation would not have been possible. I am also grateful for Jovan Mitrevski's guidance in using the ATLAS software and his assistance in pushing the analysis through the ATLAS SUSY group. Lastly, thank you to my beautiful wife Danielle, for always being by my side.

Part I

Theoretical Motivation

Chapter 1

Introduction

The Standard Model (SM) of particle physics was developed in the latter half of the twentieth century using the results of many particle colliders. It is the culmination of the work of thousands of experimental and theoretical physicists. The Standard Model has predicted several new particles prior to their discoveries, including the W and Z bosons and the top quark. Most recently, in 2012, the Higgs boson was discovered at the Large Hadron Collider (LHC) by the ATLAS and CMS experiments [1, 2]. The Higgs boson was the final particle predicted by the Standard Model, and with it found, the focus of the LHC experiments shifts to whether there is new physics beyond the Standard Model at the energy levels probed by the LHC.

One potential source of new physics that the LHC may have access to is called supersymmetry (SUSY). Supersymmetry is a proposed extension of the Standard Model that relates bosons, which have integer spin, to fermions, which have half-integer spin [3]. For each particle in the Standard Model, a superpartner is proposed with identical quantum numbers except for spin, which differs by a half-integer. This means that for each fermion in the Standard Model, a new boson would be predicted and vice versa.

Supersymmetry can potentially provide solutions to several of the lingering questions that are not addressed in the Standard Model, such as the source of dark matter and the hierarchy problem, which makes it especially attractive [4].

However, if the supersymmetric particles had identical mass to their SM partners, they would have been observed experimentally. Therefore, SUSY must be a broken symmetry, and the superpartners must acquire a large mass as a result of the symmetry breaking. One of several potential supersymmetry breaking models is referred to as gauge mediated supersymmetry breaking (GMSB) [4]. In GMSB the superpotential is broken in a hidden sector at very high scale that does not couple to the Standard Model fields. GMSB does, however, possess a set of massive messenger fields that are charged under Standard Model gauge interactions and also couple to the hidden sector. Thus, the breaking of SUSY in the hidden sector is transmitted to the superpartners through the Standard Model gauge interactions.

Supersymmetric models have many free parameters, leading to a wide array of mass spectra and phenomenologies. The experimental signature is highly dependent on how these parameters are defined. One feature that many SUSY models have in common is the conservation of R-parity. R-parity is introduced in order to prevent the proton from being destabilized by the addition of SUSY to the Standard Model. Due to R-parity conservation, SUSY particles must be pair produced, and each SUSY particle's decay must include other SUSY particles. Eventually, the cascade must end at the lightest supersymmetric particle (LSP), which is stable. If the LSP only interacts weakly with Standard Model particles, it could potentially be a dark matter candidate.

In this scenario, the LSP's lack of interaction would allow it to pass through the detector undetected. There are several supersymmetric particles that meet these qualifications; GMSB predicts a gravitino LSP, typically with mass much less than 1 GeV, while many other models predict a neutralino LSP. Due to conservation of momentum and the cylindrical geometry of the ATLAS detector, events containing the LSP would be seen to have an imbalance in the vector sum of momentum in the transverse plane. This is referred to as missing transverse energy, or $E_{\mathrm{T}}^{\mathrm{miss}}$, and is a key signature in R-parity conserving SUSY models.

GMSB models have other key features in addition to missing energy from gravitino LSPs. The signature is typically determined by the properties of the next-to-lightest supersymmetric particle (NLSP), which is produced as part of the cascade of SUSY particles and decays to the LSP and a Standard Model particle. In a large subset of GMSB models, the Standard Model particle emitted by the NLSP is a gauge or Higgs boson (γ,Z,W$^{\pm}$, h). Depending on a few specific parameters, the branching ratio of the NLSP to several of the gauge bosons can be significant, resulting in a multitude of potential final states.

This dissertation focuses on a search for events in which the NLSP produces a photon on one side of the event and a Higgs boson on the other, with the Higgs boson decaying to a $b\bar{b}$ pair. The search is done using 20.3 fb^{-1} of $\sqrt{s} = 8$ TeV collision data collected by the ATLAS detector at the LHC in 2012. Chapter 2 discusses the Standard Model in more detail, while Chapter 3 details SUSY, GMSB in particular, and why it is an attractive extension to the Standard Model. Chapter 4 discusses

previous experimental searches for GMSB with photons. Chapters 5 and 6 detail the Large Hadron Collider and the ATLAS detector. Lastly, Chapters 8-12 contain the details of the analysis performed and the results with a GMSB interpretation.

Chapter 2

The Standard Model

The Standard Model of particle physics is a theory regarding fundamental subatomic particles and their interactions. It describes the electromagnetic, weak, and strong nuclear interactions and can be essentially be defined as a $SU(3)_C \times SU(2)_L \times SU(1)_\gamma$ gauge theory [5]. The fourth fundamental force, gravity, is not incorporated into the Standard Model. There is currently no direct experimental evidence that any physics beyond the Standard Model exists, but there are several interesting phenomena which the Standard Model is unable to explain. This chapter will briefly discuss the interactions and particles that make up the Standard Model, as well as the issues that hint that the Standard Model is an incomplete theory and that new physics is required.

2.1 Fermions

The Standard Model includes 12 spin-$\frac{1}{2}$ elementary particles that are known as fermions. Half of the fermions are quarks and half are leptons, and each fermion has a corresponding antiparticle that has opposite charge. The 12 fermions can be grouped into 3 generations of 4 particles each. Each generation contains two quarks and two

leptons and are grouped according to their masses. The first generation contains the up (u) and down (d) quarks and the electron (e) and electron neutrino (ν_e). The second generation contains the charm (c) and strange (s) quarks and the muon (μ) and muon neutrino (ν_μ). The third generation contatins the top (t) and bottom (b) quarks and the tau (τ) and tau neutrino (ν_τ). In addition to grouping the particles by mass, the left-handed particles (and right-handed anti-particles) of each generation also consist of two weak isospin doublets (one quarks and one leptons) which roughly correspond to the mass eigenstates. However, there is a small amount of mixing between the flavor eigenstates under charged weak currents, which leads to CP violation. The mixing of the quarks is described by the Cabibbo-Kobayashi-Maskawa (CKM) matrix, while mixing in the neutralino sector is described by the Pontecorvo-Maki-Nakagawa-Sakata (PMNS) matrix.

The defining characteristic of quarks is that they have color charge, and thus interact via the strong nuclear force. Due to color confinement, quarks are not observed outside of bound states called hadrons. Hadrons can be made up of either a quark and an antiquark (meson) or three quarks/anti-quarks (baryon). In each case, the hadron is "neutral" in color charge, either by containing opposing color charges in the case of mesons, or containing one of each color/anti-color in the case of baryons. The most common mesons are the pions ($\pi^\pm$, π^0), which are bound states of up and down quarks and anti-quarks. The most common baryons are the proton and the neutron, which consist of up and down quarks. Quarks also carry electric charge and weak isospin, so they interact via the electromagnetic and weak forces as well.

Leptons do not carry color charge, and only half of them carry electric charge. The electron, muon, and tau carry both electric charge and weak isospin and interact through both the electromagnetic and weak interactions. The three neutrinos, however, are influenced only by the weak force, and are notoriously difficult to detect due to this property.

The first generation of fermions are stable and do not decay, so they are the constituents of all ordinary matter in the universe. Specifically, atoms consist of electrons orbiting atomic nuclei that are composed of protons and neutrons, which consist of up and down quarks. The charged particles of the second and third generation, however, decay quickly. Most cannot be observed directly, and must be observed indirectly by looking at the decay products using a particle detector. One major exception is the muon, and hadrons containing strange quarks can also be observed directly. Neutrinos do not decay, but interact very weakly with baryonic matter, so they are very rarely observed as well.

2.2 Gauge Bosons

The interactions described by the Standard Model are mediated by a set of spin-1 force carriers called the gauge bosons. These are the photon, $W^{\pm}$ and Z bosons, and gluon which mediate the electromagnetic, weak, and strong forces, respectively. The photon and gluon are massless; however, the weak force bosons have a large mass due to the spontaneous breaking of the electroweak symmetry via the Higgs mechanism [6, 7, 8].

At high energies, the electromagnetic and weak interactions are unified into a single interaction called the electroweak interaction. It is represented mathematically by SU(2) x U(1). There are 3 bosons of weak isospin (W^+, W^-, and W^0) associated with the SU(2) group, and a single boson of weak hypercharge (B^0) associated with the U(1) group. Due to the spontaneous symmetry breaking, the neutral W^0 and B^0 eigenstates mix to form the γ and Z^0 mass eigenstates as shown in Equation 2.1, where θ_W is the weak mixing angle [9, 10].

$$\begin{pmatrix} \gamma \\ Z^0 \end{pmatrix} = \begin{pmatrix} \cos\theta_W & \sin\theta_W \\ -\sin\theta_W & \cos\theta_W \end{pmatrix} \begin{pmatrix} B^0 \\ W^0 \end{pmatrix} \tag{2.1}$$

As a result of the electroweak symmetry breaking, the $W^\pm$ and Z^0 acquire masses related by Eq. 2.2 [11].

$$m_Z = \frac{m_W}{cos\theta_W} \tag{2.2}$$

The gluons are the representation of the SU(3) color gauge group, so there are an octet of gluon fields. Each gluon has a combination of two colors (one color and one anti-color), in a superposition of states given by the Gell-Mann matrices. Because gluons themselves carry color charge, they interact with each other. There is both a three-gluon vertex and a four-gluon vertex.

2.3 Higgs Boson

The Standard Model has one fundamental scalar (spin-0) particle, referred to as the Higgs boson. The Higgs boson (or at least a particle with properties very much

like the Higgs boson) was discovered in 2012 by the ATLAS and CMS collaborations, approximately 50 years after it was first proposed as the mechanism for electroweak symmetry breaking [6, 7, 8]. It is a quantum excitation of one of the four components of the Higgs field, which is described by a complex scalar doublet with a non-zero vacuum expectation value (vev). When the electroweak symmetry is broken, three of the four degrees of freedom of the Higgs field are "absorbed" by the $W^{\pm}$ and Z^0 bosons, giving them large masses and making the weak interaction extremely short range. The remaining unabsorbed component of the Higgs field manifests itself as the Higgs boson, and is also responsible for the masses of the fermions through Yukawa couplings [12].

Prior to its discovery in 2013, the Higgs boson was the lone unobserved particle predicted by the Standard Model. After many analyses studying the spin, parity, and couplings of the newly discovered particle, the results are consistent with the Standard Model predictions for the Higgs boson [13, 14, 15, 16]. However, there are many Beyond the Standard Model (BSM) theories that can accomodate a particle very much like the Standard Model Higgs while addressing some of the limitations of the Standard Model.

2.4 Standard Model Limitations

Although the Standard Model agrees extremely well with experimental results, there are certain issues that it either fails to address or addresses somewhat inadequately. There are 19 arbitrary parameters in the Standard Model that are defined by experimental results, including gauge couplings, fermion masses, and angles in the CKM matrix [17]. Two other issues that are not addressed in the Standard Model are dark matter

and the hierarchy problem, which are discussed in Sections 2.4.1 and 2.4.2. These issues are especially interesting for the analysis discussed in this paper, as both can be solved by the addition of supersymmetry to the Standard Model.

2.4.1 Dark Matter

Dark matter was first proposed as a solution to discrepancies between galaxies' observed rotational velocity and the expected rotational velocity based on the visible mass of the galaxies [18]. Subsequently, results based on gravitational lensing [19] and the cosmic microwave background [20] also support the hypothesis of dark matter. Currently, there is estimated to be dark matter in the universe equal to five times the mass of normal baryonic matter. The scientific consensus is that this dark matter is due to additional massive particles that interact only weakly with Standard Model particles. In supersymmetric models there is nearly always a particle that fits this description [21].

2.4.2 Hierarchy Problem

The hierarchy problem questions how the mass of the Higgs boson is so small relative to the Planck scale when the Higgs sector is extremely sensitive to quantum corrections. The electrically neutral part of the Standard Model Higgs boson is a complex scalar H and has a classical potential shown in Eq. 2.3.

$$V = m_H^2|H|^2 + \lambda|H|^4 \tag{2.3}$$

When $m_H^2 < 0$ and $\lambda > 0$, the vacuum expectation value is non-zero at the minimum of the potential, which is required by the Standard Model. This results in the relation shown in Eq. 2.4.

$$\langle H \rangle = \sqrt{-m_H^2/\lambda} \tag{2.4}$$

The value of the Higgs vev is known to be approximately 246 GeV from precision electroweak measurements. If λ is of order 1, this suggests that m_H^2 is on the order of -(100 GeV)^2 [4]. This agrees well with the observed Higgs mass of approximately 125 GeV, but this value should have corrections due to the coupling of massive fermions to the Higgs. A massive fermion, f, couples to the Higgs by a term in the Lagrangian of $-\lambda_f H \bar{f} f$. This results in a correction to m_H^2 as shown in Eq. 2.5.

$$\Delta m_H^2 = -\frac{|\lambda_f|^2}{8\pi^2}[\Lambda_{UV}^2 + \mathcal{O}(\ln(\Lambda_{UV})) + ...] \tag{2.5}$$

Λ_{UV} is the ultraviolet cutoff and can be interpreted as the scale to which the Standard Model is valid. If this is taken to be the Planck scale $M_P = (8\pi G_{Newton})^{-1/2} = 2.4 \times 10^{18}$, and $\lambda_f \approx 1$, then this correction due to the top quark is around 30 orders of magnitude greater than the predicted value of $m_H^2 \approx -(100GeV)^2$. Thus, the hierarchy problem is due to the difference between the electroweak scale and the Planck scale, or in other terms, the fact that gravity is so much weaker than the other forces. Solving this problem requires either an incredibly high amount of fine tuning (for example, by making λ_f incredibly small), which is an unattractive option, or some sort of cancellation of these diverging terms. How supersymmetry cancels these terms will be discussed in Section 3.1.

Chapter 3

Supersymmetry

Supersymmetry is a class of theories that propose an additional symmetry relating fields of different spins, namely fermions and bosons. It arises from extending the normal Poincaré group algebra of the Standard Model with a set of generators that obey the anti-commutation relation

$$\left\{Q_\alpha, Q^\dagger_{\dot{\alpha}}\right\} = -2\sigma^\mu_{\alpha\dot{\alpha}} \cdot P_\mu \tag{3.1}$$

where σ^μ are the Pauli spin matrices and P_μ are the space-time translation generators [4]. When these generators act on an helicity state, they have the effect of raising or lowering the spin by 1/2, thus turning a boson into a fermion and vice versa. Only the $N = 1$ minimal supersymmetric extension to the Standard Model (MSSM) will be considered here, where N refers to the number of distinct copies of $Q, Q^\dagger$ generators in the model.

3.1 The Minimal Supersymmetric Model

Supersymmetry postulates that particles are members of supermultiplets that contain equal numbers of fermionic and bosonic degrees of freedom. This means that

each SM fermion has a boson superpartner, and each SM boson has a fermion superpartner. The mass-squared and gauge operators commute with the supersymmetry operators, which implies that the mass and gauge quantum numbers are the same for all members of a supermultiplet. However, since no superpartners have been observed, supersymmetry must be spontaneously broken at some higher energy scale. This breaking is responsible for giving the superpartners higher mass, similar to how the $W^{\pm}$ and Z bosons get their mass from electroweak symmetry breaking.

In order to avoid gauge anomalies, the Higgs sector in a supersymmetric theory must be expanded to a two Higgs doublet model. One doublet couples to up-type quarks, and the other couples to down-type quarks and charged leptons. Of the eight degrees of freedom, three are still responsible for the $W^{\pm}$ and Z masses. The five remaining degrees of freedom are physical Higgs states that include two CP-even Higgs bosons (h, H), one CP-odd Higgs bosons (A), and a pair of charged Higgs bosons ($H^{\pm}$). In many supersymmetric models, the lighter CP-even Higgs (h) has mass and decay branching ratios similar to a SM Higgs. The ratio of the vacuum expectation values of the two Higgs doublets ($\tan\beta = \langle H_u \rangle / \langle H_d \rangle$) is an important parameter for the phenomenology of supersymmetry.

Supersymmetry is an attractive theory for several reasons. It provides elegant solutions to the issues discussed in Section 2.4. R-parity conserving supersymmetry models provide dark matter candidates. This is discussed further in Section 3.4. Supersymmetry also provides a solution to the hierarchy problem. Just as Standard Model fermions provide a correction to the Higgs mass as in Eq. 2.5, scalar superpartners also

provide a correction due to their coupling to the Higgs in the Lagrangian of -$\lambda_S|H^2||S^2|$. This results in corrections to m_H^2 as shown in Eq. 3.2.

$$\Delta m_H^2 = \frac{\lambda_S}{16\pi^2}[\Lambda_{UV}^2 + \mathcal{O}(\ln(\Lambda_{UV})) + ...] \tag{3.2}$$

It is important to note that Eq. 3.2 has the opposite sign of Eq. 2.5. This is due to the differing spin statistics between bosons and fermions. The coefficient of the correction due to the scalars is also one half as large as the correction due to fermions, but since there is a scalar partner of both the left- and right-handed fermions, the coefficients are the same magnitude if $\lambda_S = |\lambda_f|^2$. This is always the case for an unbroken symmetry [4]. In order for this cancellation to work as a solution for the hierarchy problem, this relationship must be preserved after SUSY is broken. This can be achieved by "soft" supersymmetry breaking, where the effective Lagrangian of the MSSM can be written as

$$\mathscr{L} = \mathscr{L}_{\text{SUSY}} + \mathscr{L}_{\text{soft}} \tag{3.3}$$

where $\mathscr{L}_{SUSY}$ contains all of the gauge and Yukawa interactions and preserves supersymmetry invariance, and $\mathscr{L}_{soft}$ contains only mass terms and violates supersymmetry. These mass terms have the form $m_{soft}^2|S|^2$ for the scalar superpartners, which results in corrections to the Higgs mass of:

$$\Delta m_H^2 = m_{soft}^2\Big[\frac{\lambda_S}{16\pi^2}\ln(\Lambda_{UV}/m_{soft}) + ...\Big] \tag{3.4}$$

In order for the corrections to remain small relative to the Higgs mass itself, the soft masses must not be much larger than the electroweak symmetry breaking

scale. Depending on the model used, these soft masses can be either free parameters or related to each other by some theoretically motivated mechanism of how SUSY is broken. Gauge-Mediated Supersymmetry Breaking (GMSB) is the mechanism used for the analysis discussed in this dissertation, and will be described in more detail in Section 3.5.

3.2 Superpartner Naming Conventions

The list of all supersymmetric particles, nicknamed sparticles, and their Standard Model partners is shown in Table 3.1.

The partners of quarks and leptons are named by prepending an "s", standing for "scalar", to the name of the Standard Model particle. Collectively, they are called sfermions, quark superpartners are called squarks, and lepton superpartners are called sleptons. This convention is also used for the individual particle names; for example, stop is the superpartner of top and selectron the superpartner of electron. The left and right-handed fermions have their own superpartners so that they have the same SU(2) doublets or singlets, though the sfermions themselves do not have any handedness since they are scalar. The third generation of sfermions can have significant mass difference between the partners of the left- and right-handed particles due to large Yukawa couplings, but for the other generations the masses are degenerate [4].

The partners of Standard Model bosons are named by appending "ino" to the Standard Model name. Collectively, the partners of the gauge bosons are called gauginos. This includes the partners of the gluon, W, and B, called gluinos, winos,

and binos. The supersymmetric partners of the Higgs bosons are called higgsinos. The bino, neutral wino, and neutral higgsino eigenstates mix to form mass eigenstates called neutralinos, which are represented by the symbols χ_1^0, χ_2^0, χ_3^0, and χ_4^0, from low mass to high mass. The mixing is discussed further in Section 3.3. The charged winos and higgsinos also mix to form mass eigenstates called charginos. They are represented by the symbols $\chi_1^\pm$ and $\chi_2^\pm$. Lastly, the superpartner of the graviton (spin 2) is the gravitino (spin 3/2). They are represented by G and $\tilde{G}$, respectively. The gravitino plays an important role in Gauge-Mediated Supersymmetry Breaking phenomenology, discussed in Section 3.5.

Table 3.1: The Standard Model particles and their corresponding superpartners [4]. The names, spins, and symbols used for each are shown. SU(2) doublets are shown in parantheses.

Particle Names	Spin-1/2	Spin-0
quarks/squarks	$(u_L\ d_L), (c_L\ s_L), (t_L\ b_L)$ u_R, c_R, t_R d_R, s_R, b_R	$(\tilde{u}_L\ \tilde{d}_L), (\tilde{c}_L\ \tilde{s}_L), (\tilde{t}_L\ \tilde{b}_L)$ $\tilde{u}_R, \tilde{c}_R, \tilde{t}_R$ $\tilde{d}_R, \tilde{s}_R, \tilde{b}_R$
leptons/sleptons	$(e_L\ \nu_e), (\mu_L\ \nu_\mu), (\tau_L\ \nu_\tau)$ e_R, μ_R, τ_R	$(\tilde{e}_L\ \tilde{\nu}_e), (\tilde{\mu}_L\ \tilde{\nu}_\mu), (\tilde{\tau}_L\ \tilde{\nu}_\tau)$ $\tilde{e}_R, \tilde{\mu}_R, \tilde{\tau}_R$
	Spin-0	Spin-1/2
Higgs/higgsinos	$(H_u^+\ H_u^0)$ $(H_d^0\ H_d^-)$	$(\tilde{H}_u^+\ \tilde{H}_u^0)$ $(\tilde{H}_d^0\ \tilde{H}_d^-)$
	Spin-1	Spin-1/2
gluon/gluino	g	$\tilde{g}$
W boson/wino	$W^\pm\ W^0$	$\tilde{W}^\pm\ \tilde{W}^0$
B boson/bino	B^0	$\tilde{B}^0$
	Spin-2	Spin-3/2
graviton/gravitino	G	$\tilde{G}$

3.3 Neutralino Mixing

The neutralino mass eigenstates are determined by finding the eigenvalues of the neutralino mass matrix for a given set of parameters. The neutralino mixing matrix is shown in Equation 3.5. The masses of the bino, neutral wino, and neutral higgsinos are represented by M_1, M_2, and μ, respectively. s_β and c_β represent sinβ and cosβ, while s_W and c_W represent the sine and cosine of the electroweak mixing angle.

$$N = \begin{pmatrix} M_1 & 0 & -m_Z c_\beta s_W & m_Z s_\beta s_W \\ 0 & M_2 & m_Z c_\beta c_W & -m_Z s_\beta c_W \\ -m_Z c_\beta s_W & m_Z c_\beta c_W & 0 & -\mu \\ m_Z s_\beta s_W & -m_Z s_\beta c_W & -\mu & 0 \end{pmatrix} \begin{pmatrix} \tilde{B} \\ \tilde{W}^0 \\ \tilde{H}_d \\ \tilde{H}_u \end{pmatrix} \tag{3.5}$$

A general neutralino NLSP can be any linear combination of bino, wino, and higgsino gauge eigenstates:

$$\tilde{\chi}_1^0 = \sum_{i=1}^{4} N_{1i} \tilde{\psi}_1^0 \tag{3.6}$$

where $\tilde{\psi}_1^0 = (\tilde{B},\, \tilde{W}^0,\, \tilde{H}_d^0,\, \tilde{H}_u^0)$. The mass eigenvectors will vary based on M_1, M_2, μ and $\tan\beta$. With this notation, the general formulas for the NLSP decay widths (when the Z and Higgs decays are on-shell) are [22]:

$$\begin{aligned} \Gamma(\tilde{\chi}_1^0 \to \tilde{G} + \gamma) &= |N_{11} c_W + N_{12} s_W|^2 \mathcal{A} \\ \Gamma(\tilde{\chi}_1^0 \to \tilde{G} + Z) &= \left(|N_{12} c_W - N_{11} s_W|^2 + \frac{1}{2} |N_{13} c_\beta - N_{14} s_\beta|^2 \right) \left(1 - \frac{m_Z^2}{m_{\tilde{\chi}_1^0}} \right)^4 \mathcal{A} \\ \Gamma(\tilde{\chi}_1^0 \to \tilde{G} + h) &= \frac{1}{2} |N_{13} c_\beta + N_{14} s_\beta|^2 \left(1 - \frac{m_h^2}{m_{\tilde{\chi}_1^0}} \right)^4 \mathcal{A} \end{aligned} \tag{3.7}$$

where $\mathcal{A}$ is a dimensionful parameter that sets the scale of the NLSP lifetime:

$$\mathcal{A} = \frac{m_{\tilde{\chi}_1^0}^5}{16\pi F_0^2} \approx \left(\frac{m_{\tilde{\chi}_1^0}}{100\ \text{GeV}}\right)^5 \left(\frac{100\ \text{TeV}}{\sqrt{F_0}}\right)^4 \frac{1}{0.1\ \text{mm}} \tag{3.8}$$

where $\sqrt{F_0}$ is the scale of SUSY breaking, which is bounded to be between approximately 10 TeV and 10^6 TeV. The lower boundary is necessary to provide a viable superpartner spectrum, while the upper boundary is necessary for gauge mediation to dominate over gravity mediation. F_0 also determines the gravitino mass through the relation $m_{\tilde{G}} = F_0/(\sqrt{3}M_{\text{P}})$ [22].

3.4 R-Parity

If all renormalizable couplings possible were included in the MSSM, there would be interactions that violate baryon-number (B) and lepton-number (L). With reasonable assumptions for parameters affecting the coupling strength, these couplings would cause proton decay in fractions of a second. This is a huge problem due to the observation of proton lifetime longer than 10^{33} years [23]. This problem can be mitigated by introducing a new concept called R-parity [4], defined in Equation 3.9, where s is the spin of a particle.

$$P_R = (-1)^{3(B-L)+2s} \tag{3.9}$$

If R-parity is conserved, then the renormalizable baryon-number and lepton-number violating terms in the MSSM are disallowed. It works out that all SM particles have R-parity = +1, while all sparticles have R-parity = -1. This has several interesting consequences. In order to conserve R-parity, any interaction must include an even

number of sparticles. This means that supersymmetric particles can only be produced in even numbers (usually two). It also means that the lightest supersymmetric particle (LSP) must be stable. A charged LSP would likely be discovered very quickly by both astronomical observations and collider experiments, so the LSP is assumed to be electrically neutral. In this case, it will interact only weakly with ordinary matter, and is a good candidate for the dark matter discussed in Section 2.4.1. Any supersymmetric particles produced in a collider will decay to lighter and lighter sparticles until the LSP is produced. The LSP, if electrically neutral, will escape undetected, resulting in missing transverse energy. There are SUSY models that do not conserve R-parity, but those will not be considered for this analysis.

3.5 Gauge-Mediated Supersymmetry Breaking

If supersymmetry actually describes nature, it must be a broken symmetry since no supersymmetric partners have been observed with masses of Standard Model particles. There are several proposed mechanisms for this breaking, but this dissertation will focus on gauge-mediated supersymmetry breaking (GMSB) models. In GMSB models, supersymmetry is spontaneously broken in a hidden sector by a field that does not couple to the MSSM, with non-zero vacuum expectation value of $\langle F \rangle$. The breaking is communicated to the MSSM through massive messenger fields that are charged under the SM $SU(3)_C \times SU(2)_L \times SU(1)_\gamma$ gauge interactions [4]. Due to the breaking being communicated through the gauge interactions themselves, the SM flavor symmetries are naturally protected, so there are no flavor changing neutral currents (FCNCs) or

additional CP violations expected.

In GMSB models, the gravitino is always the LSP. It couples to each particle and its superpartner with strength inversely proportional to $\sqrt{F}$. This means the NLSP is unstable and will decay to its SM partner and a gravitino, though its decay length depends on $\sqrt{F}$. This paper will consider only the case where the NLSP decays promptly with $c\tau < 0.25$ mm.

Two classes of GMSB models have been used by ATLAS to motivate searches for neutralino decays. The first is minimal GMSB, which defines the SUSY mass spectrum using a limited number of parameters. This model can produce neutralino NLSPs, but these neutralinos are always bino-like. Bino-like NLSPs decay only to photons or Z bosons, so do not frequently give rise to a photon + b final state. The second model is called General Gauge Mediation (GGM), and it has more parameters that allow more freedom in the SUSY mass spectrum [24]. These parameters can be tuned to adjust the neutralino decays and the production mechanism and cross section, as discussed in Section 3.6.

3.6 Photon + b + $E_{\mathrm{T}}^{\mathrm{miss}}$ Phenomenology in GGM

Because the SUSY parameters are unknown, ATLAS performs SUSY searches driven by final state phenomonology. This analysis is one of four analyses focused on high p_{T} photons from NLSP neutralino decays. An NLSP neutralino can decay to $Z/\gamma/h + \tilde{G}$. The branching ratio to each of the three bosons is determined by the mass parameters of the bino (M_1), wino (M_2), and higgsino (μ), along with the ratio

of the up-type to down-type Higgs VEVs ($\tan\beta$). For $m_{\tilde{\chi}_1^0} \gg m_h$, a purely bino NLSP ($M_1 \ll M_2$, $|\mu|$) or purely wino NLSP ($M_2 \ll M_1$, $|\mu|$) will decay to Z or γ, with the branching ratios based on the electroweak mixing angle, while purely higgsino NLSPs ($|\mu| \ll M_1$, M_2) couple to Z and h, with the branching ratios depending on $\tan\beta$ and the sign of μ. In order to achieve the desired branching ratios, the neutralino mass parameters are chosen in such a way to minimize the Z decay and balance the decays to γ and h in a consistent and optimal way.

Since winos decay predominantly to Z bosons, the wino mass is chosen to be decoupled from the bino and higgsino masses. This results in the coefficient $N_{12} = 0$ in Equation 3.7 in Section 3.3, thus reducing the NLSP branching ratios to Z bosons. In order to maximize the NLSP decay to Higgs bosons relative to Z bosons, μ is chosen to be negative and $\tan\beta$ small. For $\mu > 0$ or $\tan\beta$ large, the Z decay of the higgsino is much more prominent, which can be derived from Equation 3.7. Branching ratios of a 160 GeV neutralino NLSP to γ, Z, or 105 GeV Higgs boson ($+ \tilde{G}$) as a function of $\tan^{-1}(\mu/M_1)$ are shown in Figure 3.1. The four quadrants of the figure show the result for different selections of the sign of $|\mu|$ and $\tan\beta$. This figure is outdated because the Higgs boson is measured to be 125 GeV, but it illustrates the point that in order to minimize the Z decay, μ should be negative with $\tan\beta$ small. The upper left quadrant, with negative μ and small $\tan\beta$, is the only one with a Higgs decay more prominent than the Z decay. In addition, this figure shows that M_1 and $|\mu|$ must be balanced in order to achieve the desired NLSP branching ratios, with a fairly narrow range where decays to γ and Higgs are both prominent.

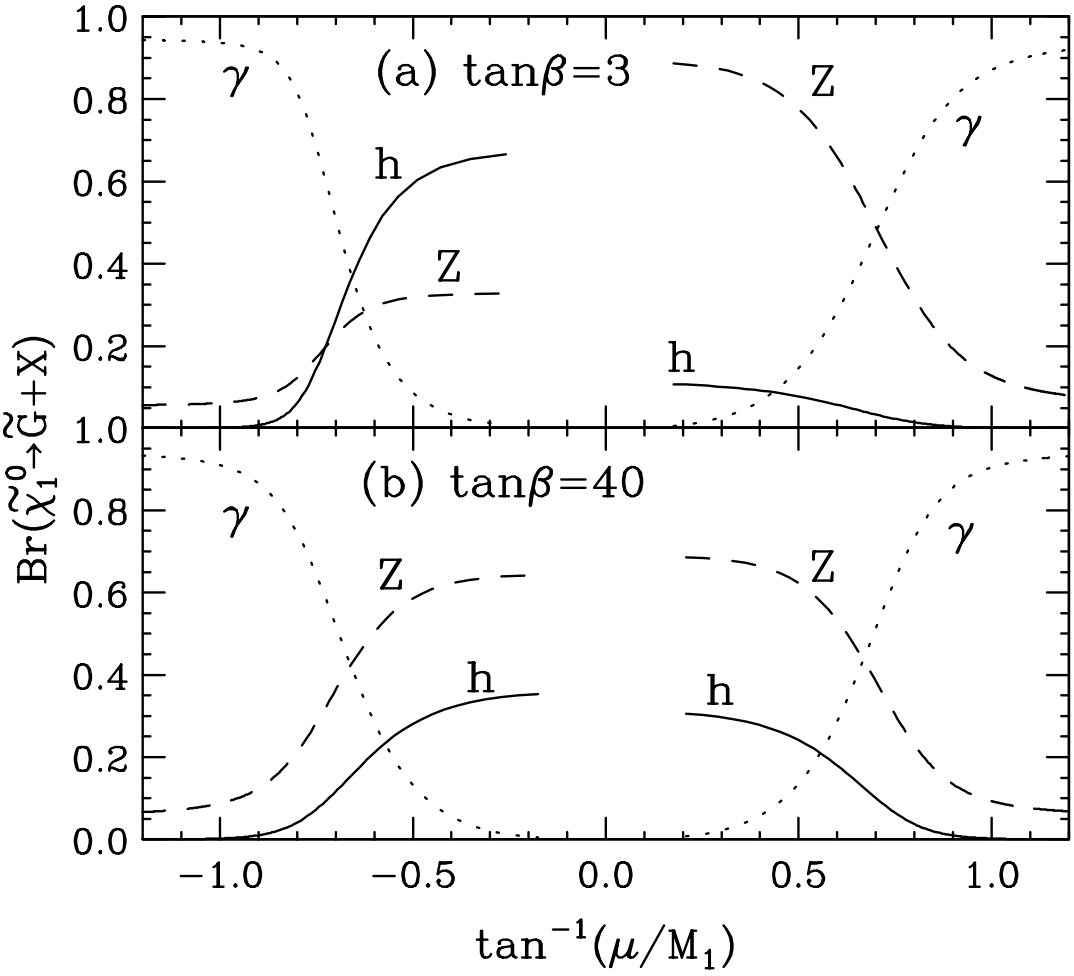

Figure 3.1: Branching ratios of a 160 GeV NLSP neutralino to γ, Z, or 105 GeV Higgs boson (+ $\tilde{G}$) for varying values of $\tan\beta$ and $\tan^{-1}(\mu/M_1)$ [25].

The signature also depends on how the event is produced. Events can be produced either through "strong" production, in which the hard scatter contains particles with color charge, or through "weak" production, in which the hard scatter does not contain particles with color charge. In either case, the event proceeds through a cascade of SUSY particles until eventually the NLSP neutralino is produced and decays to the LSP gravitino and a SM boson. In the case of weak production, the cross section is dominated by neutralinos and charginos with mass very near the NLSP mass, so there are very few additional objects produced in the event. On the other hand, for strongly produced events, there can be a large mass difference between the SUSY particles from the hard scatter and the NLSP, which can produce additional jets or other objects. For the purposes of this dissertation, interpretation for strongly produced events will only be done with colored gluino production, but a squark interpretation could be used as well. Feynman diagrams illustrating these mechanisms and potential decays are shown in Figure 3.2.

The result is interpreted in a 2D grid of gluino masses and NLSP neutralino masses. For each point, the NLSP neutralino is a combination of the bino and higgsino eigenstates, with the wino decoupled, as mentioned previously. As a result, three of the four neutralino mass eigenstates are near the same mass, and can contribute to gaugino production. In addition, one of the two chargino mass eigenstates are also near the NLSP mass. This results in several production modes involving gauginos.

Due to the sparticle couplings and parton distribution functions for the LHC beams, gluino production dominates gaugino production when they have similar masses.

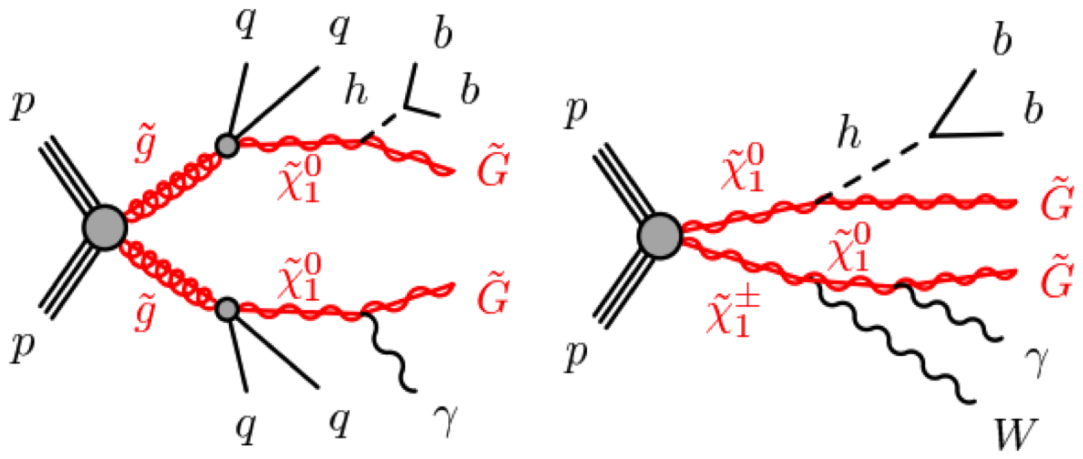

Figure 3.2: Feynman diagrams of the signal process yielding the $\gamma + b\bar{b} + E_{\mathrm{T}}^{\mathrm{miss}}$ final state for gluino (left) and gaugino production. For gaugino production, there are several other production modes from other combinations of neutralinos and charginos.

However, when the gauginos have significantly lower masses, gaugino production dominates. This results in two distinct regions in the 2D grid, with a narrow overlap region where the production modes are comparable in cross section.

Regardless of the production mode, the NLSP decays are always present in the events. However, when the decay chain starts with gluinos, there are more steps to the decay that can produce additional jets or leptons in the event. In addition, the initial objects in gluino events typically have higher energy. This results in a stark difference between the events of the two production modes.

Chapter 4

Previous Results

The final state discussed in this dissertation has not been thoroughly examined by experiments prior to the LHC. The only previous result is a GGM paper published using 4.7 fb^{-1}of $\sqrt{s} = 7$ TeV data collected by ATLAS in 2011 [26].

4.1 ATLAS 7 TeV Result

The most recent and only public result with this final state was published by the ATLAS collaboration and based on 4.7 fb^{-1}of $\sqrt{s} = 7$ TeV proton-proton collision data collected in 2011. The result discussed in this dissertation is an improvement on this result, utilizing multiple signal regions and 20.3 fb^{-1}of $\sqrt{s} = 8$ TeV proton-proton collision data collected in 2012.

A single photon trigger with a cutoff of 80 GeV was used to collect the data for the 7 TeV analysis. The analysis required that each event have a reconstructed photon with $p_{\mathrm{T}} > 125$ GeV, at least two jets, at least one b-tagged jet, and $E_{\mathrm{T}}^{\mathrm{miss}} > 150$ GeV. In addition, to reduce backgrounds, leptons were vetoed, the transverse mass of the photon and $E_{\mathrm{T}}^{\mathrm{miss}}$ needed to be greater than 100 GeV, and the $E_{\mathrm{T}}^{\mathrm{miss}}$ had to be isolated

from the leading two jets with $\Delta\phi > 0.4$.

The background for the 7 TeV analysis was modeled in four different components: one that estimated the portion due to electrons faking photons in $t\bar{t}$/W events, another that estimated the prompt photon and jet faking photon contribution contributions from $t\bar{t}$/W events, a third that estimated events with fake $E_{\mathrm{T}}^{\mathrm{miss}}$ (predominantly γ+jets), and a fourth that estimated $Z \to \nu\nu$ events. The same general methodology is used for the 8 TeV version of the analysis. See Chapter 10 for more details on the background modeling techniques.

The total expected background for the 7 TeV ATLAS search was 7.5 $\pm$ 2.2 events, coming from 1.10 $\pm$ 0.14 electron-faking-photon events, 3.38 $\pm$ 1.83 prompt-photon or jet-faking-photon events, 2.7 $\pm$ 1.1 fake $E_{\mathrm{T}}^{\mathrm{miss}}$ events, and 0.3 $\pm$ 0.3 $Z \to \nu\nu$ events. The $E_{\mathrm{T}}^{\mathrm{miss}}$ distribution for predicted background, data, and sample signal points are shown in Figure 4.1. 7 events were observed, in excellent agreement with the background prediction.

Exclusion limits were set on squark, gluino, and gaugino production within a GGM framework. The NLSP neutralino branching ratios were held constant throughout the grids, with $\mathrm{Br}(\tilde{\chi}_1^0 \to h + \tilde{G}) \approx 56\%$, $\mathrm{Br}(\tilde{\chi}_1^0 \to \gamma + \tilde{G}) \approx 33\%$, and $\mathrm{Br}(\tilde{\chi}_1^0 \to Z + \tilde{G}) \approx 11\%$. The branching ratio of the Higgs boson to $b\bar{b}$ pairs is 74%. With these parameters, limits were set on the gluino mass of $m_{\tilde{g}} > 900$ GeV at 95% CL for 200 GeV $< m_{\tilde{\chi}_1^0} < m_{\tilde{g}}$, and on the squark mass of $m_{\tilde{q}} > 1020$ GeV at 95% CL for 200 GeV $< m_{\tilde{\chi}_1^0} < m_{\tilde{q}}$. In addition, neutralinos with 220 GeV $< m_{\tilde{\chi}_1^0} < 380$ GeV are excluded based on gaugino weak production only, independent of gluino and squark masses. The exclusion limits

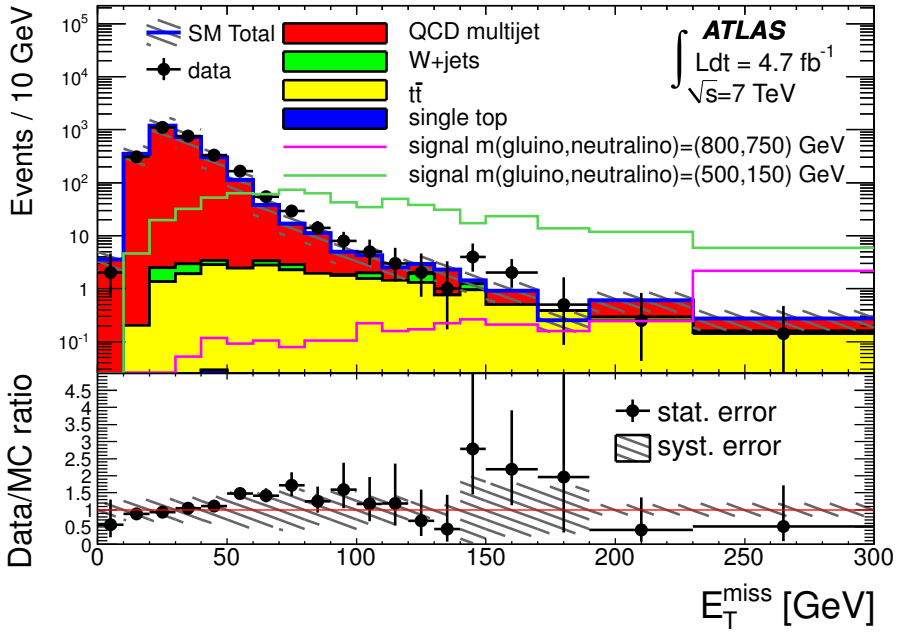

Figure 4.1: The $E_{\mathrm{T}}^{\mathrm{miss}}$ distribution for predicted background, data, and sample signal points for 7 TeV result [26].

for the squark and gluino grids can be seen in Figure 4.2.

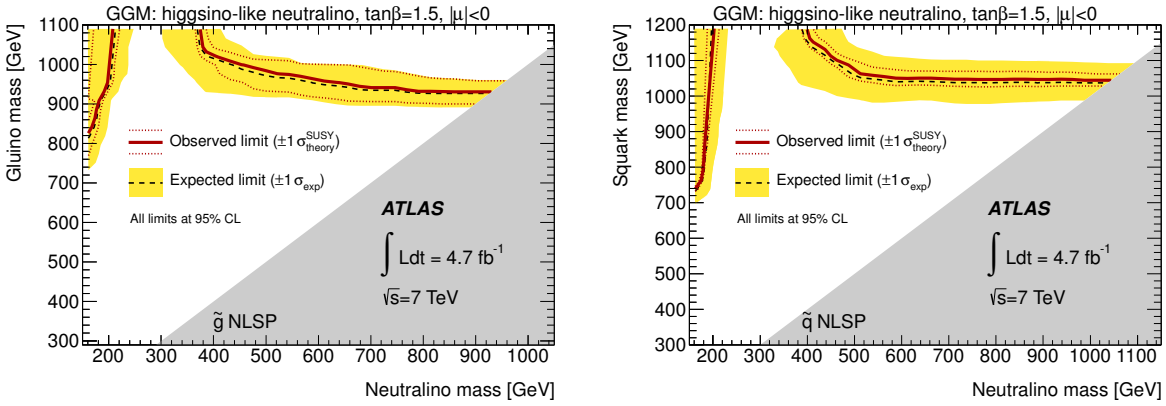

Figure 4.2: Excluded region in the gluino-neutralino (left) and squark-neutralino planes. Note the "chimney" structure for neutralino masses between 220 and 380 GeV where the exclusion is not dependent on gluino or squark mass [26].

Part II

Experimental Setup

Chapter 5

The Large Hadron Collider

Particle colliders are used to study fundamental particles and interactions. By using a particle detector to study the collision products, the presence of massive particles can be inferred, even if the particles are short-lived. In order to produce massive particles such as the Higgs boson or particles proposed by SUSY models at a significant rate, collisions must occur at high energies. The Large Hadron Collider (LHC) is the highest energy particle accelerator ever built, designed to produce proton-proton collisions with up to 14 TeV center of mass energy. The collisions used for this dissertation were produced by the LHC with $\sqrt{s} = 8$ TeV in 2012.

The LHC was approved by the CERN Council in December 1994 to be built in the 26.7 km circumference tunnel that formerly contained the Large Electron-Positron (LEP) collider [27]. The reason the LHC is able to produce higher energies than LEP, despite sharing the same tunnel, is due to synchrotron radiation, which obeys the relation

$$P \propto \frac{\gamma^4}{r^2}. \tag{5.1}$$

Due to the dependence of γ on the mass of the particle, synchrotron radiation is dramatically larger for electrons than protons. This means that protons can reach much higher energies than electrons in a tunnel of the same circumference.

5.1 LHC design

The LHC consists of two beams of protons traveling in opposite directions around the LHC tunnel. The same beampipe and magnetic field cannot be used for both beams as in a particle-antiparticle collider. The minimum tunnel diameter of 3.7 m is too small to use separate magnet rings for each proton beam, so a design utilizing twin-bore magnet design was adopted [27]. The minimum bunch spacing in the beams is 25 ns, which results in 3564 possible bunch spaces in each ring. A significant gap of 3 μs (119 bunches) must be left in each beam so that it can be safely aborted. In addition, due to the way the beams are injected, there are trains of 72 filled bunches followed by 12 empty bunches. This results in nominally having 2808 of the 3564 bunches filled. With 1.15×10^{11} protons per bunch, the design luminosity is $\mathscr{L} = 10^{34}$ cm^{-2}s^{-1}. Ultimately, the number of protons per bunch will increase to 1.7×10^{11}, which will push the luminosity to $\mathscr{L} = 2.3 \times 10^{34}$ cm^{-2}s^{-1} [27].

Protons are injected into the LHC rings with energy of 450 GeV. From there, they must be accelerated to the desired energy level. The injector chain that accelerates the protons to 450 GeV is discussed in Section 5.1.1. There are 4 main experiments using collisions from the LHC, discussed in Section 5.1.2. The LHC is designed to accelerate each beam to a maximum energy of 7 TeV, which requires a peak magnetic field of

8.33 T in the dipole magnets. This energy has not yet been achieved due to faulty interconnects limiting the current in the magnets, and thus the peak field strength. This issue is discussed further in Section 5.1.3.

5.1.1 Injection System

Before being injected into the LHC, protons pass through 4 other accelerators. Protons are accelerated first by Linac2 to 50 MeV. This is followed by the Proton Synchrotron Booster (PSB), which produces 1.4 GeV protons. Next is the Proton Synchrotron (PS), which maxes out at 25 GeV. Last is the Super Proton Synchrotron (SPS), which produces the 450 GeV protons that are injected to the LHC through two 2.5 km tunnels [27].

5.1.2 LHC Experiments

The LHC ring is divided into octants, with each octant consisting of one curved section and one straight section. The straight sections are about 528 m long and contain the beam crossings or utilities located in each of the octants. In four of the octants, collisions are provided to the major experiments in interaction regions called IR1, IR2, IR5, and IR8. The kicker magnets used for dumping the beams are located in IR6. IR3 and IR7 are used primarily for cleaning the beam and IR4 houses the RF and beam feedback systems used for accelerating the protons [27]. A diagram outlining the octants and their purposes is shown in Figure 5.1.

The 4 main experiments are called ATLAS, CMS, ALICE, and LHCb. ATLAS and CMS, located at IR1 and IR5, respectively, are general purpose detectors with

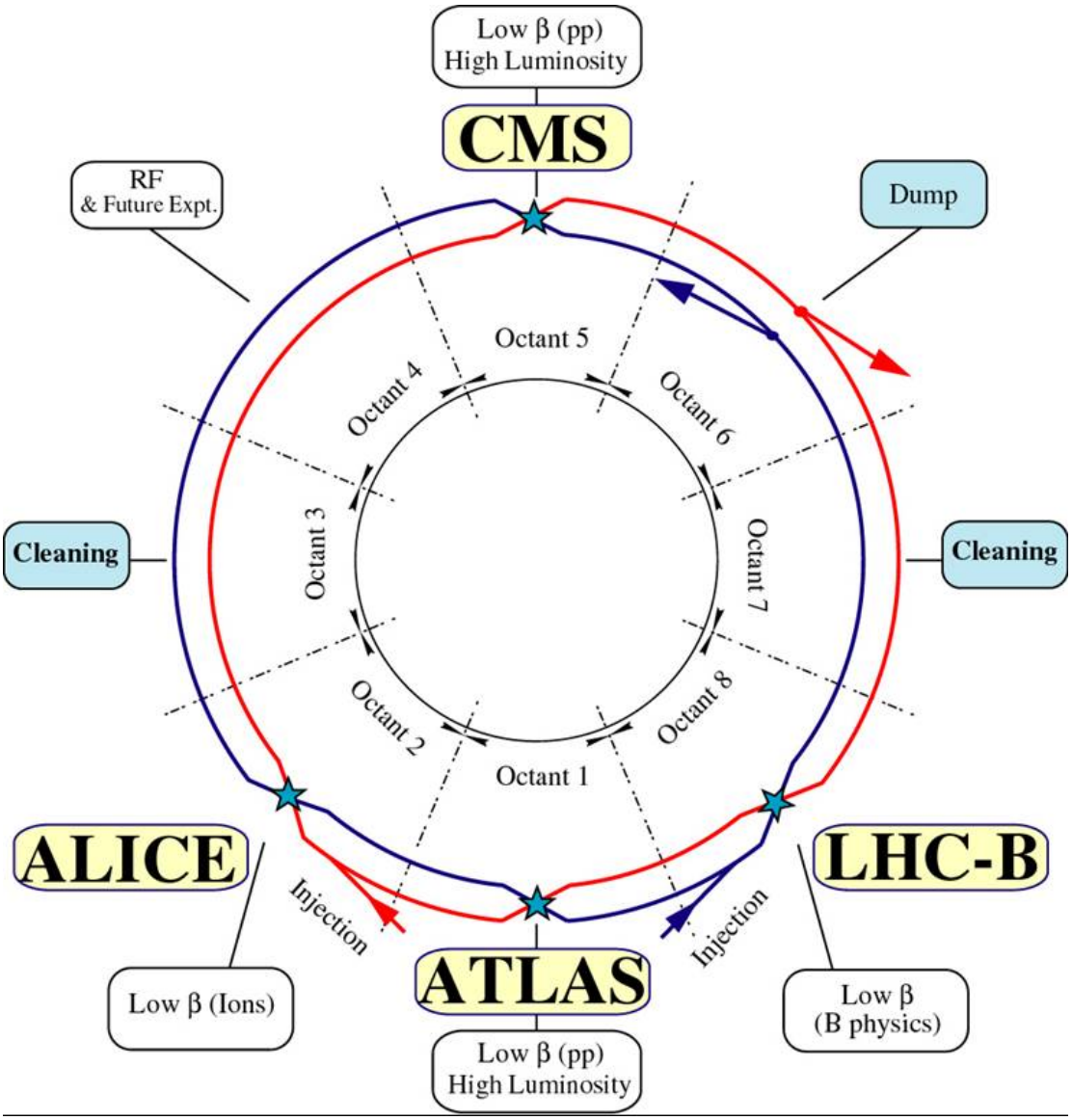

Figure 5.1: A schematic of the LHC storage ring [27]. The interaction points for ATLAS, ALICE, CMS, and LHCb are located in octants 1, 2, 5, and 8, respectively. The beam dump is located in octant 6.

sensitivity to a wide range of physics. ALICE and LHCb, located at IR2 and IR8, respectively, are more specialized. ALICE focuses on heavy ion collisions, while LHCb is optimized for physics related to the bottom quark. ATLAS and CMS are designed for high luminosity (LHC design luminosity of $\mathscr{L} = 10^{34}$ cm^{-2}s^{-1}), while ALICE and LHCb only receive a lower luminosity [27].

5.1.3 Magnet Quenching Incident

On September 19, 2008, during a powering test, an electrical arc occurred in one of the magnets, resulting in the release of helium and damage to around 700 m of the beamline [28]. The cause of this incident was determined to be a faulty interconnect between two magnets due to poor soldering, causing a resistance of approximately 220 nΩ, far exceeding the design specification of < 0.6 nΩ [28]. After the incident, other interconnects were found to have similar issues. The worst of these problems were fixed during the 2009 shutdown, but additional repairs were still needed during the 2013-14 shutdown [29]. The unfinished repairs limited the current that could be applied to the magnets, limiting the beam energy to 3.5-4 TeV during Run 1.

5.2 LHC Performance

During Run 1, the LHC ran predominantly with center-of-mass energy of $\sqrt{s}$ = 7 TeV (2010-2011) or $\sqrt{s} = 8$ TeV (2012). At $\sqrt{s} = 7$ TeV, the LHC delivered a total integrated luminosity of 5.626 fb^{-1} and 5.714 fb^{-1} to ATLAS and CMS, respectively. The maximum instantaneous luminosity delivered was $\mathscr{L} = 3.65 \times 10^{33}$ cm^{-2}s^{-1}, about a factor of 3 less than design luminosity. At $\sqrt{s} = 8$ TeV, the LHC delivered a total

integrated luminosity of 23 fb^{-1} to both ATLAS and CMS. The maximum instantaneous luminosity delivered was $\mathscr{L} = 7.73 \times 10^{33}$ $\text{cm}^{-2}\text{s}^{-1}$, just short of the design luminosity. The maximum number of colliding bunches during the 8 TeV run was 1380, with 50 ns bunch spacing [30]. Plots of the instantaneous and integrated luminosity throughout the 8 TeV run are shown in Figure 5.2.

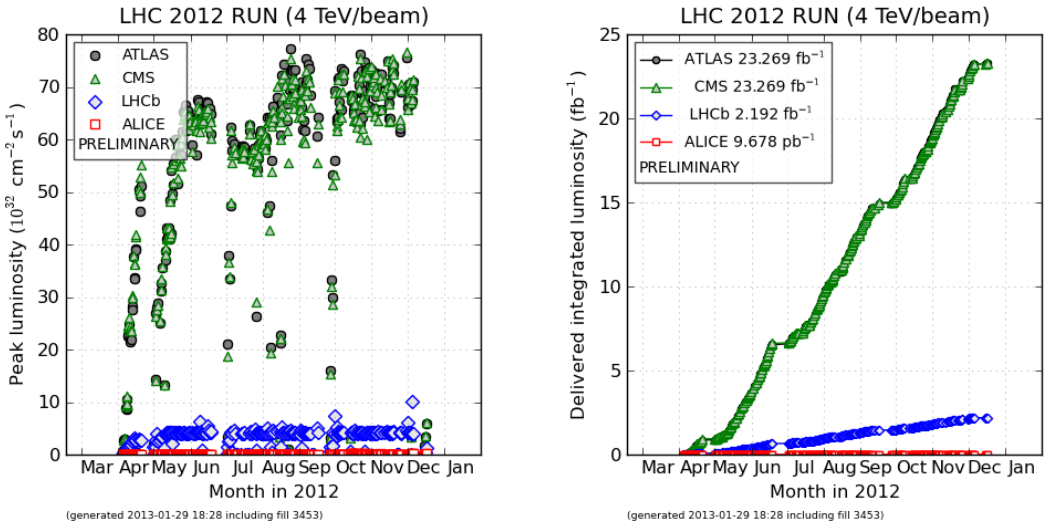

Figure 5.2: The peak instantaneous (left) and integrated (right) luminosity delivered by the LHC to the experiments as a function of time during the 8 TeV run in 2012 [30].

Chapter 6

The ATLAS Detector

The ATLAS (**A** **T**oroidal **L**HC **A**pparatu**S**) experiment is one one of four main experiments at the LHC. Along with CMS (**C**ompact **M**uon **S**olenoid), it is one of the two detectors that are considered general purpose, designed to be sensitive to a wide range of physics. ATLAS is located in an underground cavern at point 1 on the LHC ring. The detector is 25 meters tall and 44 meters long, with a weight of 7000 tons [31]. A computer-generated image of the detector is shown in Figure 6.1.

The ATLAS detector has several subsystems, each of which has an important role in identifying and measuring the energy of particles produced in the collisions. The group of detectors nearest the interaction point are collectively called the inner detector. The inner detector, discussed in Section 6.1, consists of three parts, ranging from a radius of a few centimeters to 1.15 meters from the interaction point. The calorimeter systems, discussed in Section 6.2, are located outside the inner detector. Outside the calorimeters are the muon spectrometer, discussed in Section 6.3. Tracking in the inner detector and muon spectrometer is aided by the presence of two magnet systems, discussed in Section 6.4. A multi-level trigger system, discussed in Section 6.6,

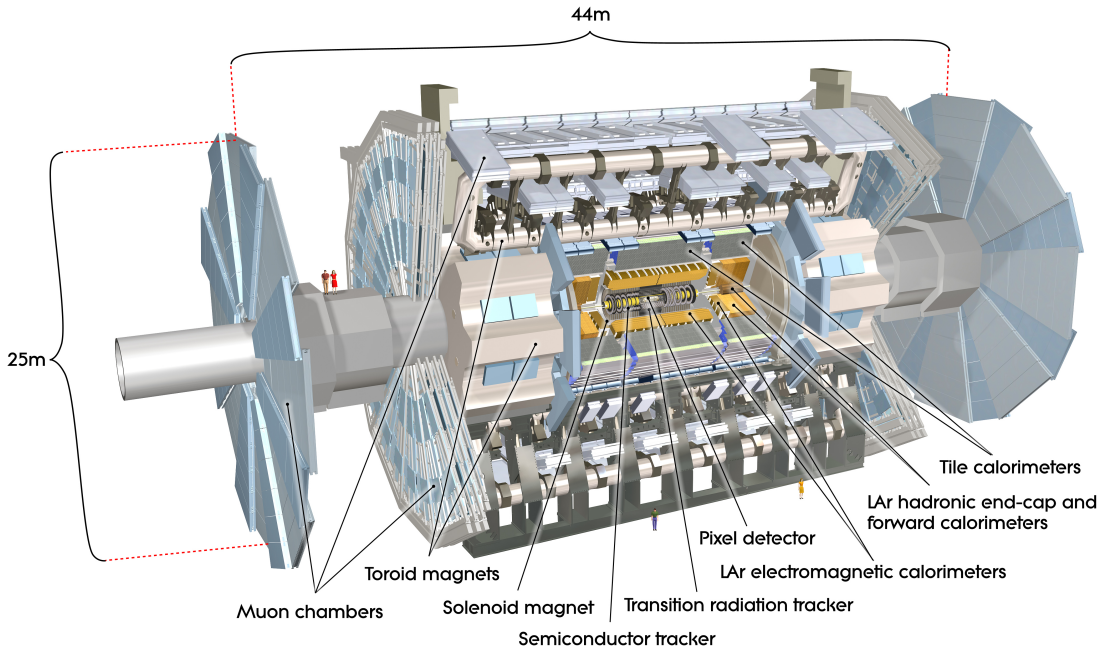

Figure 6.1: Cutaway image of ATLAS with labeled dimensions and labels of various detector subsystems [31]. Note the immense scale of the detector in relation to the images of people around the detector.

determines which events are kept and recorded, and which are thrown away.

ATLAS uses a coordinate system with the interaction point as the origin. The Cartesian coordinate system is defined with the z-axis along the beamline, corresponding to the axis of the cylindrical detector. The $x-y$ plane lies transverse to the beamline, and thus in the radial plane of the detector perpindicular to the axis. Positive z is taken to be the counter-clockwise direction viewing the LHC from above. Positive x is taken to be the direction pointing toward the center of the LHC ring, and positive y is taken to be upward toward the surface [31]. Note that interactions occur along a length of about 5 cm on the z-axis, so most interactions do not actually take place exactly at the origin of the coordinate system.

Due to the geometry of the events occuring in the detector, a somewhat unusual coordinate system is typically used. The variable r is defined as the radial distance from the z-axis. The azimuthal and polar angle with respect to the positive z-axis are defined as ϕ and θ, respectively. A quantity called pseudorapidity is defined as

$$\eta \equiv -\ln[\tan(\theta/2)]. \tag{6.1}$$

When written in terms of the particle momentum, psuedorapidity can be written as

$$\eta = \frac{1}{2}\ln\left(\frac{|\mathbf{p}| + p_z}{|\mathbf{p}| - p_z}\right). \tag{6.2}$$

When a particle is traveling at near the speed of light (or alternatively, the particle's mass is small relative to its momentum), its pseudorapidity converges to a quantity called rapidity, which is defined in particle physics as

$$y \equiv \frac{1}{2}\ln\left(\frac{E + p_z}{E - p_z}\right). \tag{6.3}$$

A difference in rapidity remains constant under a Lorentz boost in the z direction. This is important because in proton-proton collisions, it is actually partons within the protons that interact. These partons often have a momentum imbalance, leading to a boost in the z direction for the particles produced in the interaction. Pseudorapidity is preferred to rapidity because it is purely a geometric quantity that does not depend on the energy of the particle.

Any point in the detector is fully and uniquely described by the set of variables (r, η, ϕ). Note that along the z-axis, however, η reaches $\pm\infty$. The variable ΔR, the distance between two objects in the $\eta - \phi$ plane, is another important variable, defined as:

$$\Delta R \equiv \sqrt{(\Delta\eta)^2 + (\Delta\phi)^2} \tag{6.4}$$

Due to the fact that η is Lorentz invariant, ΔR is similarly invariant under Lorentz boosts in the z direction.

6.1 Inner Detector

The part of ATLAS that is nearest the beamline is the inner detector. Collectively, the inner detector reaches an outer radius of 1.15 m and is 7.0 m long (3.5 m in both positive and negative z directions). There are three detector systems that make up the inner detector, each with a barrel portion arranged in concentric circles around the beamline and an endcap portion made of disks perpendicular to the beamline. The innermost detector is the pixel detector (see Section 6.1.1), followed by the semiconductor tracker (see Section 6.1.2), and the transition radiation tracker (see Section 6.1.3). The

purpose of the inner detector is to detect charged particles in the volume with $|\eta| < 2.5$. The paths of the charged particles through the detector are inferred by combining hits in the different layers of the detector into tracks. Due to the 2T magnetic field provided by the central solenoid, described in Section 6.4.1, the p_{T} and sign of the charge of the track can be measured as well. The tracks can also be extrapolated back to the beamline to measure the interaction vertex. Images of the inner detector and its components can be seen in Figure 6.2. A cross section of the r-z plane of the inner detector can be seen in Figure 6.3.

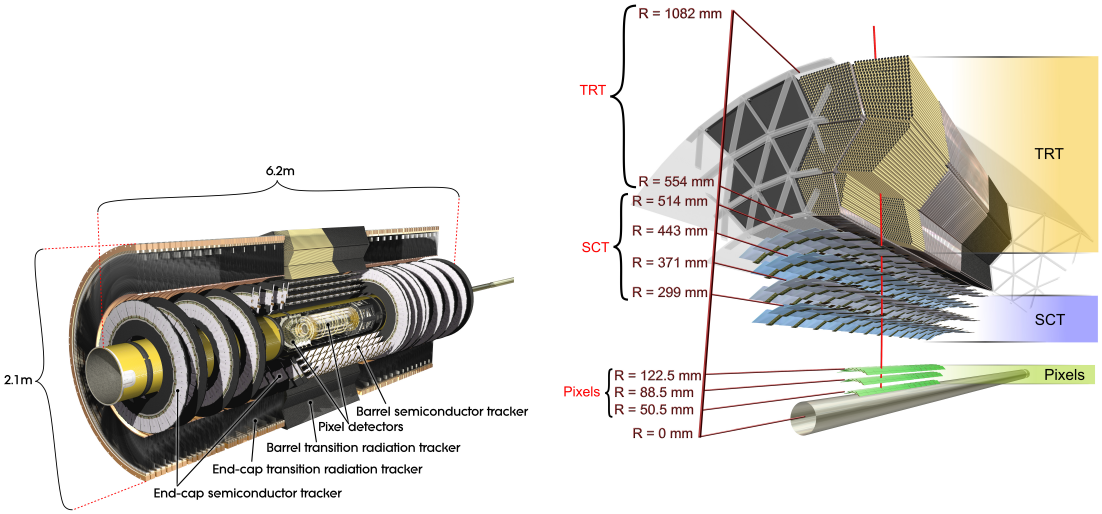

Figure 6.2: Cutaway view of the inner detector with subdetector labels (left) and a radial view of the inner detector barrel layers with distances from the beam pipe (right) [31].

6.1.1 Pixel Detector

The pixel detector barrel consists of three concentric cylinders at radii of 50.5, 88.5, and 122.5 mm, extending to ± 400.5 mm along the z-axis. The pixel detector

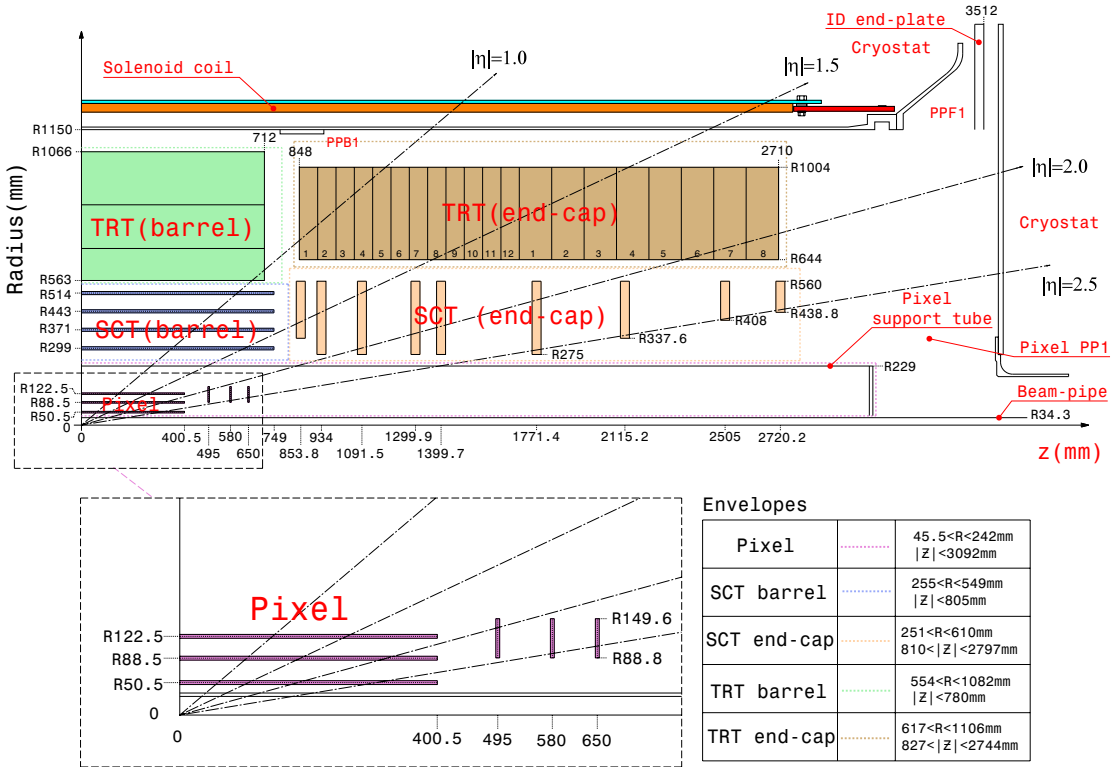

Figure 6.3: Cross section of one quarter of the ATLAS inner detector in the r-z plane. Positions of all of the subdetector layers are shown. [31]

endcaps consist of disks positioned at ±495, ±580, and ±650 mm along the z-axis. Each barrel and endcap consists of pixel modules. A module contains 46080 silicon pixels that each have their own readout channel. The pixels typically have dimensions of 50 μm x 400 μm, though about 10% measure 50 μm x 600 μm [31]. There are 1456 modules in the barrels and 288 modules in the endcaps, resulting in over 80 million readout channels in the pixel detector alone. This accounts for over half of the readout channels in the entire ATLAS experiment.

6.1.2 Semiconductor Tracker (SCT)

The semiconductor tracker (SCT) is located outside the pixel detector and detects charged particles using silicon strip detectors. There are four layers in the barrel of the SCT at radii of 299, 371, 443, and 514 mm, extending to ±749 mm along the z-axis. Each endcap has 9 disks at positions along the z-axis between ±854 and ±2720 mm. There are a total of 2112 modules in the SCT barrel and 1976 modules in the SCT endcaps. Each module contains two layers of 768 strips that need to be read out. There are 6.3 million total readout channels in the SCT.

Each strip in the SCT is 80 μm wide and 12 cm long. Due to their length, an individual strip only has resolution in one dimension. To get better resolution in the length dimension, each barrel layer or endcap has two strips that are angled by ±20 mrad with respect to each other [31]. In this way, a particle that hits both strips can be resolved in two dimensions by locating the position where the two strips overlap.

6.1.3 Transition Radiation Tracker (TRT)

The transition radiation tracker (TRT) is the outermost portion of the inner detector. The TRT uses straw tubes to detect charged particles, and is especially adept at discriminating electrons and positrons from other charged particles. The straw tubes are 4 mm in diameter, and contain a 31 μm gold-plated tungsten wire as the anode. Charged particles passing through the tube ionize the gas in the tube, which consists of 70% Xe, 27% CO_2, and 3% O_2 [31].

The TRT has two different thresholds for detection at 250 eV and 6 keV [31]. The high threshold hits are caused by particles with high Lorentz factors passing through materials of varying dielectric constants and producing transition radiation. This transition radiation produces additional ions in the straw tubes, and thus a stronger signal. Because electrons and positrons are so much lighter than other charged particles, they have higher Lorentz factors and produce more high threshold hits.

The TRT covers a volume out to $|\eta| = 2.0$. Each straw has a measurement accuracy of 130 μm in the R - ϕ plane. A charged particle passes through at least 36 straw tubes, except in the barrel-to-endcap transition region between $0.8 < \eta < 1.0$, where a track may pass through as few as 22 straws. A typical number of high threshold hits for electrons passing through the TRT with energies greater than 2 GeV is 7 to 10 [31].

6.2 Calorimeters

The purpose of the calorimeter system of ATLAS is to absorb and measure the energy of photons, electrons, and hadrons produced in collisions. Muons and neutrinos pass through the calorimeters, though muons do lose a small amount of energy. By looking at which calorimeter absorbs the energy and the tracks associated with the energy deposit, it is possible to distinguish between photons, electrons, and hadrons. The calorimeters are also used to measure a quantity called missing transverse energy; due to conservation of momentum and the purely longitudinal momentum of the incoming protons, the vector sum of the momentum of all objects should be zero in the transverse plane. Any deviation from zero can be used to infer the presence of a non-interacting particle, which is especially important in searches for supersymmetry with R-parity, as discussed in Section 3.4. In order to collect as much of the transverse energy produced in the event as possible, the calorimeters have the largest fiducial region of any detector in ATLAS, extending to $|\eta| = 4.9$. The calorimeters in ATLAS are sampling calorimeters, which effectively count the number of particles in the shower, then infer the initial energy from the number of particles counted and the length of the shower in the calorimeter. A labeled cutaway view of the different calorimeters is shown in Figure 6.4.

The innermost layer of the calorimeter system is referred to as the electromagnetic (EM) calorimeter. It is designed to absorb non-hadronic, electromagnetically interacting particles, especially photons and electrons. The EM calorimeter is at least

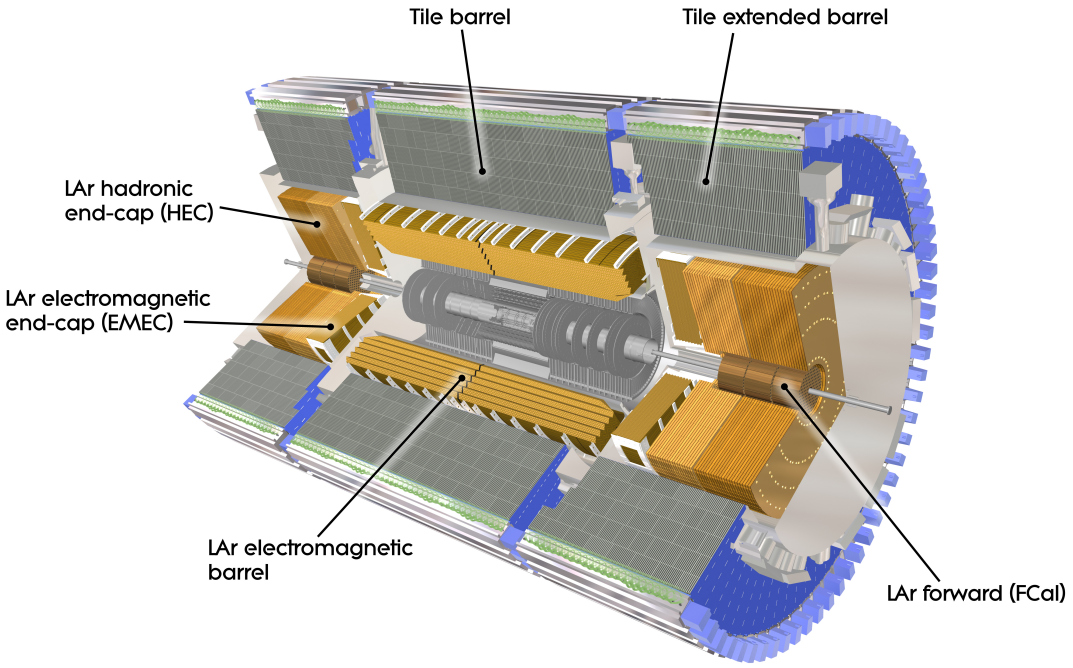

Figure 6.4: Cutaway view of the ATLAS calorimeter system with labels of the different sub-detectors [31].

22 radiation lengths (X_0) deep in the barrel and 24 X_0 deep in the endcaps [31]. It is built using liquid-argon (LAr) technology, and is described more in Section 6.2.1. It has a barrel region and endcap region, and provides coverage out to $|\eta| = 3.2$.

The outer portion of the calorimeter system is referred to as the hadronic calorimeter. It is designed to absorb and measure the energy of the hadrons produced in collisions, with a minimum number of nuclear interaction lengths (λ) of 9.7 λ in the barrel and 10 λ in the endcaps [31]. Inside the hadronic calorimeter, there are between 2 and 4 nuclear interaction lengths in the inner detector and electromagnetic calorimeter combined. The hadronic calorimeter has coverage out to $|\eta| = 4.9$, and is instrumented using both scintillating tile and liquid-argon technology. The hadronic calorimeter is described in Section 6.2.2.

6.2.1 Electromagnetic Calorimeter

The electromagnetic calorimeter uses liquid-argon technology to shower and measure the energy of electrons and photons. When a high energy electron or photon enters the calorimeter, electrons lose energy primarily through bremsstrahlung and photons lose energy primarily through electron-positron pair production. This causes a cascading shower that proceeds until the average energy is less than the critical energy, which is $\sim$10 MeV. At this point, the remaining energy dissipates through ionization; the ionization charge is collected by the calorimeter, with the total charge collected proportional to the energy of the incident particle.

The calorimater consists of between 2 and 4 layers that use lead as the absorber

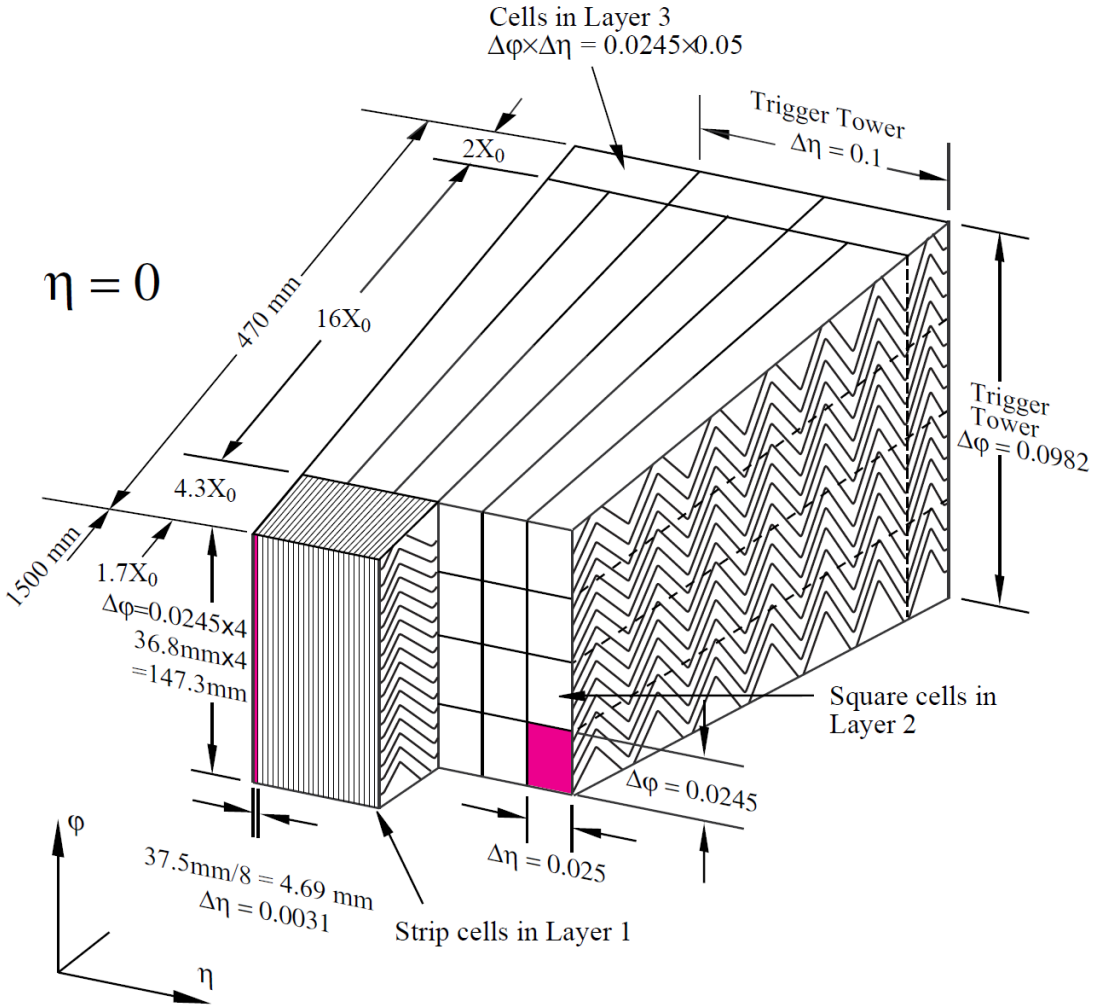

Figure 6.5: Schematic of the sampling layers of the LAr electromagnetic calorimeter. [31]

and liquid argon as the active material. It is divided into a barrel portion ($|\eta| < 1.475$) and an endcap portion ($1.375 < |\eta| < 3.2$). The presampling layer, responsible for collecting energy from showering caused by material in the inner detector, extends to $|\eta| = 1.8$. After the presampler, the first layer of the calorimeter consists of finely segmented strips that are important in distinguishing between photons and hadronic jets containing π^0s. The segmentation of the first layer varies in size between 0.025/8 x 0.1 and 0.025/4 x 0.1 in $\Delta\eta$ x $\Delta\phi$. There is a gap in the fine segmentation between the barrel and endcap regions for $|\eta|$ between 1.4 and 1.5. The segmentation of the second layer, which collects most of the EM energy of the event, varies between 0.025 x 0.025 and 0.1 x 0.1 in $\Delta\eta$ x $\Delta\phi$. The segmentation of the third layer is 0.05 x 0.025 in $\Delta\eta$ x $\Delta\phi$ throughout its entire acceptance [31]. A schematic of the sampling layers of the EM calorimeter is shown in Figure 6.5.

6.2.2 Hadronic Calorimeter

The hadronic calorimeter has components that use tile scintillators and others that use liquid-argon technology. The barrel uses steel as an absorber and scintillating tiles as the active material. It is placed directly outside the electromagnetic LAr calorimeter. There is a main barrel region for $|\eta| < 1.0$ and extended barrel regions with $0.8 < |\eta| < 1.7$. The first two layers have granularity of 0.1 x 0.1 in $\Delta\eta$ x $\Delta\phi$, while the third layer has granularity of 0.2 x 0.1 in $\Delta\eta$ x $\Delta\phi$.

The hadronic endcap calorimeter (HEC) consists of two wheels per endcap, located behind the wheels of the EM calorimeter. It covers the region of $1.5 < |\eta| <$

3.2. Like the EM calorimeter, the HEC uses LAr for the active medium. Instead of the lead used as an absorber by the EM calorimeter, the HEC uses copper as the absorber. There are four sampling layers in each endcap, with granularity of 0.1 x 0.1 for $1.5 < |\eta| < 2.5$ and 0.2 x 0.2 for $2.5 < |\eta| < 3.2$.

The forward calorimeter (FCal) consists of three modules in each endcap. The closest module to the interaction point on each side has a copper absorber and is optimized for electromagnetic measurements. The second and third modules in each endcap have a tungsten absorber and predominantly measure hadronic interactions. The FCal covers the far forward region, $3.1 < |\eta| < 4.9$ [31].

6.3 Muon Spectrometer

Figure 6.6 shows the different systems involved in the muon system. There are four types of detectors represented: monitored drift tubes (MDT), cathode strip chambers (CSC), resistive plate chambers (RPC), and thin gap chambers (TGC). The precision tracking is done by the MDT and CSC for $|\eta| < 2.7$. A secondary measurement of the muon and triggering is done by the RPC and the TGC. These detectors also have coverage for $|\eta| < 2.7$, though triggering is only available for $|\eta| < 2.4$. The magnetic field for these detectors are provided by the barrel toroids for $|\eta| < 1.4$ and by the endcap toroids for $1.6 < |\eta| < 2.7$. In the transition region of $1.4 < |\eta| < 1.6$, both toroids contribute to the magnetic field [31].

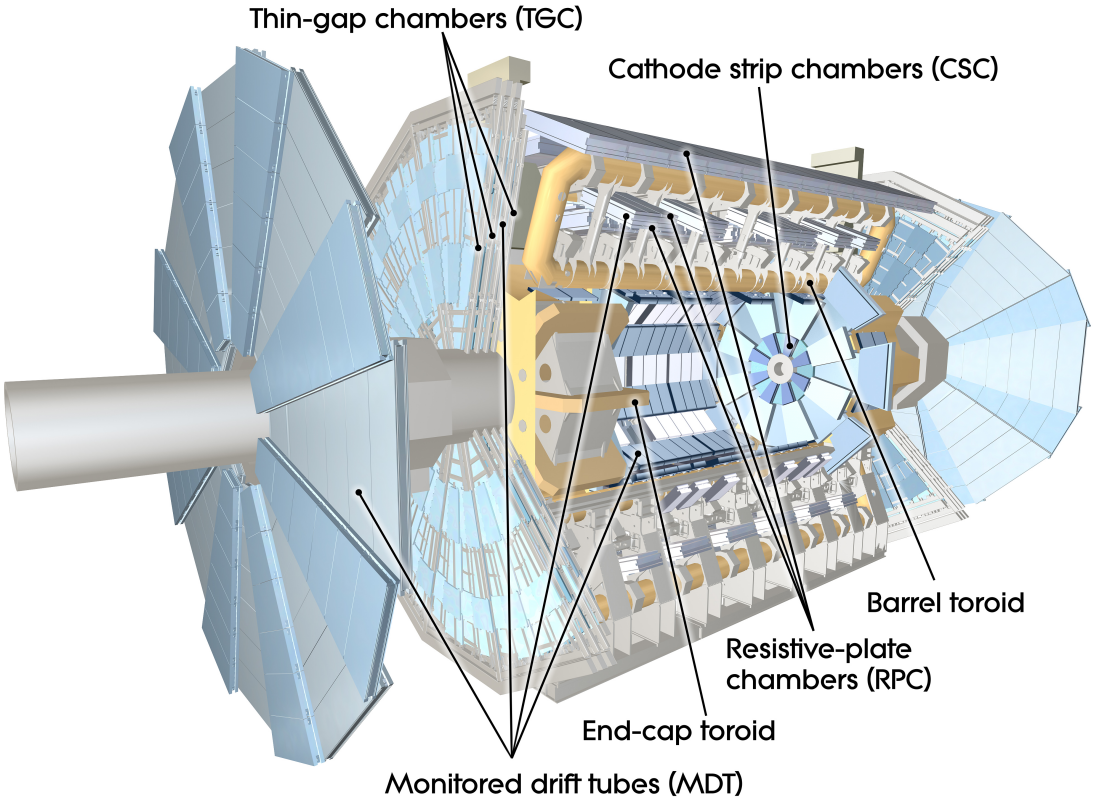

Figure 6.6: Cutaway view of the ATLAS muon system [31].

6.4 Magnet Systems

There are two main magnet systems in the ATLAS detector, the central solenoid (see Section 6.4.1) that produces the field for the inner detector, and the toroidal magnets (see Section 6.4.2) that produces the field for the muon system.

6.4.1 Central Solenoid

The solenoid magnet is located between the TRT and the LAr calorimeter. It produces a 2T field in the inner detector along the z-axis, which causes the tracks of charged particles to bend primarily in the ϕ direction. This allows the p_{T} and charge of tracks to be measured. The solenoid is a superconducting NbTi coil cooled to 4.5 K. In order to reduce the material thickness inside the calorimeter, the solenoid and the LAr calorimeter share a vacuum vessel, thus eliminating two vacuum walls from the design [31].

6.4.2 Toroidal Magnets

A system of three large toroids generates the magnetic field for the muon spectrometer. There are two endcap toroids that line up with the central solenoid on either end and a barrel toroid. Each consists of eight coils that are assembled radially and symmetrically about the beam axis. The endcap toroids are rotated 22.5° from the barrel toroid in order to optimize the bending power in the region where both fields are used [31].

6.5 Luminosity Calculation

The luminosity of a proton-proton collider can be expressed as

$$\mathscr{L} = \frac{R_{inel}}{\sigma_{inel}} \tag{6.5}$$

where R_{inel} is the rate of inelastic collisions and σ_{inel} is the pp inelastic cross section. For a collider operating at a revolution frequency f_r with n_b bunch crossings at the interaction point, this can be rewritten as

$$\mathscr{L} = \frac{\mu n_b f_r}{\sigma_{inel}} \tag{6.6}$$

where μ is the average number of inelastic interactions per bunch crossing. Therefore, the instantaneous luminosity can be determined using any method that measures the ratio μ/σ_{inel} [32].

ATLAS relies on event counting techniques to calculate this quantity. An "event" is counted when a bunch crossing has at least one pp interaction that induces at least one hit in the detector being considered. The quantity ε can be defined as the efficiency for one inelastic pp collision to satisfy the event selection criteria, and $\mu_{vis} \equiv \varepsilon\mu$ is the average number of visible inelastic interactions per bunch crossing. The visible cross section is also defined, as $\sigma_{vis} \equiv \varepsilon\sigma_{inel}$. With these definitions, the luminosity can be rewritten as

$$\mathscr{L} = \frac{\mu n_b f_r}{\sigma_{inel}} = \frac{\mu_{vis} n_b f_r}{\sigma_{vis}}. \tag{6.7}$$

To calculate μ_{vis}, several detectors and algorithms are used, assuming Poisson statistics in the μ_{vis} distribution. The central value is selected from the different algorithms, with the remaining algorithms used as a check on the stability of the measurement. The detectors used include the Inner Detector, the Minimum Bias Trigger Scintillators (MBTS), the LAr calorimeter, the Beam Conditions Monitor (BCM), the LUminosity measurement using Cerenkov Integrating Detector (LUCID), and the Zero-Degree Calorimeter (ZDC) [32].

The quantity σ_{vis} is calculated using beam-seperation scans originally proposed by van der Meer [33]. The absolute luminosity during these scans can be calculated using the relation

$$\mathscr{L} = \frac{n_b f_r n_1 n_2}{2\pi \Sigma_x \Sigma_y} \tag{6.8}$$

where n_1 and n_2 are the numbers of particles in the two colliding bunches and Σ_x and Σ_y characterize the widths of the horizontal and vertical beam profiles [32]. By scanning the beams across each other in the horizontal and vertical directions, the quantities Σ_x and Σ_y can be calculated. Calculating $\mathscr{L}$ using Equation 6.8 and the value μ_{vis} during the scan, σ_{vis} can be extracted from Equation 6.7. The value of σ_{vis} is assumed to be stable over the data taking period, so the calibration is done with only a few scans.

6.6 Trigger System

Due to the immense amount of data collected by ATLAS, not every bunch crossing can be stored and analyzed. With the bunch spacing of 50 ns used for the 8

TeV run, a potential event rate of 20 MHz is possible. To reduce this rate to a more manageable 200 Hz that can actually be recorded to disk, some discrimination between interesting and uninteresting events is needed. The trigger system must quickly and accurately determine which events need to be kept.

The trigger system is designed with three levels: level 1 (L1), level 2 (L2), and the event filter (EF). The first level of the trigger is L1. It uses limited information from the calorimeters and muon system to attempt to identify photons, electrons, jets, or muons above some p_{T} threshold. It has to make a decision on each event in less than 2.5 μs, and reduces the event rate to about 75 kHz [31].

Events that pass the L1 trigger are passed along to the L2 trigger. The L2 trigger is passed information on specific regions of interests (RoI's) that the L1 trigger flagged as potentially interesting. The full detector information for the RoI is then used to make a decision on the event. The L2 trigger has about 40 ms to make a decision on each event, and reduces the event rate to about 3.5 kHz [31]. If an event passes L2, it is passed to the event filter, which uses complex algorithms to make a final decision on the event in around 4 s.

In some cases, only a certain fraction of events that pass a particular trigger are kept and written. This is called prescaling, which is done when a particular signature is desired but occurs at too high a rate for all events to be kept. For example, a trigger that has a prescale of 25 would throw away 24 passing events for each event that is passed along to the next trigger level (or written in the case of the event filter). For an event to be written, it must pass through L1, L2, and the event filter, including any

prescales. An example trigger chain might be looking for 30 GeV of localized energy in the EM calorimeter at L1, an 80 GeV loose photon in an RoI passed from L1 at L2, and a 120 GeV loose photon in the event at EF.

Part III

The Analysis

Chapter 7

Data and Monte Carlo Samples

7.1 Dataset and Trigger Studies

This analysis is based on a sample of pp collision events recorded at $\sqrt{s} = 8$ TeV with the ATLAS detector in 2012. The standard Good Run List [1] (GRL) criterion is applied to select events from luminosity blocks during periods when all necessary detector components were working as expected. Selected luminosity blocks are required to have both the solenoid and toroid magnets operating at their nominal field strengths to allow good momentum measurements for electrons and muons. Further, it is required that each of the sub-detectors' responses and the performance for photon, electron, muon, and jet identification, as well as energy and momentum computations, do not deviate from their expected behavior. This includes the systems needed for missing transverse momentum reconstruction, as well as the trigger systems required for photon selection.

The collected integrated luminosities split up by run period are shown in Table 7.1.

[1] data12_8TeV.periodAllYear_DetStatus-v61-pro14-02_DQDefects-00-01-00_PHYS_StandardGRL_All_Good.xml

Table 7.1: Integrated luminosity used in this analysis. For each data taking period the run range and the integrated luminosity are given.

Period	Run range	Luminosity [pb^{-1}]
A	200804–201556	795.91
B	202660–205113	5113.61
C	206248–207397	1409.06
D	207447–209025	3297.54
E	209074–210308	2534.11
G	211522–212272	1279.54
H	212619–213359	1449.04
I	213431–213819	1018.45
J	213900–215091	2605.48
L	215414–215643	841.634
Total	200804–215643	20344.37

The trigger used in the presented analysis is a photon trigger, `g120_loose`. It requires a photon to pass the loose criteria and to have $p_T^\gamma > 120$ GeV. The efficiency relative to cut selection of this trigger as a function of p_T^γ is shown in Figure 7.1. It is measured from data using events which pass a diphoton trigger. The histograms show the fraction of events that pass the `g120_loose` trigger and the `g35_loose_g25_loose` trigger divided by all events that pass the `g35_loose_g25_loose` trigger, as a function of p_T^γ. It is clear that for our offline selection it is nearly 100% efficient, with at least 97% efficiency at 125 GeV and over 99% efficiency at 130 GeV. Similar histograms are shown for a Sherpa Z→ee MC sample in Figure 7.2.

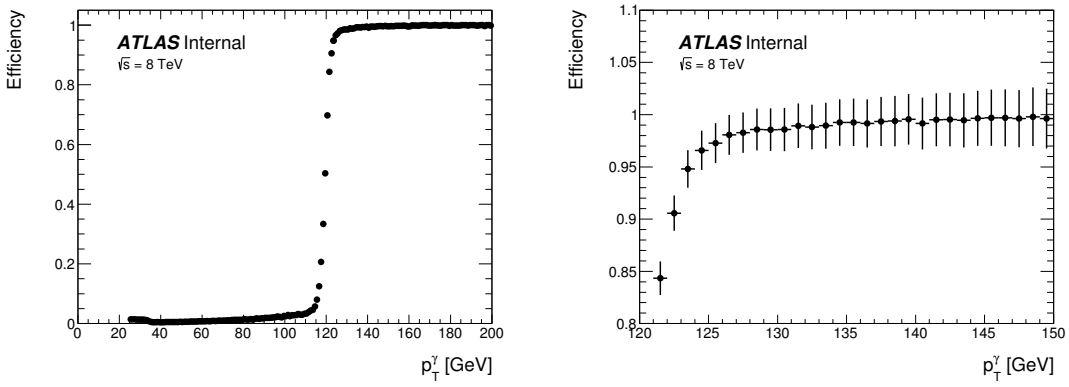

Figure 7.1: The trigger efficiency as a function of p_T^γ in data (left) and the same histogram focused on the region around 125 GeV (right).

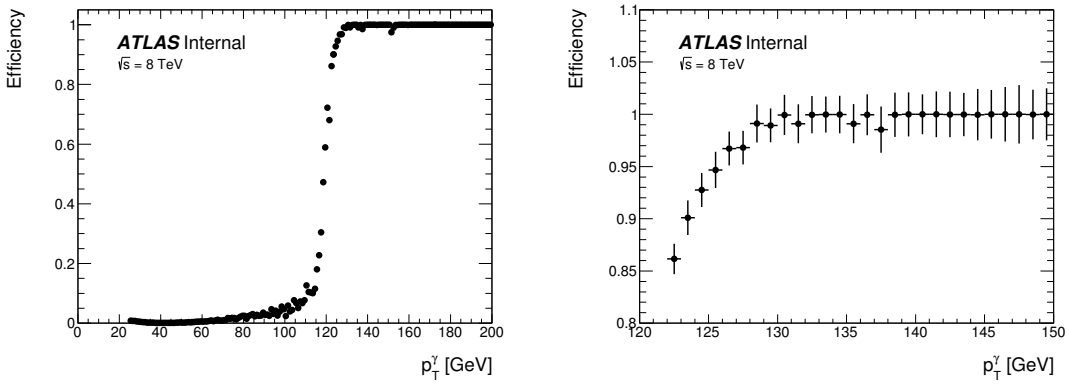

Figure 7.2: The trigger efficiency as a function of p_T^γ in Sherpa Z→ee MC (left) and the same histogram focused on the region around 125 GeV (right).

7.2 Monte Carlo simulated samples

The results presented in the following sections are compared to expectations based on Monte Carlo (MC) simulations. The signal and background samples used were generated using the mc12a MC settings at $\sqrt{s} = 8$ TeV. All signal and background samples are passed through either `GEANT4`-based full simulation [34] or ATLFAST-II fast simulation [35] of the ATLAS detector. After simulation (full or fast), the events are passed through the same reconstruction software as used for data [35]. All Monte Carlo samples add minimum bias events generated using Pythia 8 [36] to simulate varying levels of pileup interactions. The ATLAS pileup reweighting tool is used to scale simulated events to match the pileup levels of the data sample, with a mean number of interactions per beam crossing of 20.1.

The samples used for SM background are summarized in Section 7.2.1. However, the analysis does not rely heavily on these simulations. Background is estimated, whenever possible, from the data itself. As a cross-check, the data-based background expectations are compared with results from simulation and show good agreement. The simulated background samples are also used in studies performed to optimize the signal regions. In the tables in this section, the column labeled 'DSID' contains the 'dataset ID' numbers which are used for reference by the ATLAS collaboration.

The samples used for the GGM signal are summarized in Section 7.2.2. These samples are used to set limits for a region of the GGM phase space based on production of both strongly and weakly produced supersymmetric particles.

7.2.1 Background Simulation

Several SM processes can result in events with a photon, b-jets and $E_{\mathrm{T}}^{\mathrm{miss}}$. This section discusses the Monte Carlo samples used to model each of these processes.

7.2.1.1 Top pair ($+\gamma$) production

The most important background for this analysis is $t\bar{t}$ pairs. Due to the presence of b-jets and neutrinos (in semileptonic and dileptonic events), a high p_{T} photon is key to $t\bar{t}$ events passing the selection. A high p_{T} photon can either be prompt or fake. Fakes are usually due to an electron from a W decay being misidentified as a photon. The sample used for standard $t\bar{t}$ production is generated with POWHEG [37]. This sample is normalized using the approximate next-to-next-to-leading-order (NNLO) calculation of 253 pb and the non-hadronic decay branching ratio of .543 [38]. For this sample, the showering was done using PYTHIA6 [39] using the Perugia 2011C tune [40]. The CTEQ6L1 parton distribution functions [41] are used for this tune.

Due to poor modeling of ISR/FSR photons in the POWHEG $t\bar{t}$ sample (discussed in Section 10.1.3), a $t\bar{t}$ $+\gamma$ sample is also used. The $t\bar{t}$ $+\gamma$ sample is generated using MADGRAPH [42], which allows a full calculation of the seven-particle final states $l\nu_l q\bar{q}'b\bar{b}\gamma$ and $l\nu_l l'\nu_{l'}b\bar{b}\gamma$ (with $l/l' = e, \mu, \tau$), taking into account all possible contributing diagrams at leading order (LO). These events are generated using the CTEQ6L1 parton distribution function, and hadronized with PYTHIA6. A generator-level cut is made on the photon p_{T} at 80 GeV. The cross section times branching ratio for the generated $t\bar{t}\gamma$ sample is 0.099 pb at a center-of-mass energy of 8 TeV. In order to scale the LO Monte

Carlo sample to the next-to-leading-order (NLO) prediction a K-factor of 1.9 ± 0.4 is estimated [43, 44], resulting in a cross section of 0.188 pb.

A comparison of the prompt photon p_{T} spectra, shown in Fig. 7.3, of both generators reveals that the MadGraph program gives rise to a harder photon spectrum than Powheg. Additionally, the MadGraph sample results in a factor of 8 more events than the Powheg sample. In this figure, events in the Powheg sample are only included if the photon is prompt (determined from truth information) and passes the phase space cuts required for the Madgraph sample, which include cuts on the photon of $|\eta| < 5$ and $\Delta R < 0.1$ with respect to any quark or lepton from the hard scatter. The harder spectrum enhances the probability of a Madgraph-generated $t\bar{t}\gamma$ event to survive the signal selection procedure. Due to the dramatic difference between the Powheg sample and the Madgraph sample, the Powheg sample is not sufficient to describe high p_{T} prompt photons. Events in the Powheg sample in which the photon is prompt (as determined from truth information) are not counted in order to avoid double counting of these events. Similarly, high p_{T} photon samples have been produced for single top, W, and Z production in order to get more accurate results by having samples with higher luminosity in the high p_{T} photon regime. The cross sections and luminosities for the $t\bar{t}$ samples are summarized in Table 7.2.

Table 7.2: List of simulated $t\bar{t}$ samples that are used for rough background evaluation in the analysis.

Process	Generator	DSID	Number of events	σ [pb]	$\int \mathscr{L}\,dt$ [fb^{-1}]	Fast/FullSim
$t\bar{t}$	Powheg	117050	99910976	137	727	Fast
$t\bar{t}\gamma$	MadGraph	177998	200000	0.187	1070	Fast

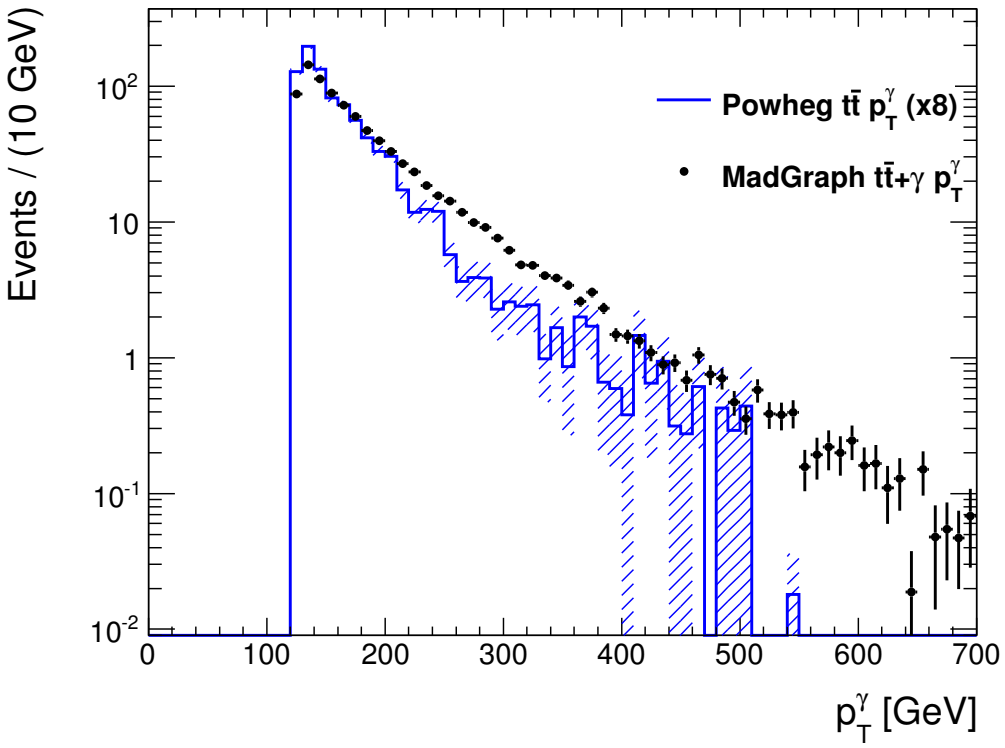

Figure 7.3: Comparison of the photon p_{T} spectrum as predicted by MADGRAPH $t\bar{t}\gamma$ and by POWHEG $t\bar{t}$. Histograms are normalized to 20.34 fb^{-1}. The POWHEG sample is magnified by a factor of 8.

7.2.1.2 Single top ($+\gamma$) production

Single top production is also an important background due to the presence of b-jets and neutrinos in leptonic events. Like $t\bar{t}$ pairs, if there is a high p_{T} photon reconstructed, then the event can possibly pass the selection. Single top production can be separated into three different production modes: Wt, s-channel, and t-channel. For the inclusive samples, POWHEG is used to generate Wt and s-channel events. The t-channel samples are generated using ACERMC [45]. For each of these samples, the showering was done using PYTHIA6 using the Perugia 2011C tune and the CTEQ6L1 PDF.

The prompt photon samples are produced using the WHIZARD [46] generator and showered with PYTHIA6 using the Perugia 2011C tune and the CTEQ6L1 PDF. The extra photon can be produced either during production or during the subsequent decays. Production and decay were treated separately, however, so interference effects are ignored. Prompt photon samples are only used for Wt and t-channel events. There are two t-channel samples: the first (DSID 202621) has the photon produced along with the top quark, and the second (DSID 202622) has the photon produced in the top quark decay. There are nine Wt samples. They are separated into groups of three based on whether the W, t, or both decay leptonically. They are further divided based on whether the photon is produced with the W and t or in the decay of either the t or W. Events from the POWHEG/ACERMC with prompt photons (determined from truth information) and passing the phase space cuts of the prompt photon samples are

removed samples in order to avoid double counting. The photon p_{T} distributions of the inclusive and prompt photon samples are shown in Figure 7.4. The prompt photon samples result in about a factor of 3 larger contribution than the inclusive samples, and also result in a harder p_{T} spectrum. NNLO cross sections and luminosities for single top samples are listed in Table 7.3.

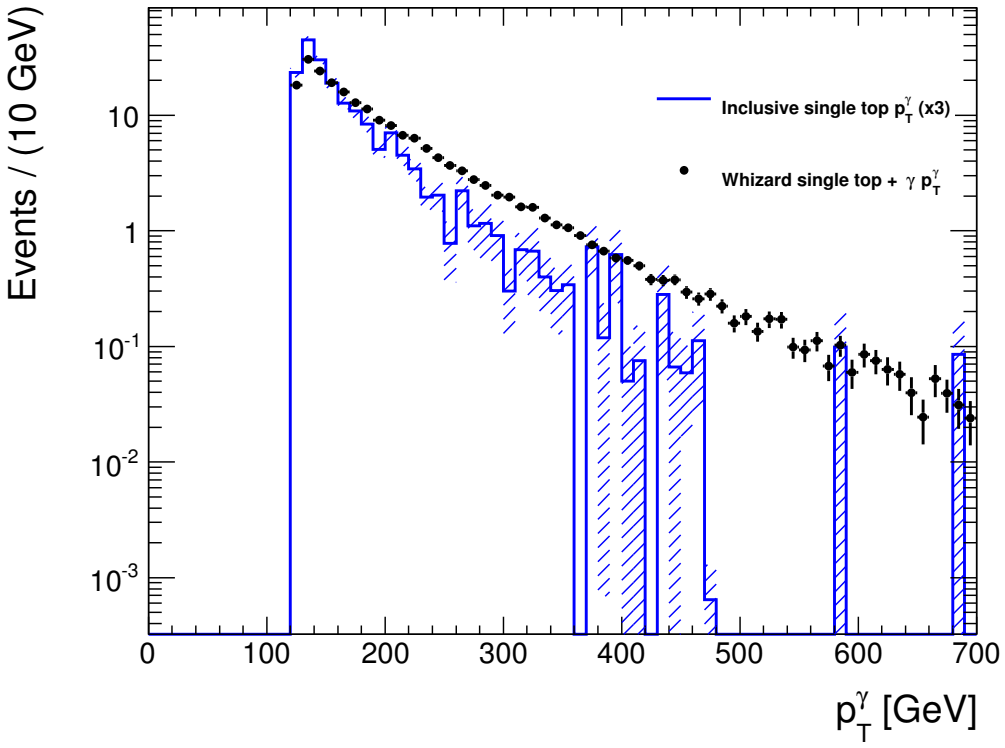

Figure 7.4: Comparison of the photon p_{T} spectrum as predicted by WHIZARD single top + γ and by inclusive single top. Histograms are normalized to 20.34 fb^{-1}. The inclusive samples are magnified by a factor of 3.

7.2.1.3 W ($+\gamma$/jets) production

W production with leptonic decays can also pass the selection if produced with $b\bar{b}$ pairs and if a high p_{T} photon is reconstructed. This is more rare than in the case

Table 7.3: List of simulated single top samples that are used for rough background evaluation in the analysis.

Process	Generator	DSID	Number of events	σ [pb]	$\int \mathscr{L} dt$ [fb^{-1}]	Fast/FullSim
t-channel	AcerMC	110101	7704356	28.4	271	Full
Wt	Powheg	110140	19947984	22.4	892	Fast
s-channel	Powheg	110119	5995993	1.82	3299	Fast
t-channel + γ	Whizard	202621	109999	0.0228	4810	Fast
t-channel + γ (t decay)	Whizard	202622	20000	.00406	4930	Fast
Dilepton $Wt\gamma$	Whizard	202623	5000	.00212	4710	Fast
Dilepton $Wt\gamma$ (t decay)	Whizard	202624	5000	.000418	12000	Fast
Dilepton $Wt\gamma$ (W decay)	Whizard	202625	5000	.000785	6370	Fast
t lepton $Wt\gamma$	Whizard	202626	20000	.00420	4770	Fast
t lepton $Wt\gamma$ (t decay)	Whizard	202627	5000	.000803	6230	Fast
t lepton $Wt\gamma$ (W decay)	Whizard	202628	5000	.000750	6660	Fast
W lepton $Wt\gamma$	Whizard	202629	20000	.00418	4790	Fast
W lepton $Wt\gamma$ (t decay)	Whizard	202630	5000	.00344	5920	Fast
W lepton $Wt\gamma$ (W decay)	Whizard	202631	5000	.00157	3180	Fast

of $t\bar{t}$ or single top where b-jets are always present, but due to W production having a higher cross section, the resulting contribution is comparable in size. The inclusive W samples are generated with Sherpa [47] using the NLO PDF set CT10 with up to 4 jets in the matrix element. Only leptonic decays are considered because hadronic decays do not produce $E_{\mathrm{T}}^{\mathrm{miss}}$ unless there is a mismeasurement. The samples are divided by W p_{T} and by flavor of the additional jets, which allows for higher luminosity in higher W p_{T} events and b-tagged events. Samples are also produced with massive bottom and charm quarks. Due to the large number of samples, the tables summarizing the inclusive samples are in Appendix A.

The prompt photon samples are also produced using Sherpa and the NLO PDF set CT10. The samples contain up to 3 additional jets in the matrix element. Each sample has a filter requiring a photon with $p_{\mathrm{T}} > 80$ GeV. Events with prompt photons (determined from truth information) and passing the phase space cuts of the

prompt photon samples are removed from the inclusive samples in order to avoid double counting. The photon p_{T} distributions of the inclusive and prompt photon samples are shown in Figure 7.5. The prompt photon samples result in about a factor of 6.5 larger contribution than the inclusive samples and also result in a harder p_{T} spectrum. NLO cross sections and luminosities are shown in Table 7.4.

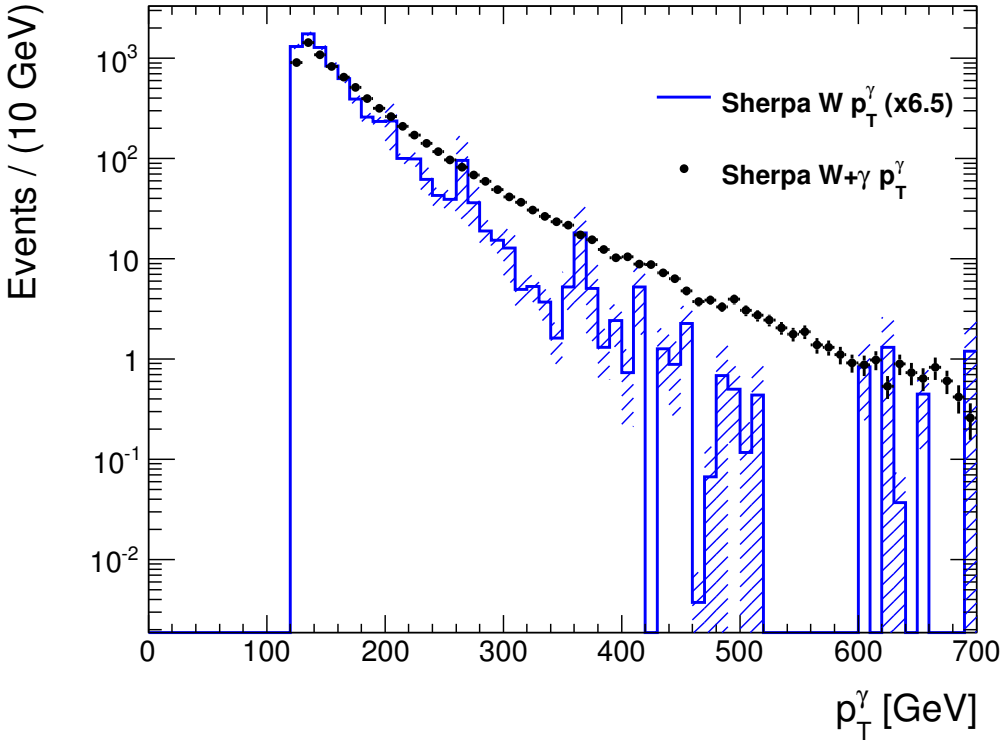

Figure 7.5: Comparison of the photon p_{T} spectrum as predicted by Sherpa $W\gamma$ samples and by Sherpa inclusive W samples. Histograms are normalized to 20.34 fb^{-1}. The inclusive samples are magnified by a factor of 6.5.

7.2.1.4 Z ($+\gamma$/jets) production

Z production with neutrino decays can also pass the selection if produced with $b\bar{b}$ pairs and if a high p_{T} photon is reconstructed. When the Z decays to charged

Table 7.4: List of simulated $W+\gamma$ samples that are used for rough background evaluation in the analysis. All samples are generated using SHERPA.

Process	DSID	Number of events	σ [pb]	$\int \mathscr{L} dt$ [fb^{-1}]	Fast/FullSim
$W \to e\nu+\gamma$	126741	499995	0.719	695	Full
$W \to \mu\nu+\gamma$	126744	499997	0.718	696	Full
$W \to \tau\nu+\gamma$	158727	500000	0.720	694	Full

leptons, it is extremely unlikely to pass the selection cuts due to the lack of genuine $E_{\mathrm{T}}^{\mathrm{miss}}$; however, these events could potentially survive the cuts for a control region requiring a lepton. The inclusive Z samples are generated with SHERPA using the NLO PDF set CT10 with up to 4 jets in the matrix element. The samples are divided by Z p_{T} and by flavor of the additional jets, which allows for higher luminosity in higher Z p_{T} events and b-tagged events. Samples are also produced with massive bottom and charm quarks. Due to the high number of samples, the tables summarizing the inclusive samples are in Appendix A.

The prompt photon samples are also produced using SHERPA and the NLO PDF set CT10. The samples contain up to 3 additional jets in the matrix element. Each sample has a filter requiring a photon with $p_{\mathrm{T}} > 70$ GeV. Events with prompt photons are removed from the inclusive samples in order to avoid double counting. NLO cross sections and luminosities are shown in Table 7.5.

Table 7.5: List of simulated $Z+\gamma$ samples that are used for rough background evaluation in the analysis. All samples are generated using SHERPA.

Process	DSID	Number of events	σ [pb]	$\int \mathscr{L} dt$ [fb^{-1}]	Fast/FullSim
$Z \to \nu\nu+\gamma$	126022	5499806	0.762	7210	Full
$Z \to ee+\gamma$	158728	198997	0.186	1070	Full
$Z \to \mu\mu+\gamma$	158729	199999	0.185	1080	Full
$Z \to \tau\tau+\gamma$	158730	200000	0.185	1080	Full

7.2.1.5 Diboson production

Diboson $WW/WZ/ZZ$ production can potentially enter into the signal region if a high p_{T} photon is reconstructed and if a real or fake b-jet is tagged. This is a rare occurence and is a much smaller contribution than other backgrounds with vector bosons decaying leptonically. The diboson samples used are produced with SHERPA using the NLO PDF set CT10 with up to 3 jets in the matrix element. These samples also have massive bottom and charm quarks. The samples are summarized in Table 7.6.

Table 7.6: List of simulated diboson samples that are used for rough background evaluation in the analysis. All of the samples are generated using the SHERPA generator.

Process	DSID	Number of events	σ [pb]	$\int \mathscr{L} dt$ [fb^{-1}]	Fast/FullSim
$WW \to ll\nu\nu$	177997	7999389	5.61	1420	Full
$WZ \to lll\nu$	177974	2699393	10.2	264	Full
$WZ \to l\nu\nu\nu$	177975	379999	1.47	258	Full
$ZZ \to ll\nu\nu$	177999	769799	.519	1483	Full
$ZW \to eeqq$	183585	176000	1.54	114	Full
$ZZ \to eeqq$	183586	30000	0.247	122	Full
$ZW \to \mu\mu qq$	183587	176000	1.54	115	Full
$ZZ \to \mu\mu qq$	183588	30000	0.248	121	Full
$ZW \to \tau\tau qq$	183589	175999	1.52	115	Full
$ZZ \to \tau\tau qq$	183590	30000	0.242	124	Full
$ZW \to \nu\nu qq$	183591	180000	2.83	63.6	Full
$ZZ \to \nu\nu qq$	183592	120000	1.74	68.8	Full
$WW \to e\nu qq$	183734	789998	7.72	102	Full
$WZ \to e\nu qq$	183735	209999	2.00	105	Full
$WW \to e\nu qq$	183736	789898	7.74	102	Full
$WZ \to e\nu qq$	183737	209900	2.00	105	Full
$WW \to e\nu qq$	183738	789995	7.71	102	Full
$WZ \to e\nu qq$	183739	210000	2.01	104	Full

7.2.1.6 γ + jets production

γ+jets production can contribute to the background of this analysis when fake $E_{\mathrm{T}}^{\mathrm{miss}}$ is present along with real or fake b-jets. Due to the high cross section of γ+jet production, this is one of the most significant backgrounds, comparable in size to $t\bar{t}$. The samples used for γ+jet production are produced using Sherpa and the NLO PDF set CT10 and up to 4 partons in the matrix element. These samples also have massive bottom and charm quarks. The samples are summarized in Table 7.7.

Table 7.7: List of simulated γ+jet samples that are used for rough background evaluation in the analysis. All samples are generated using Sherpa.

Flavor	γ p_{T} range [GeV]	DSID	Number of events	σ [pb]	$\int \mathscr{L} dt$ [fb^{-1}]	Fast/FullSim
C Veto, B Veto	100-140	177574	1999998	215	9.29	Fast
C Veto, B Veto	140-280	177575	1999497	68.1	29.3	Fast
C Veto, B Veto	280-500	177576	749992	2.85	263	Full
C Veto, B Veto	500+	177577	199995	0.134	1490	Full
C Filter, B Veto	100-140	177578	1999995	182	11.0	Fast
C Filter, B Veto	140-280	177579	1999999	58.1	34.4	Fast
C Filter, B Veto	280-500	177580	749989	2.48	302	Full
C Filter, B Veto	500+	177581	199992	0.121	1660	Full
B Filter	100-140	177582	1999999	32.5	61.5	Fast
B Filter	140-280	177583	1999999	11.6	173	Fast
B Filter	280-500	177584	249996	0.589	424	Full
B Filter	500+	177585	99999	0.0320	3150	Full

7.2.1.7 Multijet QCD production

Multijet QCD production can also be a background when a jet fakes a photon, there is fake $E_{\mathrm{T}}^{\mathrm{miss}}$, and real or fake b-jets are present. This is extremely rare, but multijet QCD has a high cross section so it could still fake the signal. Pythia samples were checked to look at this background, but were not used for any plots or calculations. This

was because the events that passed the cuts seemed to be true photons rather than fake, which are modeled in other samples. Furthermore, the samples have low luminosity until the p_{T} of the sample is rather high. The samples checked are summarized in Table 7.8.

Table 7.8: List of simulated multijet QCD samples that were looked at for the analysis. The lowest p_{T} (and thus highest σ) samples are listed first. All samples are generated using PYTHIA.

Process	DSID	Number of events	σ [pb]	$\int \mathscr{L} dt$ [fb^{-1}]	Fast/FullSim
Dijet J2	147912	5999034	105000	.0570	Full
Dijet J3	147913	5997214	663	9.04	Full
Dijet J4	147914	5977254	4.56	1310	Full
Dijet J5	147915	2996082	.0855	35000	Full
Dijet J6	147916	2993651	.00195	1540000	Full
Dijet J7	147917	2991955	0.000593	5040000	Full

7.2.2 Signal Simulation

This analysis is motivated by the higgsino-like neutralino decay signatures predicted by General Gauge Mediation (GGM) models, namely a final-state signature that consists of a photon, pair of b-quarks, and high $E_{\mathrm{T}}^{\mathrm{miss}}$. A grid of GGM signal points is simulated with a specific set of benchmark parameter values. The sensitivity of the analysis is evaluated using this grid of points.

In this particular region of the GGM model space, the lightest neutralino mass eigenstate is a mixture of bino and higgsino flavor eigenstates. The neutral wino is much heavier so it does not contribute to the flavor of the lightest neutralino. Due to the Weinberg mixing angle in the Standard Model, the bino component of the lightest neutralino couples to both the photon and the Z. In the 2D grid, the two free parameters are the gluino and neutralino masses ($m_{\tilde{g}}$,$m_{\tilde{\chi}_1^0}$). Other parameters are fixed to $M_2 =$

2.5 TeV, tanβ = 1.5, and NLSP cτ < 0.25 mm. The GGM model parameters M_1 and μ determine the lightest neutralino mass, and the values of these two parameters are varied in such a way that the branching ratios of the $\tilde{\chi}_1^0$ are approximately constant, resulting in Br($\tilde{\chi}_1^0 \rightarrow h + \tilde{G}$) $\approx$ 56%, Br($\tilde{\chi}_1^0 \rightarrow \gamma + \tilde{G}$) $\approx$ 33%, and Br($\tilde{\chi}_1^0 \rightarrow Z + \tilde{G}$) $\approx$ 11%, numbers which vary by $\pm$ 2% throughout the grids [48]. The value of μ must also be negative in order to make the branching ratio to the Higgs boson greater than the branching ratio to Z. The values of M_1 and μ used to generate each mass point are shown in Table 7.9. Masses of sleptons and squarks are set to 2.5 TeV. The Higgs boson is in the decoupling regime with M_A = 2 TeV and M_h = 126 GeV. The branching fraction $h \rightarrow b\bar{b}$ for this choice of M_h is $\approx$ 60%.

Table 7.9: The values of M_1 and μ used to generate the 2D grid.

μ [GeV]	M_1 [GeV]	$M_{\tilde{\chi}_1^0}$ [GeV]
-150	275	149.3
-175	230	173.7
-200	234	198.0
-250	270	247.1
-350	362.5	346.0
-450	460.5	445.5
-550	559.5	545.2
-650	659	645.0
-750	758.5	744.8
-850	858.5	844.8
-950	958.5	944.7
-1050	1058.5	1044.7
-1150	1158	1144.5
-1250	1258	1244.5
-1350	1358	1344.5
-1450	1458	1444.4

The full mass spectrum and decay widths, including the Higgs branching frac-

tions, are calculated using this set of parameters with SUSPECT 2.41 [49], SDECAY 1.3b [50], and HDECAY 3.4 [51] as part of the SUSYHIT package 1.3 [52]. Events are generated with HERWIG++ [53]. Events are then simulated using the ATLFAST-II fast simulation. In total, 103 signal points were produced. The ($m_{\tilde{g}}$,$m_{\tilde{\chi}_1^0}$) grid contains 87 signal points. These grid points contain only gluino (strong) production. Additionally, there are 16 points that contain only gaugino (weak) production for the different neutralino masses represented in the grid. These samples contain production by all different combinations of neutralinos and charginos, and are typically not dominated by any one process. For each point in the grid, the dataset containing strongly produced gluinos is combined with the corresponding dataset containing weakly produced gauginos to give a full representation. The samples were separated out of convenience, as the gluino production cross sections are independent of the neutralino mass and weak production cross sections are independent of the gluino mass. In addition, it makes event reweighting easier, as strongly and weakly produced events typically have dramatically different K-factors. Lastly, in regions where weak production dominates, it is more efficient to have one large weak production dataset per neutralino mass than reproducing practically the same events several times with datasets that contain both strong and weak production.

In the ($m_{\tilde{g}}$,$m_{\tilde{\chi}_1^0}$) grid, the gluino mass ranges from 700 GeV to 1.5 TeV in 100 GeV intervals, and the neutralino mass ranges from 150 GeV to 50 GeV less than the relevant gluino mass in 100 GeV intervals, though the 175 GeV and 200 GeV neutralino mass points are included as well. In some regions of the grid the production of signal

events proceeds dominantly through strong interaction that produces gluinos, while in others, the electroweak interaction leads to the production of gauginos. The strong and weak production cross sections are shown in Figure 7.6. The total cross section and the fraction of events that are produced through the electroweak interaction are shown in Figure 7.7.

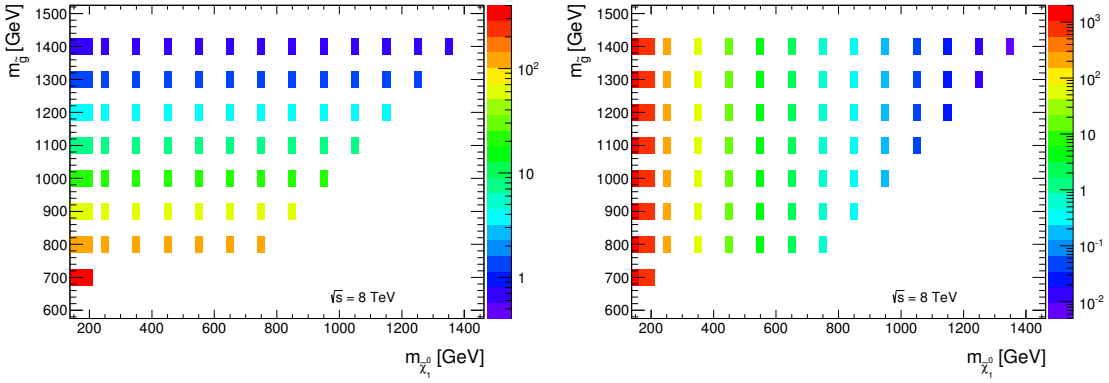

Figure 7.6: The strong production cross section [fb] (left) and the weak production cross section [fb] (right) in the gluino grid.

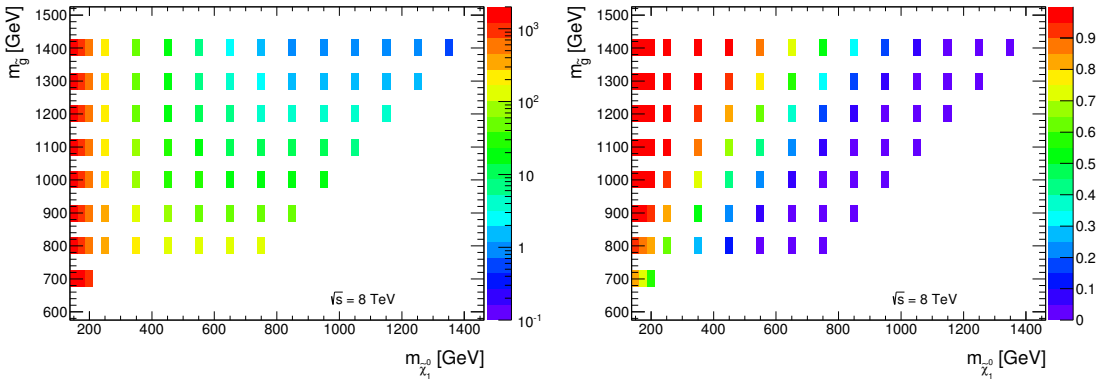

Figure 7.7: The total cross section [fb] (left) and the fraction of events that are produced through the electro-weak interaction (right) in the gluino grid.

The production datasets generated with HERWIG++ have names of the form `mc12_8TeV.175057.Herwigpp_UEEE3CTEQ6L1_GGM_gl_neut_700_150`, and the two respec-

tive mass scales are given in GeV. The weak production dataset names are of the form `mc12_8TeV.175144.Herwigpp_UEEE3CTEQ6L1_GGM_neut_150`. Dataset IDs range from 175057 to 175143 for the gluino grid, and from 175144 to 175159 for weak production. This analysis used derived datasets in the SUSY_NTUP format with configuration tags `e1635_a159_a171_r3549_p1328`.

The production cross sections for the generated signal datasets are calculated using the NLL-Fast and Prospino programs. The NLL-Fast program computes gluino hadroproduction cross sections up to the next-to-leading-log terms [54], while Prospino [55] is used here to compute next-to-leading-order cross sections for all weak production. For each point in the production grids, NLL-Fast is used to calculate the cross section of the $\tilde{g}\tilde{g}$, $\tilde{q}\tilde{g}$, and $\tilde{q}\tilde{q}$ processes, and Prospino is used to calculate the electroweak $\tilde{\chi}\tilde{\chi}$ processes. The central value of the cross section for each individual process is defined according to the ATLAS SUSY group and PDF4LHC recommendations [56], taking into account the envelope of cross sections calculated for different PDF sets. The total cross section is the sum of the individual process cross sections, with the uncertainties added in quadrature.

The NLO+NLL strong production cross sections for the signal points in the $m_{\tilde{g}}$ vs. $m_{\tilde{\chi}_1^0}$ grid are tabulated in Table 7.10. The NLO gaugino pair production cross sections are given in Table 7.11. These two decoupled production mechanisms can be combined to find the total signal production cross section for any point in the benchmark plane.

Table 7.10: The total LO and NLO+NLL strong production cross sections with relative uncertainties and derived K factors for points in the GGM gluino-neutralino signal grid. The LO cross sections are calculated using CTEQ, whereas the NLO+NLL cross sections are calculated using NLL-fast and both MSTW and CTEQ NLO PDFs.

$M_{\tilde{g}}$ [GeV]	σ(LO) [fb]	σ(NLO+NLL) [fb]	Uncertainty (%)	K factor
700	188.6	434.0	18.7	2.249
800	65.5	157.2	20.28	2.336
900	24.52	60.18	22.87	2.398
1000	9.7	24.32	25.85	2.464
1100	3.956	10.16	28.55	2.528
1200	1.663	4.396	31.95	2.616
1300	0.7084	1.942	35.48	2.724
1400	0.3044	0.8705	39.04	2.845
1500	0.1320	0.3943	42.95	2.987

Table 7.11: The LO and NLO gaugino pair production cross sections with relative uncertainties and derived K factors for GGM gluino-neutralino signal points. The LO cross section could not be calculated for the highest-mass neutralino points.

$m_{\tilde{\chi}_1^0}$[GeV]	σ(LO) [fb]	σ(NLO) [fb]	Uncertainty (%)	K factor
150	1365	1774	2.768	1.299
175	762.9	985.8	2.687	1.292
200	458.2	587.9	2.66	1.283
250	188.9	239.4	2.657	1.267
350	44.79	55.53	3.003	1.24
450	13.63	16.52	3.158	1.212
550	4.773	5.662	3.367	1.186
650	1.822	2.112	3.543	1.159
750	0.7374	0.837	3.688	1.135
850	0.3099	0.3437	3.814	1.109
950	NA	0.1461	4.261	NA
1050	NA	.06284	5.187	NA
1150	NA	.02747	6.368	NA
1250	NA	.01207	7.971	NA
1350	NA	.005306	10.07	NA

Chapter 8

Object Selection

Jets, b-tagged jets, photons, leptons and the missing transverse momentum are defined by the standard ATLAS procedure as outlined in the following sections.

8.1 Jets

Jets are reconstructed from calibrated clustered energy deposits using the anti-kt jet clustering algorithm [57] with distance parameter $\Delta R = \sqrt{\Delta\phi^2 + \Delta\eta^2} = 0.4$. The inputs to this algorithm are clusters [58] of calorimeter cells seeded by cells with energy significantly above the measured noise. Jet momenta are constructed by performing a four-vector sum over these topological clusters of calorimeter cells, treating each as an $(E, \vec{p})$ four-vector with zero mass. The jet energies are corrected for the effects of calorimeter non-compensation and inhomogeneities by using p_{T}- and η-dependent calibration factors based on Monte Carlo (MC) simulations validated with extensive test-beam and collision-data studies [59]. The jet energy is first corrected using the scale established for electromagnetic objects (EM scale) and then further corrected to the hadronic energy scale. Only jet candidates with $p_{\mathrm{T}} > 20$ GeV and $|\eta| < 2.8$ are

used in this analysis. Due to pileup, events can have many collision vertices, with one (the primary vertex) typically producing all of the high energy objects. However, other collision vertices often produce some low energy jets. In order to remove jets which originate from pile up, jets are associated with vertices by matching jets with tracks, which are then matched with vertices. The fraction of p_{T} associated with the primary vertex is called the jet vertex fraction (jvf). It is required that $jvf > 0.5$ for jets with $p_{\mathrm{T}} < 50$ GeV to eliminate most of the jets resulting from pileup. Jets with no tracks are assigned a jvf value of -1, and thus would fail this cut if they have $p_{\mathrm{T}} < 50$ GeV. Some jets arise due to calorimeter noise or cosmic ray energy deposits. Such fake jets display different properties than jets arising from parton fragmentation. A selection of cleaning cuts is applied to each jet in the event with $p_{\mathrm{T}}^{\mathrm{LCTopo}} > 20$ GeV. The event is rejected if a jet has properties consistent with the following non-collision sources:

- If the fraction of energy in the hadronic endcap calorimeter is larger than 0.5 ($HECf > 0.5$), the measured absolute value of quality of the jet is greater than 0.5 ($|HECQ| > 0.5$), and the normalized jet quality computed as the energy squared cells mean quality is larger than 0.8 ($LArQmean > 0.8$). For more details, see Ref. [60].

- If the absolute value of the total energy in cells with a negative value is greater than 60 GeV the jet is considered bad($|neg.E| > 60$ GeV). For this and the previous item, the signal is consistent with noise in the hadronic endcap calorimeters.

- For jets with $|\eta| < 2.8$, if the electromagnetic energy fraction is larger than 0.95

($EMf > 0.95$), the absolute jet quality value is greater than 0.8 ($|LArQ| > 0.8$), and the normalized jet quality is larger than 0.8 ($LArQmean > 0.8$).

- For jets with $|\eta| < 2$, if the electromagnetic energy fraction is less than 0.05 ($EMf < 0.05$) and the ratio of the sum p_{T} of the tracks associated to the jets divided by the calibrated jet p_T is less than 0.05 ($chf < 0.05$). In the case where the jet has $|\eta| > 2$ the jet is considered bad if the electromagnetic energy fraction is less than 0.05 with no requirement on the jet charge fraction.

8.2 *b*-tagging

Jets are identified as containing a *b*-quark, and thus called "*b*-tagged," using the MV1 b-tagging algorithm. The MV1 *b*-tagging algorithm is based on a neural network using the output weights of the JetFitter+IP3D, IP3D and SV1 algorithms [61] as input. Only jets with $p_{\mathrm{T}} > 20$ GeV and $|\eta| < 2.5$ are considered, and the working point corresponds to *b*-tagging efficiency of 70%. The light jet rejection for this operating point is about 137 [61].

8.3 Photons

For baseline photons, the transverse energy is required to be greater than 20 GeV, and photons must fulfill a set of tight identification requirements as follows. We require the electromagnetic cluster to be consistent with that expected of a photon. Cuts are applied on the fractional energy deposit in the hadronic calorimeter and on the shower width in η and ϕ in the first and second layers of the electromagnetic calorimeters

[62]. Furthermore, the very fine segmentation in η in the first layer of the electromagnetic calorimeters is used to discriminate against π^0 mesons by cutting out clusters that show two resolved peaks.

Since photons can convert into e^+e^- pairs by interacting with the material in front of the calorimeter, there are two categories of photons: unconverted and converted. Photons are classified as unconverted photons if they do not have tracks from a conversion vertex matched to the cluster, and as converted if they do. A two-track conversion vertex is formed when two tracks passing a TRT high-threshold requirement form a vertex consistent with coming from a massless particle. A single-track conversion is formed when a track that passes a TRT high-threshold requirement has a first hit after the pixel b-layer. The photon is accepted if the $|\eta|$ of its cluster is smaller than 2.37 and not in the transition region between barrel and end-cap calorimeters ($1.37 < |\eta| < 1.52$). An isolation criteria is applied in order to suppress the background from photons originated inside jets: the total energy deposited inside the $\Delta R = 0.2$ cone is required to be smaller than 5 GeV. Another reason for this requirement is that the identification efficiency of photons drops significantly for true photons close to jets.

Cleaning cuts are applied on photon candidates in order to identify bad quality or fake clusters coming from instrumental problems. We also apply an event cleaning based on the photons. A bad photon is defined as either having a cluster time $|t| > (10 + 2/|E_{\text{clus}}|)$ ns, where E_{clus} is measured in GeV for the energy correction to the cluster time, or if the value $\frac{\Sigma_{\text{cluster}} E_{\text{cell}}(Q > 4000)}{\Sigma_{\text{cluster}} E_{\text{cell}}} > 0.8\%$

and either the isEM variables $R_\phi > 1.0$ or $R_\eta > 0.98$, as defined in Ref. [63]. The cell Q-factor measures the difference between the measured pulse shape and the predicted pulse shape that is used to reconstruct the cell energy.

8.4 Leptons

Electron candidates are clustered energy deposits in the electromagnetic calorimeter matched to a track. They are required to have $p_{\mathrm{T}} > 25$ GeV and $|\eta| < 2.47$, and to satisfy the medium++ electron shower shape and track selection criteria described in [64]. Candidates in the calorimeter transition region $1.37 < |\eta| < 1.52$ are excluded.

Muons are reconstructed with the STACO algorithm using tracks in the inner detector and in the muon spectrometer [65]. Muon candidates are required to have $p_{\mathrm{T}} > 25$ GeV and $|\eta| < 2.4$, pass loose quality cuts, and also pass inner detector track quality requirements [65, 66].

8.5 Missing transverse momentum

The measurement of the missing transverse momentum two-vector $\vec{p_{\mathrm{T}}}^{\mathrm{miss}}$ and its magnitude (conventionally denoted $E_{\mathrm{T}}^{\mathrm{miss}}$) is done using the RefFinal algorithm. It is based on the vector sum of the p_{T} of reconstructed objects in the event. Objects include muons (electrons) with p_{T} above 10 GeV, tight photons with p_{T} above 20 GeV, jets with $\mathrm{E_T} > 20$ GeV, and calibrated calorimeter clusters which are not associated with any object (also called '$E_{\mathrm{T}}^{\mathrm{miss}}$ soft terms') with $|\eta| < 4.9$ as described in [67]. The METUtility package is used to recalculate the $E_{\mathrm{T}}^{\mathrm{miss}}$ using selected objects.

8.6 Total Transverse Energy

For the regions of GGM phase space that are being studied in this analysis, the total visible transverse energy is expected to be large. The energy in these events is expected to be much larger than the typical SM background event. To represent this quantity, the observable H_{T} is defined as the scalar sum of the transverse energy of all individual visible objects (including jets, photons, electrons, and muons) defined in this section:

$$H_{\mathrm{T}} \equiv \sum_{i=1}^{N_{\mathrm{obj}}} (p_{\mathrm{T}})_i \tag{8.1}$$

8.7 Overlap removal

After the objects have been identified in the steps above, the following standard SUSY group recommendations for overlap removal are applied. Any jet candidate lying within a distance of $\Delta R < 0.2$ from an electron or photon is discarded. Also, in order to ensure that selected leptons and photons are not originating as the result of hadronic activity in the event, electrons and photons within a $0.2 < \Delta R < 0.4$ distance from a jet are rejected. Muons within a $\Delta R < 0.4$ distance from a jet are discarded as well. Since a major background in this analysis is due to electrons faking a photon, a preliminary suppression of that background is achieved by picking the electron interpretation whenever an electron/photon ambiguity exists, so the photon candidate is discarded if it lies within a $\Delta R < 0.01$ distance from an electron. Converted photons are able to survive this cut because medium++ electrons require a b-layer hit that most

converted photons do not have, since they convert after passing through the b-layer. All of these overlap criteria are applied prior to the isolation requirements of photons, electrons, and muons, but after all other requirements.

Chapter 9

Event Selection and Optimization

In order to improve upon the limit set with 7 TeV data shown previously in Figure 4.2, there are two distinct regions in which the limit can be improved. Both regions have a high p_{T} photon, b-jets, and $E_{\mathrm{T}}^{\mathrm{miss}}$, but the overall energy scale and the number of other objects in events are quite different. Therefore, a single signal region such as what was used for the 7 TeV analysis is not optimal, and two signal regions are defined.

9.1 Signal region definitions

The first event selection is aimed at detecting weakly produced, light neutralinos (< 250 GeV) with a high cross section. These events are characterized by relatively low energy objects with very little jet activity in addition to the expected objects. Events in this signal region (SRL) are required to pass the following cuts:

1. At least 5 tracks must be assigned to the primary vertex;

2. The event should contain a tight photon with p_{T} in excess of 125 GeV inside the $|\eta| < 2.37$ range;

3. The event should contain between two and four (inclusive) jets with $p_{\mathrm{T}} > 20$ GeV;

4. At least two jets should be b-tagged;

5. The event should have no identified charged lepton (e or μ). This cut greatly reduces $t\bar{t}$ or Wbb events with leptonic W decays, which are major backgrounds for this signature;

6. The $E_{\mathrm{T}}^{\mathrm{miss}}$ of the event should be greater than 100 GeV;

7. The $M_{\mathrm{T}}^{\gamma,E_{\mathrm{T}}^{\mathrm{miss}}}$ is required to be greater than 90 GeV. This cut is very efficient in removing events in which an electron or τ from a W decay is faking a photon;

8. The $E_{\mathrm{T}}^{\mathrm{miss}}$ should be isolated; namely, its minimal angle with respect to one of the two leading jets should obey $\Delta\phi_{\mathrm{min}}(E_{\mathrm{T}}^{\mathrm{miss}},\ \mathrm{jet}) >\ 0.3$. This cut suppresses QCD events in which the missing energy is mostly instrumental;

9. The reconstructed mass of the two b-jets with highest flavor weight should be between 75 and 150 GeV.

After applying these cuts one is left with a total SM background of 17.4 ± 1.0 events in the simulations as shown in Table 9.1. This is a Monte Carlo based preliminary number (errors quoted are due to limited MC statistics only) and it is not actually used in the background estimation. For reference, a signal sample with $m_{\tilde{g}} = 1200$ GeV and $m_{\tilde{\chi}_1^0} = 150$ GeV is shown. It contains both gluino and gaugino production, but is dominated by gaugino production.

Table 9.1: Low mass signal region cut-flow of simulated events normalized to 20.34 fb^{-1}. Uncertainties are due to limited MC statistics only.

Cut	Total MC	γ+jets	$t\bar{t}$ (+γ)	$W + \gamma$/jets	$Z(\rightarrow \nu\nu)$+ γ/jets	Single Top	$m_{\tilde{g}} = 1200$ GeV, $m_{\tilde{\chi}_1^0} = 150$ GeV
No cuts	9.65E+8	1.17E+7	2.80E+6	8.07E+8	1.41E+8	1.07E+6	3.61E+4
Event cleaning, $p_{\mathrm{T}}^{\gamma} > 25$ GeV	7.65E+6	7.57E+6	7.50E+3	6.23E+4	6.02E+3	1.33E+3	1.39E+4
$p_{\mathrm{T}}^{\gamma} > 125$ GeV	3341500 ± 2300	3322400 ± 2300	1637.4 ± 7.0	14704 ± 72	2256.5 ± 8.9	308.1 ± 2.6	2681 ± 53
$2 \leq N_{\mathrm{jets}} \leq 4$	2147200 ± 1800	2137000 ± 1800	943.1 ± 5.3	8113 ± 38	723.1 ± 6.3	217.4 ± 2.2	1518 ± 40
One b-tagged jet	212580 ± 470	210580 ± 470	734.4 ± 4.6	1011 ± 10	86.0 ± 1.3	151.1 ± 1.8	539 ± 24
Two b-tagged jet	18840 ± 100	18460 ± 100	264.8 ± 2.7	73.3 ± 2.3	5.67 ± 0.23	33.38 ± 0.90	194 ± 14
Lepton Veto	18700 ± 100	18450 ± 100	159.7 ± 2.2	53.4 ± 2.1	5.67 ± 0.23	21.47 ± 0.81	194 ± 14
$E_{\mathrm{T}}^{\mathrm{miss}} > 100$ GeV	149.3 ± 4.8	86.4 ± 4.6	43.6 ± 1.1	10.33 ± 0.71	2.92 ± 0.14	5.37 ± 0.40	38.2 ± 6.1
$M_{\mathrm{T}} > 90$ GeV	116.3 ± 4.1	71.7 ± 3.9	31.76 ± 0.91	6.81 ± 0.57	2.76 ± 0.14	3.18 ± 0.23	31.2 ± 5.5
$\Delta\phi_{\mathrm{min}}(E_{\mathrm{T}}^{\mathrm{miss}}, \mathrm{j}_{1,2}) > 0.3$	53.4 ± 2.2	16.1 ± 2.0	26.41 ± 0.82	5.87 ± 0.53	2.34 ± 0.10	2.67 ± 0.21	24.8 ± 4.9
75 GeV $< M_{b\bar{b}} <$ 150 GeV	17.4 ± 1.0	3.88 ± 0.87	9.80 ± 0.49	1.82 ± 0.29	0.76 ± 0.06	1.14 ± 0.15	21.2 ± 4.4

The second signal region is aimed at detecting events in which gluinos are produced, eventually decaying to moderate to high-mass neutralinos, with small cross section. These events are characterized by relatively high energy objects with additional jet activity along with the expected objects. Events in this signal region (SRH) are required to pass the following cuts:

1. At least 5 tracks must be assigned to the primary vertex;
2. The event should contain a tight photon with p_{T} in excess of 150 GeV inside the $|\eta| < 2.37$ range;
3. The event should contain at least 4 jets with $p_{\mathrm{T}} > 20$ GeV;
4. At least one jet should be b-tagged;
5. The $E_{\mathrm{T}}^{\mathrm{miss}}$ of the event should be greater than 200 GeV.
6. The $M_{\mathrm{T}}^{\gamma,E_{\mathrm{T}}^{\mathrm{miss}}}$ is required to be greater than 90 GeV. This cut is very efficient in removing events in which an electron or τ from a W decay is faking a photon;
7. The $E_{\mathrm{T}}^{\mathrm{miss}}$ should be isolated; namely, its minimal angle with respect to one of the four leading jets should obey $\Delta\phi_{\mathrm{min}}(E_{\mathrm{T}}^{\mathrm{miss}}, \text{ jet}) > 0.3$. This cut suppresses QCD events in which the missing energy is mostly instrumental;
8. The H_{T} of the event is required to be greater than 1000 GeV.

After applying these cuts one is left with a total SM background of 4.49 ± 0.56 events in the simulations as shown in Table 9.2. This is a Monte Carlo based

preliminary number (error is due to limited MC statistics only) and it is not actually used in the background estimation. For reference, a signal sample with $m_{\tilde{g}} = 1200$ GeV and $m_{\tilde{\chi}_1^0} = 850$ GeV is shown. It contains both gluino and gaugino production, but is dominated by gluino production. The cuts used for the two signal regions are summarized in Table 9.3.

Table 9.2: High mass signal region cut-flow of simulated events normalized to 20.34 fb^{-1}. Uncertainties are due to limited MC statistics only.

Cut	Total MC	γ+jets	$t\bar{t}$ (+γ)	$W+\gamma$/jets	$Z(\to \nu\nu)$+γ/jets	Single Top	$m_{\tilde{g}} = 1200$ GeV, $m_{\tilde{\chi}_1^0} = 850$ GeV
No cuts	9.65E+8	1.17E+7	2.80E+6	8.07E+8	1.41E+8	1.07E+6	7.99E+1
Event cleaning, $p_{\mathrm{T}}^{\gamma} > 25$ GeV	7.65E+6	7.57E+6	7.50E+3	6.23E+4	6.02E+3	1.33E+3	3.39E+1
$p_{\mathrm{T}}^{\gamma} > 150$ GeV	1609700 ± 1200	1599900 ± 1200	861.3 ± 4.9	7348 ± 48	1283.0 ± 7.4	177.1 ± 1.7	32.09 ± 0.57
$N_{\mathrm{jets}} \geq 4$	285610 ± 480	283780 ± 480	585.5 ± 4.1	1052 ± 11	86.1 ± 3.0	77.9 ± 1.1	29.10 ± 0.57
One b-tagged jet	47810 ± 160	47000 ± 160	492.5 ± 3.7	229.7 ± 4.1	17.16 ± 0.30	61.10 ± 0.95	22.15 ± 0.49
$E_{\mathrm{T}}^{\mathrm{miss}} > 200$ GeV	59.9 ± 2.1	12.9 ± 1.7	25.20 ± 0.84	15.06 ± 0.84	3.44 ± 0.13	2.67 ± 0.19	19.43 ± 0.46
$M_{\mathrm{T}} > 90$ GeV	43.6 ± 1.6	9.8 ± 1.3	17.96 ± 0.65	10.60 ± 0.71	3.30 ± 0.12	1.74 ± 0.10	19.28 ± 0.46
$\Delta\phi_{\mathrm{min}}(E_{\mathrm{T}}^{\mathrm{miss}}, \mathrm{j}_{1\ldots4}) > 0.3$	23.22 ± 0.91	0.70 ± 0.43	11.72 ± 0.54	7.04 ± 0.58	2.59 ± 0.11	1.01 ± 0.08	14.75 ± 0.40
$H_{\mathrm{T}} > 1000$ GeV	4.49 ± 0.56	0.65 ± 0.42	1.42 ± 0.20	1.94 ± 0.30	0.29 ± 0.04	0.19 ± 0.03	12.58 ± 0.37

Table 9.3: Cuts used for the two signal regions SRL and SRH.

Cut	SRL	SRH
p_{T}^{γ} [GeV]	> 125	> 150
N_{jets}	$\geq 2, \leq 4$	≥ 4
$N_{b-\mathrm{jets}}$	≥ 2	≥ 1
N_{leps}	0	—
$E_{\mathrm{T}}^{\mathrm{miss}}$ [GeV]	> 100	> 200
$M_{\mathrm{T}}^{\gamma, E_{\mathrm{T}}^{\mathrm{miss}}}$ [GeV]	> 90	> 90
$\Delta\phi_{\mathrm{min}}(E_{\mathrm{T}}^{\mathrm{miss}},\ \mathrm{N}_{\mathrm{leading\ jets}})$, N	> 0.3, 2	> 0.3, 4
H_{T} [GeV]	—	> 1000
$M_{b\bar{b}}$ [GeV]	$> 75, < 150$	—

9.2 Optimization

The optimization of the selection criteria is performed by calculating a discovery significance function using signal and background Monte Carlo samples. The plots in the sections that follow show the normalized distributions of representative signal samples and the major backgrounds in the upper portion. In the lower portions of the plots, the discovery significance of a signal + background hypothesis is shown with the cut value varied for the variable shown. The scale for the discovery significance is normalized to a maximum of 1 so that the effect on each signal sample can be observed. The signal samples used have $m_{\tilde{g}}$= 1200 GeV, and $m_{\tilde{\chi}_1^0}$= 150 or 450 GeV for the low mass region, or $m_{\tilde{\chi}_1^0}$= 450, 850, or 1150 GeV for the high mass region. Each signal sample has contributions from both gluino and gaugino production, with gaugino production being more prominent at low neutralino mass and less prominent at high neutralino mass. The background samples used are photon+jets, W+jets, and $t\bar{t}$. The selected cut value is shown with a solid line. The discovery significance function used is defined

in Eq. 9.1. This particular function does not depend on the uncertainty of the signal or background predictions, but is still useful as a guideline for the optimal cut values.

$$Z = \sqrt{2[(s+b)\ln(1+s/b) - s]} \tag{9.1}$$

9.2.1 Photon p_{T} cut

The p_{T} distribution of photons in $t\bar{t}$, photon+jets, $W+\gamma$/jets, and representative signal points ((1200 ,150) and (1200, 450) in the ($m_{\tilde{g}}$, $m_{\tilde{\chi}_1^0}$) plane for the low mass signal region and (1200, 450), (1200, 850) and (1200, 1150) in the ($m_{\tilde{g}}$, $m_{\tilde{\chi}_1^0}$) plane for the high mass signal region) is shown in Fig. 9.1. For the high mass region, the selected cut value is below the optimal value for the samples shown in order to preserve signal efficiency and for higher control region statistics. The values selected are 125 GeV for SRL and 150 GeV for SRH.

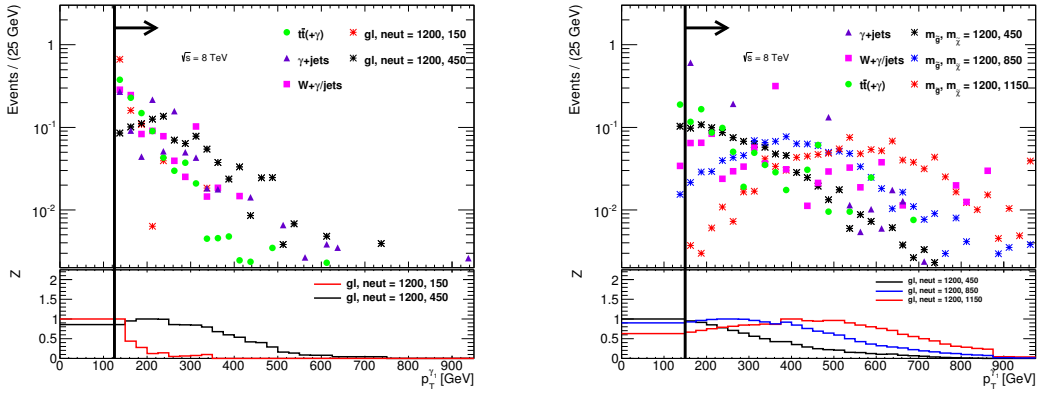

Figure 9.1: The p_{T}^{γ} distributions in the $t\bar{t}$ sample, photon+jet sample, $W+\gamma$/jets sample and simulated signal points after all other SRL cuts (left) and SRH cuts (right). The upper histograms are normalized to 1, while the lower histograms are normalized such that the maximum for each signal sample is 1. The bottom portion shows the discovery significance of observing the signal if a lower cut were made at that value for selected signal samples. The cut value chosen for the low mass region is 125 GeV and for the high mass region is 150 GeV.

9.2.2 Number of jets in the event

The distribution of the number of jets with $p_{\mathrm{T}} > 20$ GeV in the event after all other SRL and SRH cuts in the $t\bar{t}$ sample, photon+jet sample, $W + \gamma$/jets sample and simulated signal points is shown in Figs. 9.2 and 9.3. In the low mass region, the number of jets is required to be between 2 and 4 (inclusive), and in the high mass region, the number of jets is required to be at least 4. Because more jets are expected in the signal than the typical background, a maximum number of jets cut was not considered for SRH.

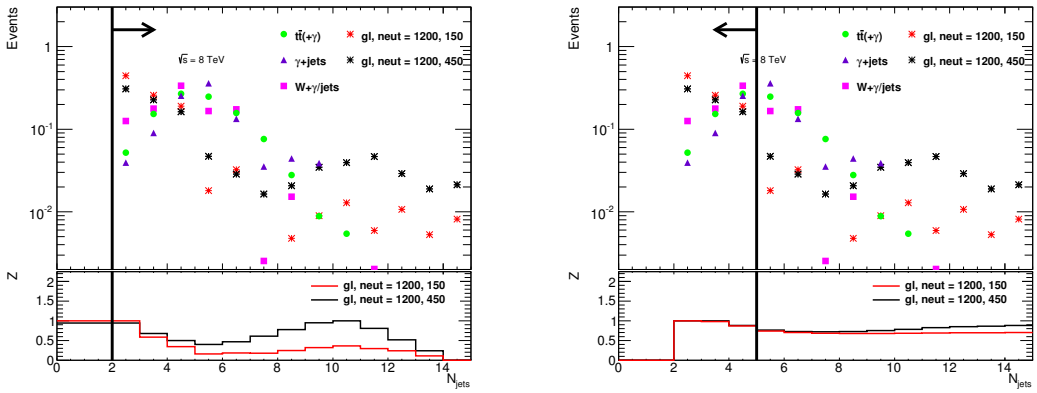

Figure 9.2: The distribution of the number of jets with $p_{\mathrm{T}} > 20$ GeV in the event after all other SRL cuts in the $t\bar{t}$ sample, photon+jet sample, $W + \gamma$/jets sample and simulated signal points. The left plot shows the effect of an $N_{\mathrm{jets}} \geq x$ cut, while the right plot shows the effect of an $N_{\mathrm{jets}} \leq x$ cut. Events are selected if the number of jets is between 2 and 4 (inclusive).

9.2.3 b-tag requirement

The requirement for b-tagged jets with 0.7 efficiency suppresses the W+jets and QCD background as seen in Tables 9.1 and 9.2. Requiring a single b-tagged jet for the high mass region results in a high efficiency for the signal while using 0.7 efficiency

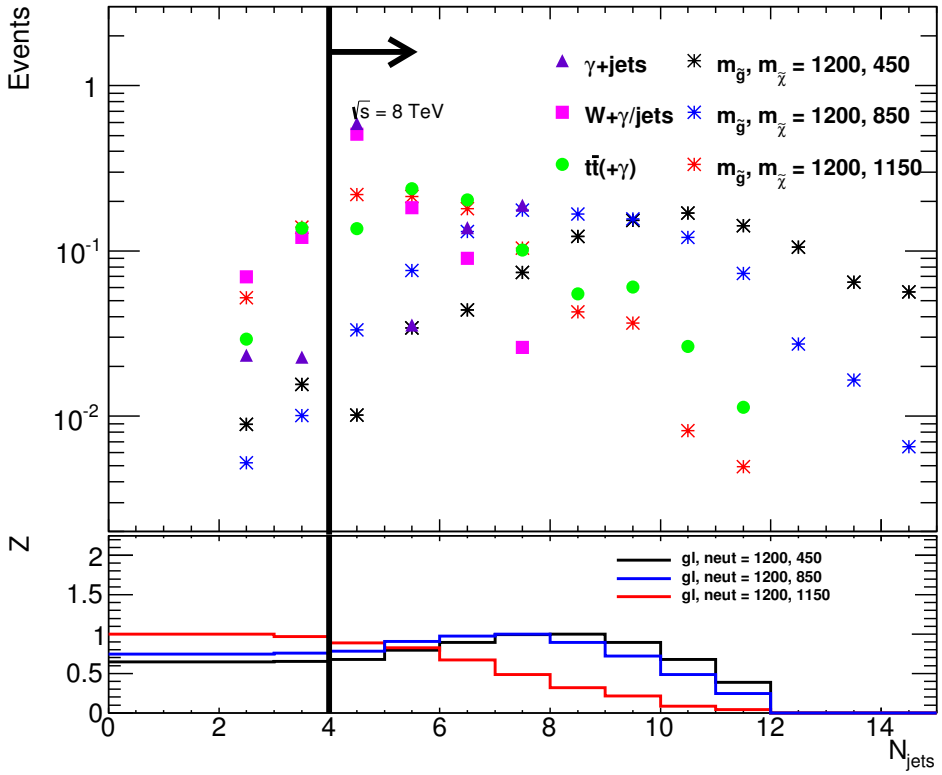

Figure 9.3: The distribution of the number of jets with $p_{\mathrm{T}} > 20$ GeV in the event after all other SRH cuts in the $t\bar{t}$ sample, photon+jet sample, $W + \gamma$/jets sample and simulated signal points. Events are selected if there are at least 4 jets.

ensures a high rejection against light jets. For the low mass region, a second b-tagged jet is required, further rejecting light jet background. The MV1 flavor weight for the most tagged jet is shown in Fig. 9.4, after the p_{T}^{γ} and N_{jets} cuts. The MV1 flavor weight for the second most tagged jet is shown in Fig. 9.5.

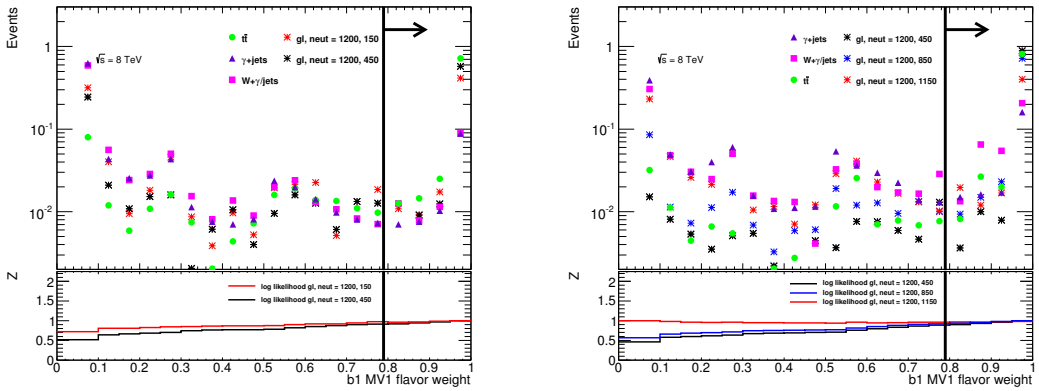

Figure 9.4: The distribution of the flavor weight of the most tagged jet after all SRL (left) and SRH (right) cuts, except neither has the $E_{\mathrm{T}}^{\mathrm{miss}}$ cut or additional b-tag cuts applied. For both analyses, the value must be greater than 0.7892. This corresponds to b-jets being tagged with approximately 70% efficiency. The upper histograms are normalized to 1, while the lower histograms are normalized such that the maximum for each signal sample is 1.

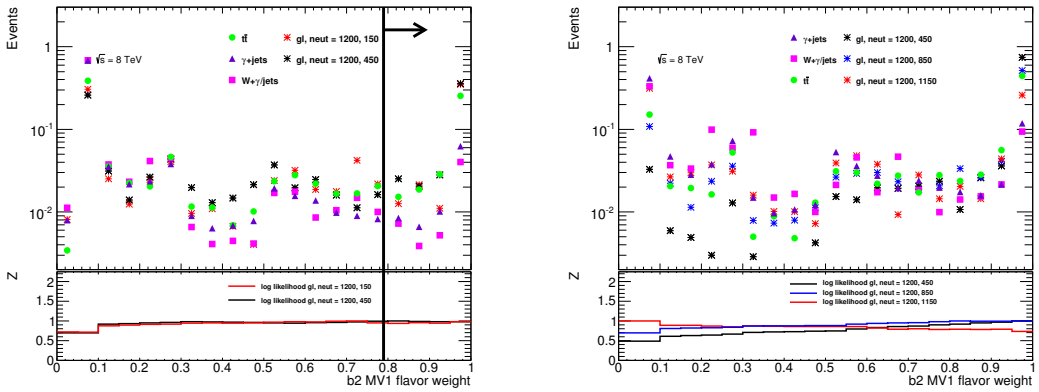

Figure 9.5: The distribution of the flavor weight of the second most tagged jet after all other SRL (left) and SRH (right) cuts, except neither has the $E_{\mathrm{T}}^{\mathrm{miss}}$ cut applied. For the low mass region, the value must be greater than 0.7892, while there is no requirement for the high mass region. The upper histograms are normalized to 1, while the lower histograms are normalized such that the maximum for each signal sample is 1.

9.2.4 Lepton veto

As already mentioned, demanding no identified lepton in the event removes dileptonic and semileptonic $t\bar{t}$ events with a prompt photon or with a photon faked by a jet and dileptonic events with a photon faked by an electron or a τ. There are no leptons expected from signal for either the high mass or low mass signal region. However, in the high mass signal region, leptons could be produced in the cascade depending on what the decay chain contains. For this reason, there is no lepton veto on the high mass signal region. The distribution of the number of leptons in the event after the p_{T}^{γ}, N_{jets}, and b-tag cuts in the $t\bar{t}$ sample, photon+jet sample, $W + \gamma$/jets sample and simulated signal points is shown in Fig. 9.6.

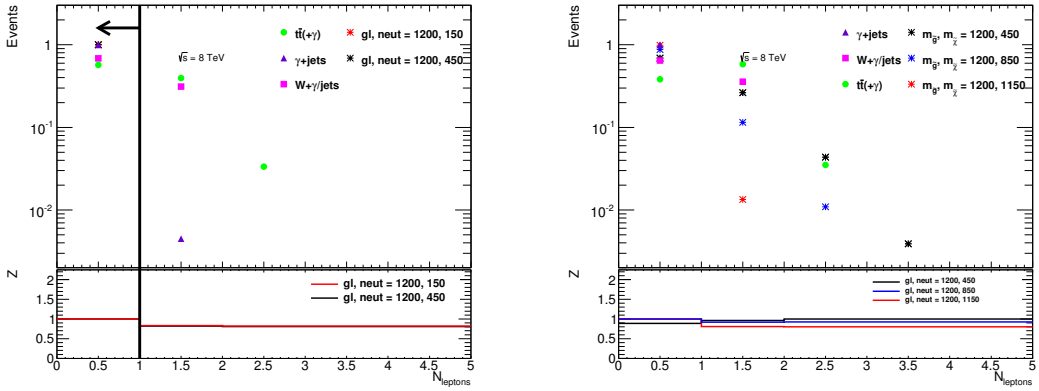

Figure 9.6: The distribution of the number of leptons in the event after all other SRL (left) and SRH (right) cuts in the $t\bar{t}$ sample, photon+jet sample, $W + \gamma$/jets sample and simulated signal points. The upper histograms are normalized to 1, while the lower histograms are normalized such that the maximum for each signal sample is 1. Leptons are vetoed in the low mass region and there is no lepton requirement for the high mass region.

9.2.5 $E_{\mathrm{T}}^{\mathrm{miss}}$ cut

The main characteristic of R-parity-conserving SUSY events, GGM included, is the presence of large $E_{\mathrm{T}}^{\mathrm{miss}}$. A cut on this quantity reduces the background contamination due to QCD as well as other processes in a dramatic way. The $E_{\mathrm{T}}^{\mathrm{miss}}$ distribution in the $t\bar{t}$ sample, photon+jet sample, $W + \gamma$/jets sample and simulated signal samples are shown in Fig. 9.7. As seen from the plots, the cut values cannot be simultaneously optimized for all points, so the cuts selected are on the conservative end to preserve signal efficiency and for higher control region statistics. The values selected are 100 GeV for SRL and 200 GeV for SRH.

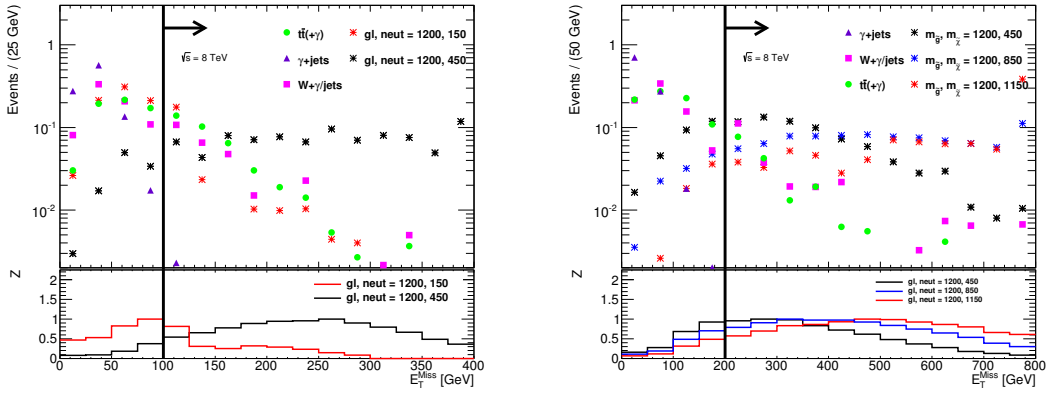

Figure 9.7: The $E_{\mathrm{T}}^{\mathrm{miss}}$ distributions in the $t\bar{t}$ sample, photon+jet sample, $W + \gamma$/jets sample and simulated signal points after all other SRL (left) and SRH (right) cuts. The upper histograms are normalized to 1, while the lower histograms are normalized such that the maximum for each signal sample is 1. The cut values chosen for the low mass region is 100 GeV and for the high mass region is 200 GeV.

9.2.6 $M_{\mathrm{T}}^{\gamma,E_{\mathrm{T}}^{\mathrm{miss}}}$ cut

The $E_{\mathrm{T}}^{\mathrm{miss}}$ direction is quasi-random with respect to the direction of jets and photons in the event. In SUSY events the high mass of the sparticles give rise to high

p_{T} particles, and therefore, the transverse mass of the photon and $E_{\mathrm{T}}^{\mathrm{miss}}$ for signal is usually large. On the other hand, when the photon is faked by one of the W decay products (e or τ) the same mass tends to be small. The M_{T} distribution in the $t\bar{t}$ sample, photon+jet sample, $W+\gamma$/jets sample and simulated signal points is shown in Fig. 9.8, after all cuts up to $E_{\mathrm{T}}^{\mathrm{miss}}$in the cut flow. As seen from the plot, by cutting at 90 GeV for each signal region, the first peak in the $t\bar{t}$ and $W+\gamma$/jets samples corresponding to the W transverse mass is removed by the cut.

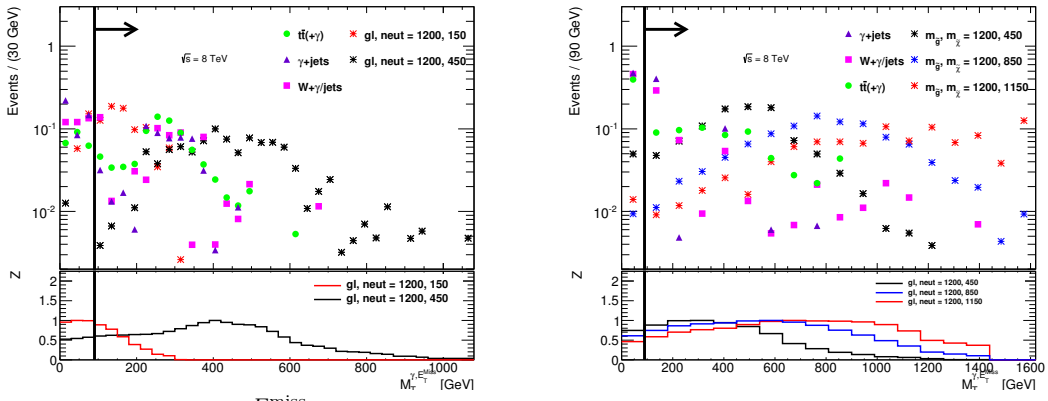

Figure 9.8: The $M_{\mathrm{T}}^{\gamma,E_{\mathrm{T}}^{\mathrm{miss}}}$ distribution after all other SRL (left) and SRH (right) cuts in the $t\bar{t}$ sample, photon+jet sample, $W+\gamma$/jets sample and simulated signal points. The upper histograms are normalized to 1, while the lower histograms are normalized such that the maximum for each signal sample is 1. The cut value chosen for both analyses is 90 GeV to reject electron faking photon background.

9.2.7 $E_{\mathrm{T}}^{\mathrm{miss}}$ isolation cut

$E_{\mathrm{T}}^{\mathrm{miss}}$ in signal events is due to the presence of two weakly-interacting LSP. The direction of $E_{\mathrm{T}}^{\mathrm{miss}}$ is, therefore, almost random and is usually not in the same direction as any other object in the final state. On the other hand, significant $E_{\mathrm{T}}^{\mathrm{miss}}$ may originate from instrumental origin or from the emission of energetic neutrino in b or c jets. In

such a case the direction of $E_{\mathrm{T}}^{\mathrm{miss}}$ is correlated with that of one of the jets. As seen from Tables 9.1 and 9.2, the $E_{\mathrm{T}}^{\mathrm{miss}}$ isolation > 0.3 cut reduces the QCD background by a factor of 4-5. For SRL, this variable is calculated with respect to the leading two jets, while for SRH, it is calculated with respect to the leading four jets. After all cuts in the cut flow up to $E_{\mathrm{T}}^{\mathrm{miss}}$, the $E_{\mathrm{T}}^{\mathrm{miss}}$ isolation distribution is shown in the $t\bar{t}$ sample, photon+jet sample, $W+\gamma$/jets sample and simulated signal points in Fig. 9.9. As seen from the plots, a large fraction of QCD events is removed by the cut.

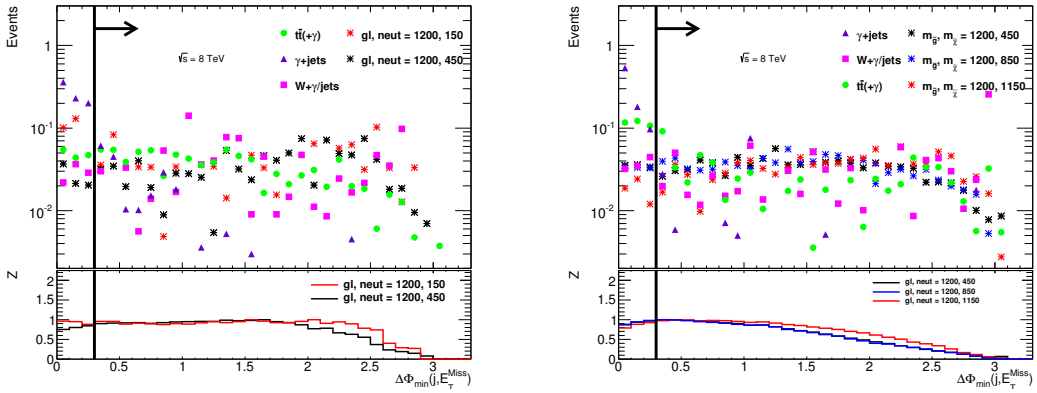

Figure 9.9: The $E_{\mathrm{T}}^{\mathrm{miss}}$ isolation distribution after all other SRL (left) and SRH (right) cuts in the $t\bar{t}$ sample, photon+jet sample, $W+\gamma$/jets sample and simulated signal points. The upper histograms are normalized to 1, while the lower histograms are normalized such that the maximum for each signal sample is 1. The cut value chosen is 0.3 for both signal regions in order to eliminate a majority of the γ+jet background.

9.2.8 $M_{b\bar{b}}$ cut

The b-jets in signal events are produced by the decay of a Higgs boson. Therefore, the reconstructed mass of the two b-tagged jets in the low mass region should be near the mass of the Higgs boson, which is set to 126 GeV in the signal samples. After the p_{T}^{γ}, N_{jets}, and b-tagging cuts, the $M_{b\bar{b}}$ distribution is shown in the $t\bar{t}$ sample, photon+jet sample, $W+\gamma$/jets sample and simulated signal points in Fig. 9.10. Events are

selected in SRL if $M_{b\bar{b}}$ is in the range of 75-150 GeV. Due to potential b-jets produced in the cascade decay that would affect the $M_{b\bar{b}}$ distribution, this cut is not used for the high mass region.

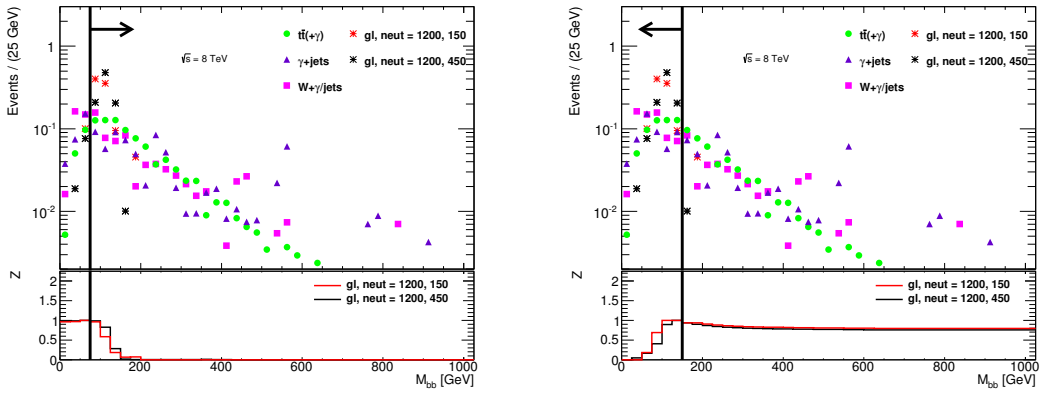

Figure 9.10: The $M_{b\bar{b}}$ distribution after all other SRL cuts in the $t\bar{t}$ sample, photon+jet sample, $W + \gamma$/jets sample and simulated signal points. The upper histograms are normalized to 1, while the lower histograms are normalized such that the maximum for each signal sample is 1. The left plot shows the effect of an $M_{b\bar{b}} > x$ cut, while the right plots shows the effect of an $M_{b\bar{b}} < x$ cut. The cut value chosen is 75 GeV $< M_{b\bar{b}} <$ 150 GeV.

9.2.9 H_{T} cut

In the high mass region, the gluinos produced lead to large amounts of energy in these events. The H_{T}, defined as the scalar sum of the p_{T} of all jets, photons, electrons, and muons, is generally much larger for these signal events than it is in background events. After the p_{T}^{γ} and N_{jets} cuts, the H_{T} distribution is shown in the $t\bar{t}$ sample, photon+jet sample, $W + \gamma$/jets sample and simulated signal points in Fig. 9.11. For SRH, the selected cut is 1000 GeV. Because the low mass region depends on gaugino production, there is less energy in events and this cut is not required.

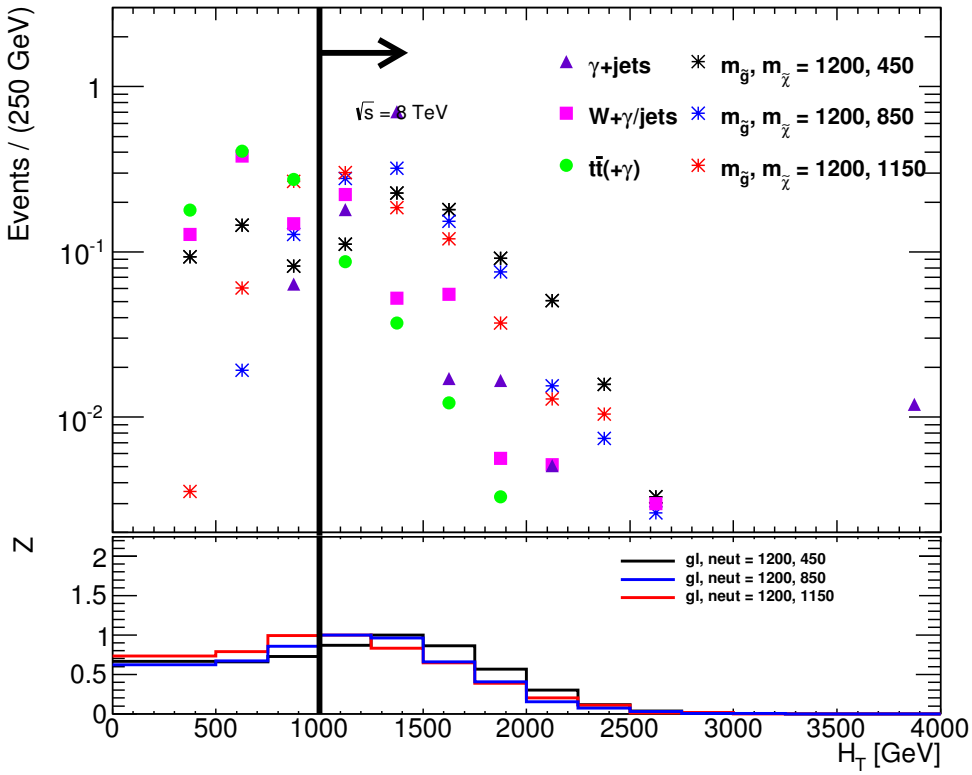

Figure 9.11: The H_{T} distribution after all other SRH cuts in the $t\bar{t}$ sample, photon+jet sample, $W + \gamma$/jets sample and simulated signal points. The upper histograms are normalized to 1, while the lower histograms are normalized such that the maximum for each signal sample is 1. The cut value chosen is 1000 GeV.

Chapter 10

The Background Model

10.1 Background Estimations

As shown in Tables 9.1 and 9.2 in Section 9.1, the dominant sources of background are $t\bar{t}$, $W + \gamma$/jets, and QCD processes. The others, like single top and diboson production processes, give rise to very low level of background. In Subsections 10.1.2 and 10.1.3, the data-driven methods of estimating the background containing $W \to l\nu$ processes are described (including $t\bar{t}$ sources). In Subsection 10.1.4 the QCD background is estimated, also in a data-driven way. Finally, Subsection 10.1.5 estimates the small contribution from irreducible $Z \to \nu\nu$ background using simulation samples.

10.1.1 General properties of $t\bar{t}$ and $W + \gamma$/jets background

Semileptonic $t\bar{t}$ events contain in their final state a pair of b-quarks and genuine $E_{\mathrm{T}}^{\mathrm{miss}}$. Leptonic W events contain genuine $E_{\mathrm{T}}^{\mathrm{miss}}$ and can be produced with b-quark pairs. These events may, therefore, survive the selection procedure provided a tight isolated high p_{T} photon candidate is also identified. Such a photon may originate from one of the following sources:

1. The electron from a leptonic decay of a W is misidentified as a photon;

2. The event includes a genuine prompt photon, whether radiated or from the underlying event;

3. One of the jets or a τ-lepton fakes a photon;

The electron misidentified as a photon background is discussed in Section 10.1.2 and is evaluated using a data-driven technique. For the purposes of background modeling, events with a prompt photon and events with a jet or τ misidentified as a photon will be grouped together. These two types are discussed in section 10.1.3 which makes use of a lepton control sample to estimate the background.

10.1.2 Processes containing $W \to l\nu$ in which an electron fakes a γ

A significant fraction of the background arising from $W \to l\nu$ processes is due to an electron that is misidentified as a photon. In order to calculate this contribution, two components are necessary: the fake rate scale factor, and a control region replacing the photon with an electron in the cut flow. The scale factor is then applied in the control region to calculate this background's contribution in the signal region. In addition, the contributions of misidentified electrons to several lepton control regions are calculated for use in the next section.

10.1.2.1 e$\to \gamma$ fake rate scale factor

The $e \to \gamma$ fake rate scale factor is estimated using a tag-and-probe method. In this case, the tag is defined to be an electron with $20\,\text{GeV} < p_\text{T} < 125\,\text{GeV}$ that

passes the tight++ identification criteria. In events with a tag electron, the probe can be either a photon or an electron with $p_{\mathrm{T}} > 125\,\mathrm{GeV}$ passing the object requirements discussed in Chapter 8. In order to reduce backgrounds from other processes, we also require $E_{\mathrm{T}}^{\mathrm{miss}} <$ 40 GeV. The invariant mass of the tag electron and probe photon or electron is reconstructed using the four-momenta of the two objects. This results in a clear Z-mass peak near 91 GeV, with varying sharpness depending on the sample. Since the Z boson cannot decay to an electron and a photon, we know that events of this type are most likely due to an electron being misidentified as a photon. Two MC samples are used to compare with the data result and are described in Table 10.1.

Table 10.1: List of simulated Z→ee samples that are used for calculating the $e \to \gamma$ fake rate. The MC results are for comparison purposes only and are not used in the analysis.

Process	Generator	DSID	Number of events	σ [pb]	$\int \mathscr{L} dt\ [fb^{-1}]$	Fast/FullSim
Z→ ee	SHERPA	147770	29993053	1240	24.2	Full
Z→ ee	POWHEG	147806	9994580	1110	9.00	Full

Figure 10.1 shows a comparison of the $e\gamma$ samples and the ee sample for data and Sherpa MC. In the Sherpa $Z \to ee$ MC sample, the shape of the two peaks is nearly identical; however, in the peaks seen in the data, the $e\gamma$ sample has much larger tails than the ee sample. In order to correct for this contamination, the Z peaks are fit to a Voigtian function (a convolution of a Gaussian distribution and a Breit-Wigner distribution), with the background modeled by a quadratic polynomial function using the Bernstein basis [68]. Bernstein polynomials have features that make them ideal for having well-behaved polynomial PDFs. The first feature is that the $n+1$ basis polynomials of degree n sum

to 1 for any value of x. The second feature is that the polynomials are non-negative in the defined range. Using standard polynomials, the fit sometimes fails to converge due to the background function going slightly negative in low background regions. Using a polynomial basis that is non-negative in the defined range alleviates this issue. This fit was done in the range $60\,\text{GeV} \leq M_{ee} \leq 120\,\text{GeV}$ (also done in 70-110 GeV range for systematics). Furthermore, in order to more accurately calculate the probability for any particular electron to be misidentified as photon, the fake rate is divided into three pseudorapidity bins. These bins are $|\eta| < 0.6$, $0.6 < |\eta| < 1.37$, and $1.52 < |\eta| < 2.37$. The fit for the central region $|\eta| < 0.6$ is shown in Figures 10.2 and 10.3. It is observed that there is very little background in each of the fits except for the data $e\gamma$ sample. The electron to photon fake rate scale factor is defined as:

$$f_{e\gamma} = \frac{N_{e\gamma}}{N_{ee}} \tag{10.1}$$

where $N_{e\gamma}$ (N_{ee}) is the number of electron-photon (electron-electron) pairs found under the fitted Z peak in the invariant mass distribution. A derivation of the above formula follows:

- Let the true number of $Z \to e^+e^-$ events be N_Z.
- Let ϵ_{et} and ϵ_{em} be the efficiency for an electron to pass TIGHT++ and MEDIUM++, respectively.
- Let $P_{e\to\gamma}$ be the probability that a true electron passes TIGHTAR.
- Then

$$N_{ee} = \epsilon_{em}\epsilon_{et}N_Z \qquad (E_T^{em} > E_T^{et} \text{ and } M_Z \approx M_{ee}) \tag{10.2}$$

where N_{ee} is the number of events with $m_{inv} \approx m_Z$ and one TIGHT++ and one MEDIUM++ electron.

- Similarly, for $Z \to e^+e^-$ events in which one of the electrons is identified as a TIGHT++ electron and the other as a TIGHTAR photon, we define:

$$N_{\gamma e} = P_{e\to\gamma}\epsilon_{et}N_Z \qquad (E_T^{\gamma} > E_T^{et} \text{ and } M_Z \approx M_{e\gamma}) \tag{10.3}$$

as the number of observed $Z \to e^+e^-$ events of N_Z in which one of the electrons is misidentified as a photon. Then

$$N_{\gamma e} = P_{e\to\gamma}\epsilon_{et}N_Z = P_{e\to\gamma}\epsilon_{et}\frac{N_{ee}}{\epsilon_{em}\epsilon_{et}} \tag{10.4}$$

$$P_{e\to\gamma} = \epsilon_{em}\Big(\frac{N_{\gamma e}}{N_{ee}}\Big) \tag{10.5}$$

To obtain the electron-to-photon scale factor f from this probability, we consider the background from $W \to e\nu_e$ events. To estimate the expected contribution to the signal region, we select events in the control region with a MEDIUM++ electron.

- Let N_{truee} be the number of events with a true electron.

- Then

$$N_{em} = \epsilon_{em}N_{truee} \tag{10.6}$$

is the observed number of events with a true electron identified as a MEDIUM++ electron, and

$$N_\gamma = P_{e\to\gamma} N_{truee} \tag{10.7}$$

is the expected number of events in the photon sample with a true electron misidentified as a photon. We can rewrite this as:

$$N_\gamma = \frac{P_{e\to\gamma}}{\epsilon_{em}}(\epsilon_{em} N_{truee}) = \Big(\frac{N_{\gamma e}}{N_{ee}}\Big) N_{em} \tag{10.8}$$

and we define

$$f = \frac{N_{\gamma e}}{N_{ee}} \tag{10.9}$$

as the average scale factor we use to calculate electron faking photon backgrounds.

The scale factors for each η bin and their statistical uncertainties are shown in Table 10.2 for data and two Z→ee MC samples. The scale factors as a function of p_{T} are shown in Table 10.3. Increasing the p_{T} cut for the probe results in a decreased $e \to \gamma$ fake rate scale factor.

In order to estimate the systematic error on the fake rate scale factor, several factors were considered: the dependence on the fit range (60-120 GeV and 70-110 GeV were used), the fake rate using only events in a 80-100 GeV invariant mass range without fitting, and the distribution used to make the fit (Gaussian, Crystall Ball, and Breit-Wigner were also used). The effects of the defined mass range are shown in Table 10.4 and the effects of the fit shape are shown in Table 10.5. The result is a relative systematic uncertainty of ± 10% on the scale factor.

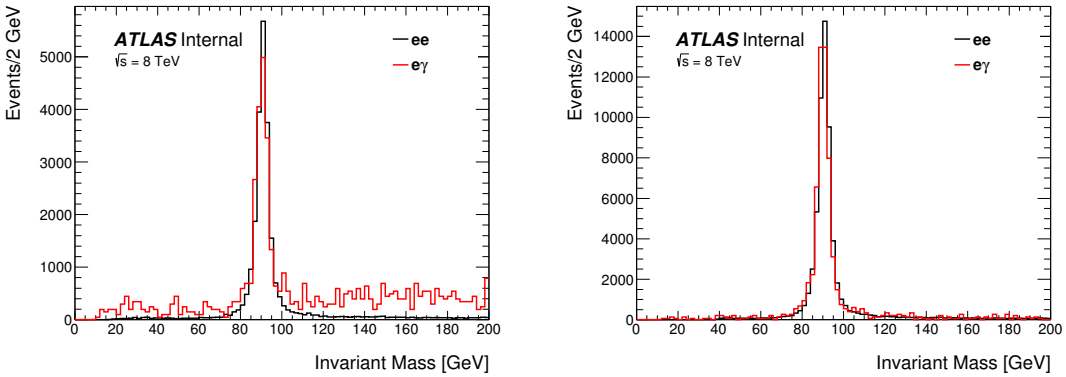

Figure 10.1: The invariant mass of e^+e^- candidates and $e^{\pm}\gamma$ candidates in data (left) and Sherpa simulation (right). Histograms are area normalized.

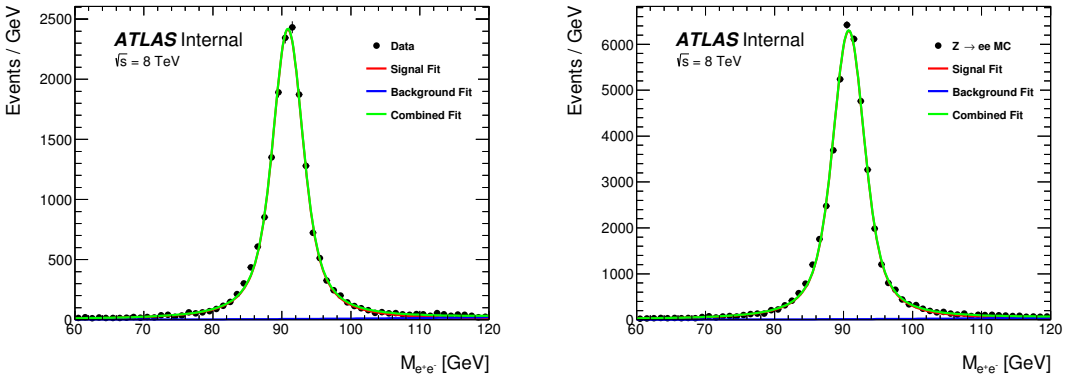

Figure 10.2: The invariant mass of e^+e^- candidates, inclusive in η, in data (left) and Sherpa simulation (right). The fit is performed using a Voigtian model for the Z peak and quadratic Bernstein polynomials for the background.

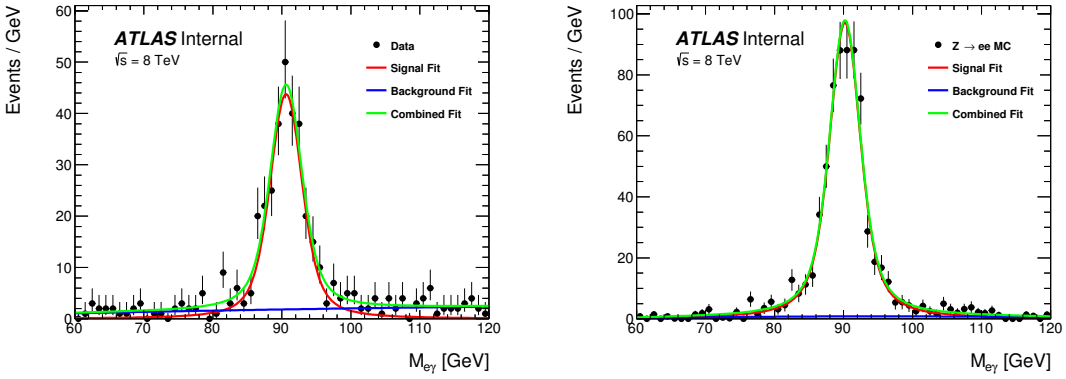

Figure 10.3: The invariant mass of $e^{\pm}\gamma$ candidates, inclusive in η, in data (left) and Sherpa simulation (right). The fit is performed using a Voigtian model for the Z peak and quadratic Bernstein polynomials for the background.

Table 10.2: Probability of an electron being reconstructed as a photon as a function of the probe η. The data estimate is shown along with the value calculated for Z→ee MC, using the Sherpa and Powheg generators. Uncertainties include statistical uncertainty and uncertainty on the fit parameters.

	Data	Sherpa Z → ee	Powheg Z → ee
$0 \leq \|\eta\| < 0.6$	0.012 ± 0.002	0.013 ± 0.001	0.013 ± 0.003
$0.6 \leq \|\eta\| < 1.37$	0.019 ± 0.002	0.011 ± 0.001	0.013 ± 0.002
$1.52 \leq \|\eta\| < 2.47$	0.034 ± 0.005	0.026 ± 0.002	0.019 ± 0.004
Overall	0.020 ± 0.001	0.015 ± 0.001	0.014 ± 0.002

Table 10.3: Probability of an electron being reconstructed as a photon for varying values of the probe p_{T} as a function of the probe η. The fake rate decreases substantially with an increased probe p_{T}. Uncertainties include statistical uncertainty and uncertainty on the fit parameters.

	75 GeV	100 GeV	125 GeV	150 GeV
$0 \leq \|\eta\| < 0.6$	0.021 ± 0.001	0.017 ± 0.002	0.012 ± 0.002	0.009 ± 0.002
$0.6 \leq \|\eta\| < 1.37$	0.022 ± 0.001	0.020 ± 0.001	0.019 ± 0.002	0.015 ± 0.003
$1.52 \leq \|\eta\| < 2.47$	0.037 ± 0.001	0.033 ± 0.002	0.034 ± 0.005	0.032 ± 0.008
Overall	0.025 ± 0.001	0.022 ± 0.001	0.020 ± 0.001	0.016 ± 0.002

Table 10.4: Probability of an electron being reconstructed as a photon for varying limits on the mass range used as a function of probe η. The 60-120 GeV and 70-110 GeV columns use the nominal fit distributions to do background subtraction, while the 80-100 GeV column has no background subtraction. Uncertainties include statistical uncertainty and uncertainty on the fit parameters (when applicable).

	$60 < m_{ee} < 120$	$70 < m_{ee} < 110$	$80 < m_{ee} < 100$
$0 \leq \|\eta\| < 0.6$	0.012 ± 0.002	0.011 ± 0.003	0.014 ± 0.001
$0.6 \leq \|\eta\| < 1.37$	0.019 ± 0.002	0.021 ± 0.003	0.020 ± 0.002
$1.52 \leq \|\eta\| < 2.47$	0.034 ± 0.005	0.034 ± 0.004	0.035 ± 0.003
Overall	0.020 ± 0.001	0.019 ± 0.002	0.020 ± 0.001

10.1.2.2 Electron control regions

In order to calculate the contribution of this background to the signal regions, control regions must be defined. In this case, the control regions (eCRL and eCRH)

Table 10.5: Probability of an electron being reconstructed as a photon for different signal distributions as a function of the probe η. Each is fit with a quadratic polynomial for the background. Voigtian was selected as the nominal fit due to having the best agreement between the fit and the distribution, as well as having the most conservative scale factors. Uncertainties include statistical uncertainty and uncertainty on the fit parameters.

	Voigtian	Crystal Ball	Gaussian	Breit-Wigner
$0 \leq \|\eta\| < 0.6$	0.012 ± 0.002	0.011 ± 0.002	0.011 ± 0.002	0.011 ± 0.002
$0.6 \leq \|\eta\| < 1.37$	0.019 ± 0.002	0.017 ± 0.002	0.018 ± 0.002	0.018 ± 0.002
$1.52 \leq \|\eta\| < 2.47$	0.034 ± 0.005	0.032 ± 0.004	0.030 ± 0.004	0.029 ± 0.004
Overall	0.020 ± 0.001	0.018 ± 0.001	0.017 ± 0.001	0.017 ± 0.001

consist of events that survive the selection criteria enumerated in Section 9.1 where the photon is replaced by a medium++ quality electron that fulfills the same requirements. These control regions, in addition to 2-lepton control regions that are used in Section 10.1.3, are described in Tables 10.6 and 10.7. Figures 10.4 and 10.5 compare MC and data in these control regions. The MC is normalized to 20.3 fb^{-1}, and both data and MC have the $e \to \gamma$ fake rate scale factor calculated in the previous section applied. Note that these figures also show the signal contamination to be quite small in the electron control regions. Figures 10.6 and 10.7 compare MC shapes in the $e \to \gamma$ control regions to MC in the signal region, again after application of the $e \to \gamma$ scale factor. The plots are normalized to unity.

The cut-flow of control region events are shown in Tables 10.8 and 10.9. After η-dependent scale factors are applied, the result is a prediction of 3.21 $\pm$ 0.27 (stat.) events in the low mass signal region and 0.18 $\pm$ 0.05 (stat.) events in the high mass signal region. These results are summarized in Tables 10.10 and 10.11, along with the electron misidentified as a photon contribution to several lepton control regions used in

the next section.

Table 10.6: Electron control regions for the low mass region. The first control region only replaces photon variables with corresponding electron variables. The remaining control regions, in addition to replacing the photon with an electron, require an extra lepton and have loosened $E_{\mathrm{T}}^{\mathrm{miss}}$ and $M_{b\bar{b}}$ cuts. These 2-lepton control regions are used in the following section.

Control Region	Required Leptons	$E_{\mathrm{T}}^{\mathrm{miss}}$ cut	$M_{b\bar{b}}$ cut
eCRL	≥ 1	> 100 GeV	> 75 GeV AND < 150 GeV
eLCR1L	≥ 2	> 25 GeV	None
eLCR2L	≥ 2	> 50 GeV	None
eLCR3L	≥ 2	> 75 GeV	None
eLCR4L	≥ 2	> 100 GeV	None
eLCR5L	≥ 2	> 125 GeV	None

Table 10.7: Electron control regions for the high mass region. The first control region only replaces photon variables with corresponding electron variables. The remaining control regions, in addition to replacing the photon with an electron, require an extra lepton and have loosened $E_{\mathrm{T}}^{\mathrm{miss}}$ and H_{T} cuts. $E_{\mathrm{T}}^{\mathrm{miss}}$ or H_{T} must be below the signal region threshold in order to stay orthogonal to the signal region. These 2-lepton control regions are used in the following section.

Control Region	Required Leptons	$E_{\mathrm{T}}^{\mathrm{miss}}$ cut	H_{T} cut	Add'l Comment
eCRH	≥ 1	> 200 GeV	> 1000 GeV	
eLCR1H	≥ 2	> 50 GeV	> 700 GeV	$E_{\mathrm{T}}^{\mathrm{miss}} < 200$ GeV OR $H_{\mathrm{T}} < 1000$ GeV
eLCR2H	≥ 2	> 50 GeV	> 500 GeV	$E_{\mathrm{T}}^{\mathrm{miss}} < 200$ GeV OR $H_{\mathrm{T}} < 1000$ GeV
eLCR3H	≥ 2	> 100 GeV	> 700 GeV	$E_{\mathrm{T}}^{\mathrm{miss}} < 200$ GeV OR $H_{\mathrm{T}} < 1000$ GeV
eLCR4H	≥ 2	> 100 GeV	> 500 GeV	$E_{\mathrm{T}}^{\mathrm{miss}} < 200$ GeV OR $H_{\mathrm{T}} < 1000$ GeV

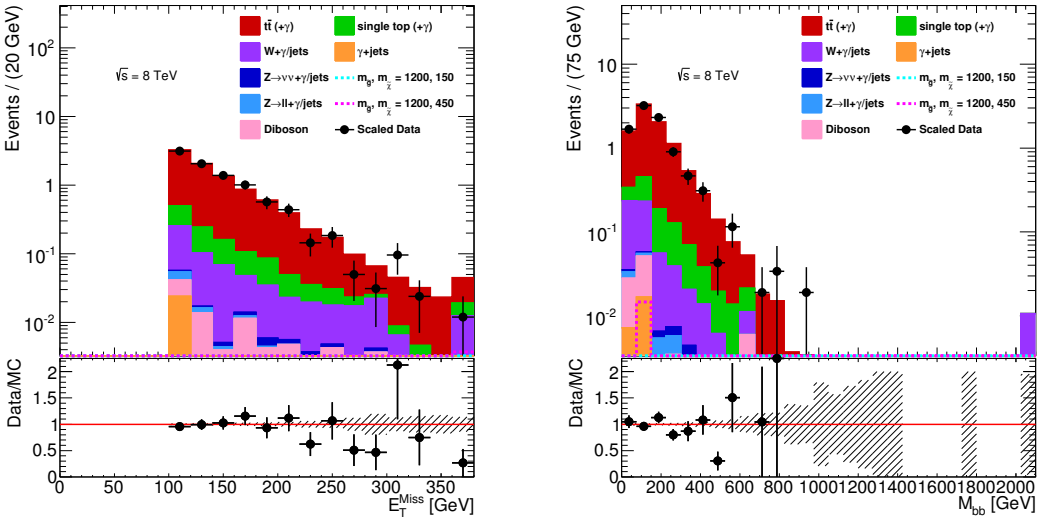

Figure 10.4: Data/MC comparison in low mass $e \to \gamma$ control region for variables $E_{\mathrm{T}}^{\mathrm{miss}}$ (left) and $M_{b\bar{b}}$. MC is normalized to 20.3 fb^{-1}. Both data and MC have applied $e \to \gamma$ scale factor calculated in Section 10.1.2.1.

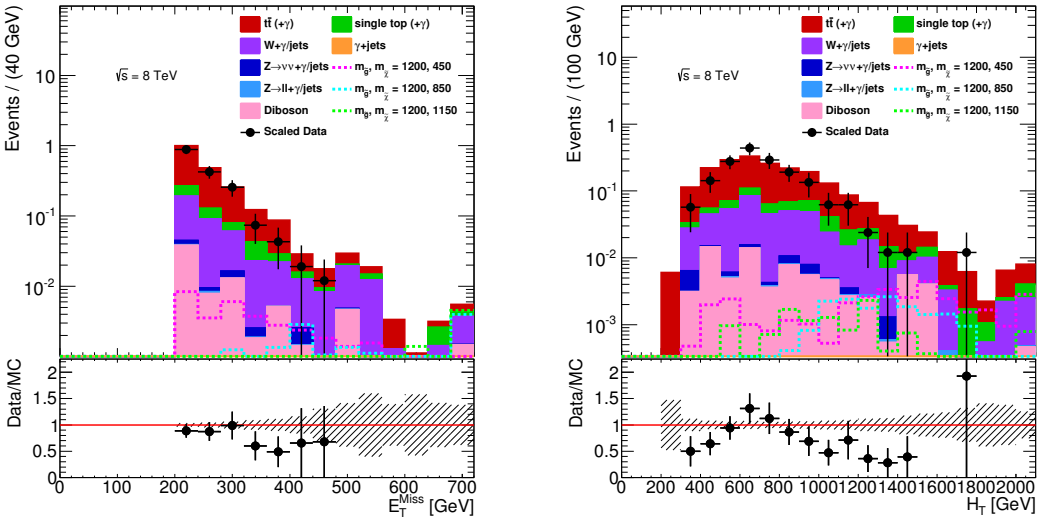

Figure 10.5: Data/MC comparison in high mass $e \to \gamma$ control region for variables $E_{\mathrm{T}}^{\mathrm{miss}}$ (left) and H_{T}. MC is normalized to 20.3 fb^{-1}. Both data and MC have applied $e \to \gamma$ scale factor calculated in Section 10.1.2.1.

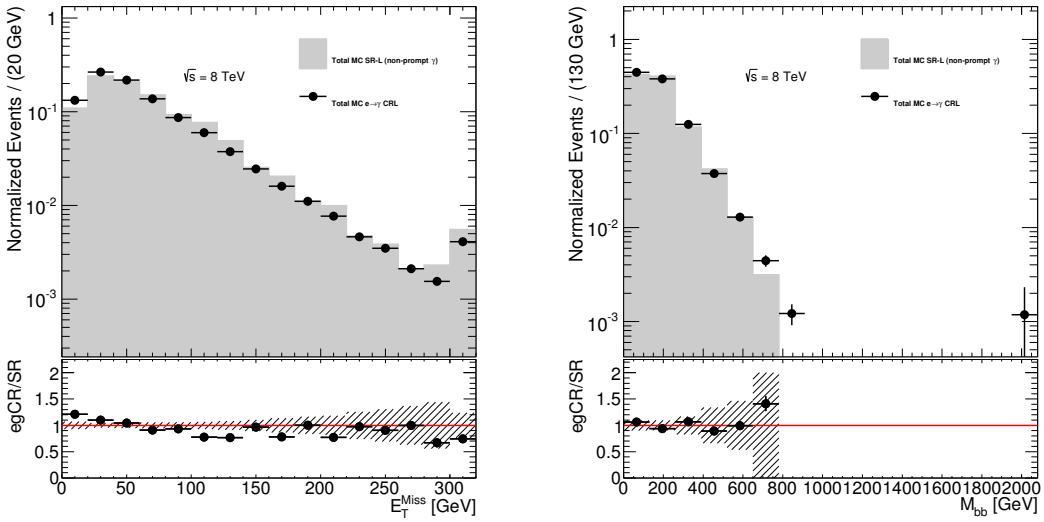

Figure 10.6: Comparison of normalized MC shape in low mass signal region and low mass $e \to \gamma$ control region for variables $E_{\mathrm{T}}^{\mathrm{miss}}$ (left) and $M_{b\bar{b}}$.

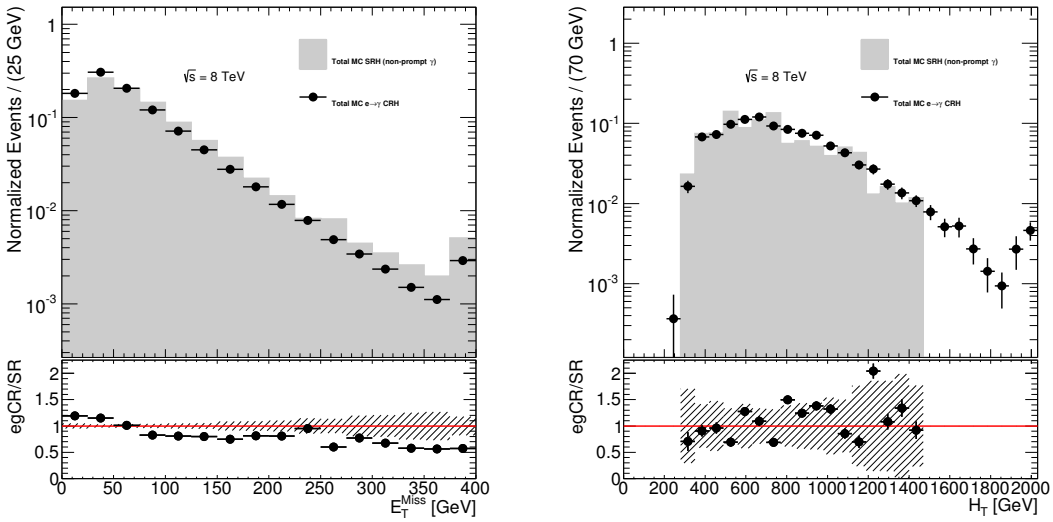

Figure 10.7: Comparison of normalized MC shape in high mass signal region and high mass $e \to \gamma$ control region for variables $E_{\mathrm{T}}^{\mathrm{miss}}$ (left) and H_{T}.

Table 10.8: The cut-flow of events where the photon is replaced by an electron in the low mass region. Datasets are normalized to 20.3 fb^{-1}.

Cut	Data	$t\bar{t}$ (+γ)	$W+\gamma$/jets	Single Top
p_T^e > 125 GeV	1227500 ± 1100	39058 ± 40	312260 ± 440	6431 ± 18
$2 \leq N_{\text{jets}} \leq 4$	786510 ± 890	22732 ± 31	183820 ± 230	4564 ± 15
One b-tagged jet	100940 ± 320	17775 ± 27	18098 ± 60	3213 ± 13
Two b-tagged jet	14640 ± 120	6486 ± 16	1143 ± 11	746.6 ± 6.2
Lepton Veto	13020 ± 110	5121 ± 14	1140 ± 11	662.2 ± 5.9
$E_{\text{T}}^{\text{miss}}$ > 100 GeV	1192 ± 35	1004.6 ± 6.2	105.8 ± 2.9	123.1 ± 2.5
M_{T} > 90 GeV	679 ± 26	590.2 ± 4.8	36.6 ± 2.1	50.2 ± 1.4
$\Delta\phi_{\text{min}}(E_{\text{T}}^{\text{miss}}, \text{j}_{1,2})$ > 0.3	534 ± 23	487.7 ± 4.3	29.9 ± 1.9	41.7 ± 1.3
75 GeV <$M_{b\bar{b}}$< 150 GeV	188 ± 14	176.5 ± 2.6	9.9 ± 1.0	14.09 ± 0.72

Table 10.9: The cut-flow of events where the photon is replaced by an electron in the high mass region. Datasets are normalized to 20.34 fb^{-1}.

Cut	Data	$t\bar{t}$ (+γ)	$W+\gamma$/jets	Single Top
p_T^e > 150 GeV	636070 ± 800	19006 ± 28	147840 ± 290	3431 ± 13
$N_{\text{jets}} \geq 4$	123700 ± 350	12476 ± 23	22590 ± 66	1501.1 ± 8.2
One b-tagged jet	29730 ± 170	10444 ± 21	3540 ± 20	1182.8 ± 7.2
$E_{\text{T}}^{\text{miss}}$ > 200 GeV	460 ± 21	394.6 ± 4.0	125.4 ± 3.3	57.8 ± 1.7
M_{T} > 90 GeV	170 ± 13	150.4 ± 2.5	27.6 ± 2.0	15.85 ± 0.82
$\Delta\phi_{\text{min}}(E_{\text{T}}^{\text{miss}}, \text{j}_{1\ldots4})$ > 0.3	112 ± 11	92.0 ± 1.9	21.4 ± 1.9	11.38 ± 0.70
H_{T} > 1000 GeV	16 ± 4	18.13 ± 0.87	4.68 ± 0.59	3.81 ± 0.43

Table 10.10: Electron faking a photon background in the low mass signal and control regions as predicted for data, $t\bar{t}$,$W+\gamma$/jets, and single top samples. 'lepton' stands for a lepton requirement in the event.

Sample	eCRL	eLCR1L	eLCR2L	eLCR3L	eLCR4L	eLCR5L
$t\bar{t}$	2.87 ± 0.05	12.98 ± 0.10	10.30 ± 0.09	6.94 ± 0.07	4.11 ± 0.06	2.35 ± 0.04
$t\bar{t}$ +γ	0.010 ± 0.002	0.055 ± 0.005	0.044 ± 0.004	0.032 ± 0.004	0.019 ± 0.003	0.013 ± 0.002
single top	0.22 ± 0.01	0.75 ± 0.02	0.61 ± 0.02	0.41 ± 0.02	0.24 ± 0.01	0.14 ± 0.01
single top+γ	0.0012 ± 0.0004	0.0063 ± 0.0008	0.0044 ± 0.0007	0.0023 ± 0.0004	0.0012 ± 0.0003	0.0006 ± 0.0002
W+jets	0.17 ± 0.02	0.016 ± 0.004	0.014 ± 0.004	0.010 ± 0.003	0.006 ± 0.002	0.0020 ± 0.0009
$W+\gamma$	0.002 ± 0.001	0.004 ± 0.001	0.003 ± 0.001	0.002 ± 0.001	0.0008 ± 0.0007	0.0008 ± 0.0007
Total MC	3.28 ± 0.05	13.81 ± 0.10	10.98 ± 0.09	7.39 ± 0.08	4.38 ± 0.06	2.51 ± 0.04
Scaled Data, 20.34 fb^{-1}	3.21 ± 0.27	13.75 ± 0.52	10.63 ± 0.46	6.37 ± 0.35	3.72 ± 0.27	2.11 ± 0.21

Table 10.11: Electron faking a photon background in the high mass signal and control regions as predicted for data, $t\bar{t}$,$W + \gamma$/jets, and single top samples.

Sample	eCRH	eLCR1H	eLCR2H	eLCR3H	eLCR4H
$t\bar{t}$	0.27 ± 0.01	1.45 ± 0.03	3.41 ± 0.05	0.73 ± 0.02	1.59 ± 0.04
$t\bar{t}$ +γ	0.0018 ± 0.0008	0.010 ± 0.002	0.025 ± 0.003	0.005 ± 0.001	0.011 ± 0.002
single top	0.056 ± 0.007	0.105 ± 0.008	0.24 ± 0.01	0.061 ± 0.006	0.125 ± 0.009
single top+γ	0.0005 ± 0.0002	0.0020 ± 0.0004	0.0044 ± 0.0007	0.0005 ± 0.0002	0.0013 ± 0.0004
W+jets	0.067 ± 0.009	0.03 ± 0.01	0.04 ± 0.01	0.02 ± 0.01	0.02 ± 0.01
$W + \gamma$	0.0011 ± 0.0008	0.007 ± 0.002	0.008 ± 0.003	0.002 ± 0.001	0.002 ± 0.001
Total MC	0.40 ± 0.02	1.60 ± 0.04	3.72 ± 0.05	0.82 ± 0.03	1.75 ± 0.04
Scaled Data, 20.34 fb^{-1}	0.18 ± 0.05	1.62 ± 0.17	3.50 ± 0.26	0.75 ± 0.12	1.64 ± 0.18

A comparison is also done between the p_{T} of the electrons in the tag and probe sample to the p_{T} of the electrons used in the control regions. This is done to ensure that the tag and probe sample is representative of the electrons to which the fake rate scale factor is applied. Figure 10.8 shows this comparison for both the eCRL and eCRH control regions using p_{T} distributions normalized to unity. It is seen that the p_{T} distributions are very similar for the low mass sample, but that the high mass sample is slightly harder than the tag and probe sample. Thus, the result for the high mass region is likely slightly conservative since the fake rate is decreasing for higher electron p_{T}.

A study has been carried out to estimate the effect of the difference in electron p_{T} distributions by weighting events in eCRL and eCRH in order to match the distributions from the tag and probe region. Tables 10.12 and 10.13 show the weights that were applied in eCRL and eCRH, respectively. The predictions for the electron faking photon background with these weights applied are 3.17 ± 0.26 for the low mass region and $0.12 \pm .04$ for the high mass region. This is a difference of 1.2% for the low mass result and 33% for the high mass result. The 33% difference for the high mass region is taken as a systematic error on the result.

After all systematics have been taken into account, the final result for this background is 3.21 ± 0.27 (stat.) ± 0.32 (syst.) events in the low mass signal region and 0.18 ± 0.05 (stat.) ± 0.06 (syst.) events in the high mass region.

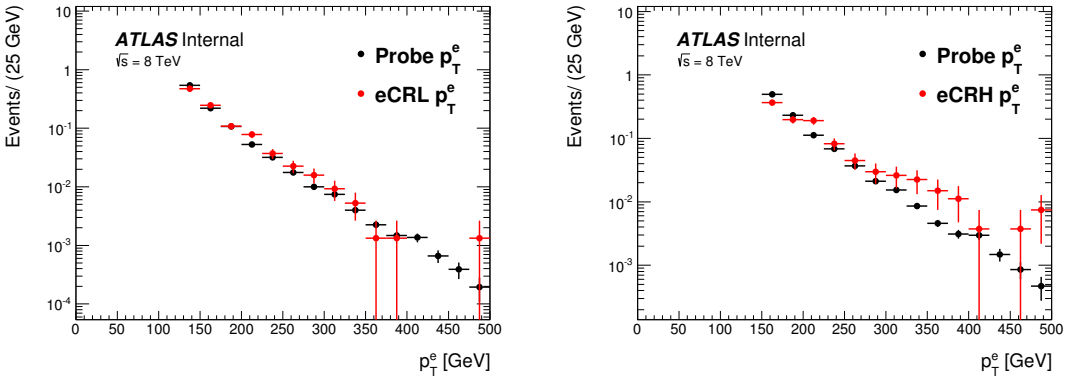

Figure 10.8: Comparison of normalized electron p_{T} in tag and probe sample and eCRL (left) and eCRH. The eCRL sample has all cuts applied except for the $M_{b\bar{b}}$ cut, and the eCRH sample has all cuts applied except for H_{T}.

Table 10.12: The scale factors applied to the events in eCRL in order to match the p_{T} distribution of the probe electron.

p_{T} range [GeV]	scale factor
0 - 125	0
125 - 150	1.12349
150 - 175	0.94951
175 - 200	0.889871
200 - 250	0.776197
250 - 300	0.844573
300 - 400	0.821939
400 - 1000	0.664699

Table 10.13: The scale factors applied to the events in eCRH in order to match the p_{T} distribution of the probe electron.

p_{T} range [GeV]	scale factor
0 - 150	0
150 - 175	1.66991
175 - 200	0.995822
200 - 250	0.651654
250 - 300	0.59366
300 - 400	0.403211
400 - 1000	0.373886

10.1.3 Background containing $W \to l\nu$ processes with prompt photon and jets faking a photon.

As shown in Tables 9.1 and 9.2 in Section 9.1, the $t\bar{t}$ ($+\gamma$), single top($+\gamma$), and W+γ/jets backgrounds are large contributors to the total background containing $W \to l\nu$ processes. In addition to the prompt photon contribution, some events may also survive the selection cuts provided a jet or a τ-lepton faked a photon. It is difficult to separate these events from genuine prompt photon events, so both sources are treated together.

By requiring the presence of a lepton in addition to the signal region cuts (including a high p_{T} photon), one obtains a 'lepton' control sample that allows for estimating the background containing $W \to l\nu$ processes. The lepton requirement suppresses the QCD and signal contamination in the control region and allows one to use lower $E_{\mathrm{T}}^{\mathrm{miss}}$ threshold in order to increase the number of events in the control sample and reduce the uncertainty. Additionally, for the control regions for the low mass region, the $\mathrm{M}_{b\bar{b}}$ cut is not applied in order to increase statistics. These relaxations have little effect on the contributions of different backgrounds to the control regions while greatly increasing MC and data statistics. The selected control region is defined by 'lepton + $E_{\mathrm{T}}^{\mathrm{miss}} > 125$ GeV' for the low mass region, with other $E_{\mathrm{T}}^{\mathrm{miss}}$ cut values studied as well. For the high mass region, the selected control region is defined by 'lepton + $E_{\mathrm{T}}^{\mathrm{miss}} > 50$ GeV + $H_{\mathrm{T}} > 500$ GeV'. In addition, either $E_{\mathrm{T}}^{\mathrm{miss}} < 200$ GeV or $H_{\mathrm{T}} < 1000$ GeV is required so that the control region is orthogonal to the signal region. Different options for the lower cut value of $E_{\mathrm{T}}^{\mathrm{miss}}$ and H_{T} were studied as well. The control regions tested

are described in Tables 10.14 and 10.15. These control regions are used to calculate a transfer factor (ratio of MC events in SR and CR) that is applied to the data in the control region to predict the contribution in the signal region.

Table 10.14: Lepton control regions for the low mass region. The control regions consist of a required lepton and loosened $E_{\mathrm{T}}^{\mathrm{miss}}$ and $M_{b\bar{b}}$ cuts. Corresponding control regions are defined with required electrons instead of photons and are labeled eLCR.

Control Region	Required Leptons	$E_{\mathrm{T}}^{\mathrm{miss}}$ cut	$M_{b\bar{b}}$ cut
LCR1L	≥ 1	> 25 GeV	None
LCR2L	≥ 1	> 50 GeV	None
LCR3L	≥ 1	> 75 GeV	None
LCR4L	≥ 1	> 100 GeV	None
LCR5L	≥ 1	> 125 GeV	None

Table 10.15: Lepton control regions for the high mass region. The control regions consist of a required lepton and loosened $E_{\mathrm{T}}^{\mathrm{miss}}$ and H_{T} cuts. $E_{\mathrm{T}}^{\mathrm{miss}}$ or H_{T} must be below the signal region threshold in order to stay orthogonal to the signal region. Corresponding control regions are defined with required electrons instead of photons and are labeled eLCR.

Control Region	Required Leptons	$E_{\mathrm{T}}^{\mathrm{miss}}$ cut	H_{T} cut	Add'l Comment
LCR1H	≥ 1	> 50 GeV	> 700 GeV	$E_{\mathrm{T}}^{\mathrm{miss}} < 200$ GeV OR $H_{\mathrm{T}} < 1000$ GeV
LCR2H	≥ 1	> 50 GeV	> 500 GeV	$E_{\mathrm{T}}^{\mathrm{miss}} < 200$ GeV OR $H_{\mathrm{T}} < 1000$ GeV
LCR3H	≥ 1	> 100 GeV	> 700 GeV	$E_{\mathrm{T}}^{\mathrm{miss}} < 200$ GeV OR $H_{\mathrm{T}} < 1000$ GeV
LCR4H	≥ 1	> 100 GeV	> 500 GeV	$E_{\mathrm{T}}^{\mathrm{miss}} < 200$ GeV OR $H_{\mathrm{T}} < 1000$ GeV

The number of events in the signal region and various control regions as pre-

dicted by the $t\bar{t}$, single top, and W Monte Carlo are shown in Tables 10.16 and 10.17. As seen from these tables, the sum of the $t\bar{t}$, single top and W background predictions for the control regions LCR1 and LCR2 are in agreement with the data for the low mass region, indicating that the QCD contamination into the control region is small and also serving as proof that the $t\bar{t}$ and W backgrounds are indeed the dominant contributors of all the background containing $W \to l\nu$ processes. In the higher $E_{\mathrm{T}}^{\mathrm{miss}}$ control regions, however, the MC underestimates the data fairly significantly. There is no significant contribution from other processes, so perhaps this is a statistical fluctuation in the data or the MC poorly models the data in this region. In the high mass control regions, the MC matches the data fairly well in each of the control regions, confirming that $t\bar{t}$ and W are the dominant contributors in these regions.

Table 10.16: Prompt and jet faking photon background in the low mass signal and control regions as predicted for data, $t\bar{t}$,$W + \gamma$/jets, and single top samples. The label 'L' for 'lepton' stands for a lepton requirement in the event.

Sample	SRL	LCR1L	LCR2L	LCR3L	LCR4L	LCR5L
$t\bar{t}$	3.03 ± 0.33	16.73 ± 0.80	12.89 ± 0.70	8.47 ± 0.57	4.74 ± 0.43	2.94 ± 0.34
$t\bar{t}$ +γ	6.77 ± 0.36	43.84 ± 0.91	33.57 ± 0.79	21.96 ± 0.64	14.09 ± 0.51	8.90 ± 0.41
single top	0.38 ± 0.14	0.91 ± 0.21	0.70 ± 0.18	0.37 ± 0.11	0.32 ± 0.10	0.17 ± 0.08
single top+γ	0.76 ± 0.06	4.91 ± 0.14	3.51 ± 0.12	2.12 ± 0.09	1.27 ± 0.07	0.75 ± 0.06
W+jets	0.29 ± 0.15	0.36 ± 0.23	0.12 ± 0.06	0.11 ± 0.06	0.10 ± 0.06	0.07 ± 0.05
$W + \gamma$	1.54 ± 0.25	8.95 ± 0.63	6.28 ± 0.52	3.76 ± 0.40	2.50 ± 0.33	1.68 ± 0.27
Total MC	12.76 ± 0.59	75.7 ± 1.4	57.1 ± 1.2	36.79 ± 0.96	23.02 ± 0.76	14.52 ± 0.61
Data, 20.34 fb^{-1}		84.0 ± 9.2	63.0 ± 7.9	47.0 ± 6.9	34.0 ± 5.8	18.0 ± 4.2

In Tables 10.18 and 10.19, the electron faking photon portion is removed (the

Table 10.17: Prompt and jet faking photon background in the high mass signal and control regions as predicted for data, $t\bar{t}$,$W + \gamma$/jets, and single top samples. The label 'L' for 'lepton' stands for a lepton requirement in the event. The control regions require that either $E_{\mathrm{T}}^{\mathrm{miss}} < 200$ GeV or $H_{\mathrm{T}} < 1000$ GeV in order to be orthogonal to the signal region.

Sample	SRH	LCR1H	LCR2H	LCR3H	LCR4H
$t\bar{t}$	0.45 ± 0.15	1.81 ± 0.28	5.76 ± 0.49	1.01 ± 0.22	2.73 ± 0.35
$t\bar{t}$ +γ	0.97 ± 0.14	13.99 ± 0.53	35.07 ± 0.84	6.54 ± 0.36	15.49 ± 0.56
single top	0.02 ± 0.01	0.07 ± 0.04	0.18 ± 0.07	0.07 ± 0.04	0.15 ± 0.06
single top+γ	0.17 ± 0.03	2.40 ± 0.10	4.41 ± 0.14	0.89 ± 0.06	1.58 ± 0.08
W+jets	0.10 ± 0.07	0.09 ± 0.05	0.57 ± 0.40	0.06 ± 0.04	0.15 ± 0.07
$W + \gamma$	1.84 ± 0.30	6.84 ± 0.55	12.00 ± 0.72	2.61 ± 0.34	4.57 ± 0.44
Total MC	3.55 ± 0.37	25.20 ± 0.82	58.0 ± 1.3	11.18 ± 0.55	24.67 ± 0.80
Data, 20.34 fb^{-1}		28.0 ± 5.3	61.0 ± 7.8	12.0 ± 3.5	23.0 ± 4.8

values subtracted are shown previously in Section 10.1.2.2 in Tables 10.10 and 10.11), and the final prediction for each control region is presented. The electron faking photon portion must be removed because dilepton events could potentially be considered by both background estimation techniques if one of the leptons is a high p_{T} electron. The transfer factor is calculated by taking the ratio of number of MC events in the control and the signal regions. By multiplying the transfer factor to the number of data events in the control region, all of the events with $E_{\mathrm{T}}^{\mathrm{miss}}$ resulting from a $W \to l\nu$ decay are estimated. Alternatively, this calculation can be thought of as normalizing the Monte Carlo in the lepton control region.

Predictions for five different control regions for the low mass region and four different control regions for the high mass region are shown. In each case, there is one outlier from the other results; however, the outliers are consistent with the other results

within the stated statistical uncertainties from data and MC. For SRL, LCR2L was initially chosen as the nominal and LCR5L did not exist, but due to the large difference between the LCR2L and LCR4L predictions, LCR5L was created and selected as the nominal. The large uncertainty covers the range from the LCR2L prediction to the LCR5L prediction. For SRH, LCR2H was chosen as the nominal due to it having the highest statistics of the regions, and the good agreement with the other regions is evidence that the looser cuts on $E_{\mathrm{T}}^{\mathrm{miss}}$ and H_{T} do not introduce mismodeling. LCR5L and LCR2H were tested for signal contamination, with the results described in Appendix B.1. It is measured to be insignificant in regions near the final limit.

As an additional systematic check on the transfer factor calculation, it is calculated using only the prompt photon samples without any $e \to \gamma$ subtraction for the MC. The result using LCR5L using this method is 9.9 ± 2.7 events, which is a difference of 2.7 events with respect to the nominal calculation. The result using LCR2H using this method is 2.96 ± 0.52 events, which is a difference of .39 events with respect to the nominal calculation. These differences are taken as a systematic error on the result. The final predictions for the prompt photon and jet faking photon background (using the results from LCR5L and LCR2H) are 12.6 ± 3.4 (stat.) $\pm$ 3.5 (syst.) events for the low mass region and 3.35 ± 0.45 (stat.) $\pm$ 0.94 (syst.) events for the high mass region. In addition to the systematics mentioned here, there is a significant contribution from scale variations. The calculation of these uncertainties is outlined in Appendix C.

Table 10.18: Prompt and jet faking photon background with electron faking photon removed in the low mass signal and control regions as predicted for data, $t\bar{t}$,$W+\gamma$/jets, and single top samples. The label 'L' stands for a lepton requirement in the event. The transfer factor is calculated by dividing the MC in SRL by the MC in LCRL, with electron faking photon contribution subtracted in each region. The transfer factor is then multiplied by the data measured in the LCR, also with the electron faking photon contribution subtracted.

Sample	SRL - eCRL	LCR1L - eLCR1L	LCR2L - eLCR2L	LCR3L - eLCR3L	LCR4L - eLCR4L	LCR5L - eLCR5L
$t\bar{t}$	0.16 ± 0.33	3.75 ± 0.81	2.59 ± 0.71	1.53 ± 0.57	0.62 ± 0.43	0.58 ± 0.34
$t\bar{t}$ +γ	6.76 ± 0.36	43.78 ± 0.91	33.53 ± 0.79	21.92 ± 0.64	14.07 ± 0.51	8.89 ± 0.41
single top	0.16 ± 0.14	0.16 ± 0.21	0.09 ± 0.18	-0.04 ± 0.11	0.08 ± 0.10	0.02 ± 0.08
single top+γ	0.76 ± 0.06	4.90 ± 0.14	3.50 ± 0.12	2.12 ± 0.09	1.27 ± 0.07	0.75 ± 0.06
W+jets	0.12 ± 0.15	0.34 ± 0.23	0.11 ± 0.06	0.10 ± 0.06	0.10 ± 0.06	0.07 ± 0.05
$W+\gamma$	1.53 ± 0.25	8.94 ± 0.63	6.28 ± 0.52	3.76 ± 0.40	2.50 ± 0.33	1.68 ± 0.27
Total MC	9.48 ± 0.59	61.9 ± 1.4	46.1 ± 1.2	29.40 ± 0.96	18.64 ± 0.76	12.01 ± 0.61
Combined Data, 20.34 fb^{-1}		70.3 ± 9.2	52.4 ± 8.0	40.6 ± 6.9	30.3 ± 5.8	15.9 ± 4.2
Transfer Factor		0.15 ± 0.01	0.21 ± 0.01	0.32 ± 0.02	0.51 ± 0.04	0.79 ± 0.06
Prediction		10.8 ± 1.6	10.8 ± 1.8	13.1 ± 2.4	15.4 ± 3.2	12.6 ± 3.5

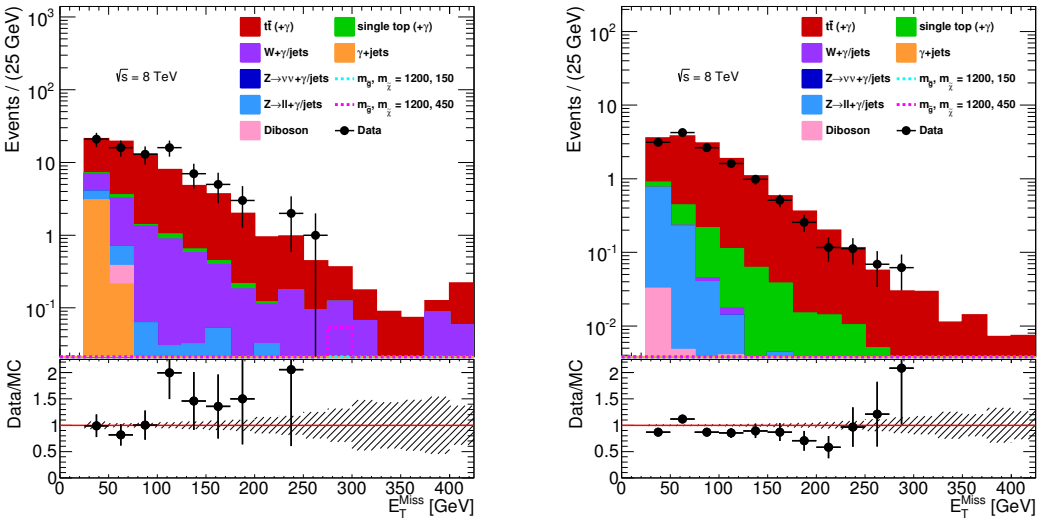

Figure 10.9: The $E_{\mathrm{T}}^{\mathrm{miss}}$ distribution in LCR1L (left) and eLCR1L (right) in data and MC. The integral of the right histogram is subtracted from the left before applying the transfer factor. MC samples are normalized to 20.34 fb^{-1}. The other control regions are each a subset of this control region with tighter $E_{\mathrm{T}}^{\mathrm{miss}}$ cuts.

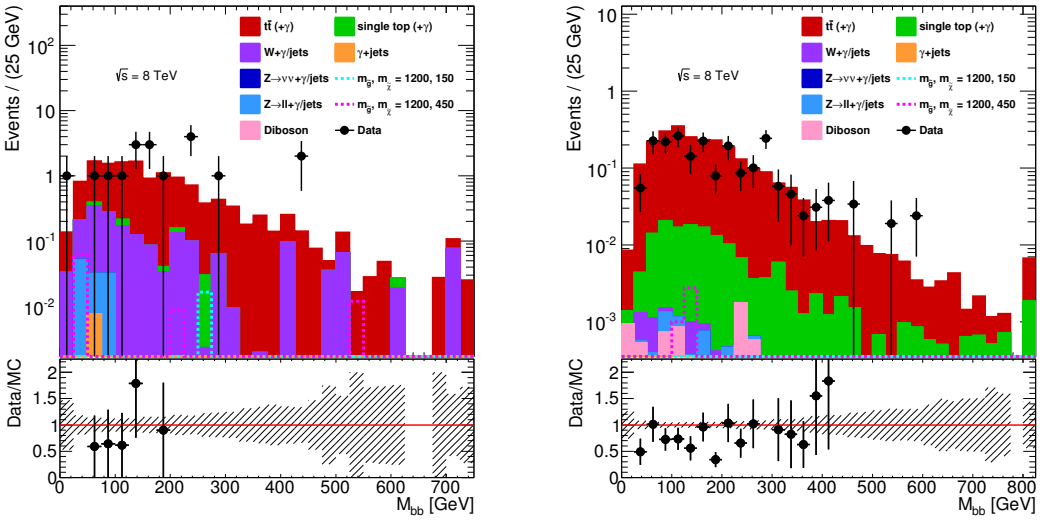

Figure 10.10: The $M_{b\bar{b}}$ distribution in LCR5L (left) and eLCR5L (right) in data and MC. The integral of the right histogram is subtracted from the left before applying the transfer factor. MC samples are normalized to 20.34 fb^{-1}.

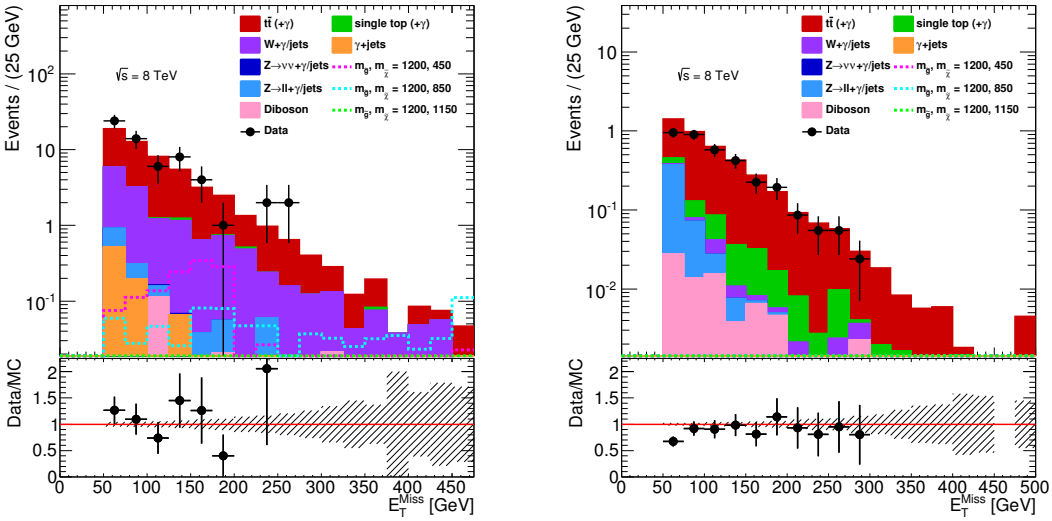

Figure 10.11: The $E_{\mathrm{T}}^{\mathrm{miss}}$ distribution in LCR2H (left) and eLCR2H (right) in data and MC. The integral of the right histogram is subtracted from the left before applying the transfer factor. MC samples are normalized to 20.34 fb^{-1}.

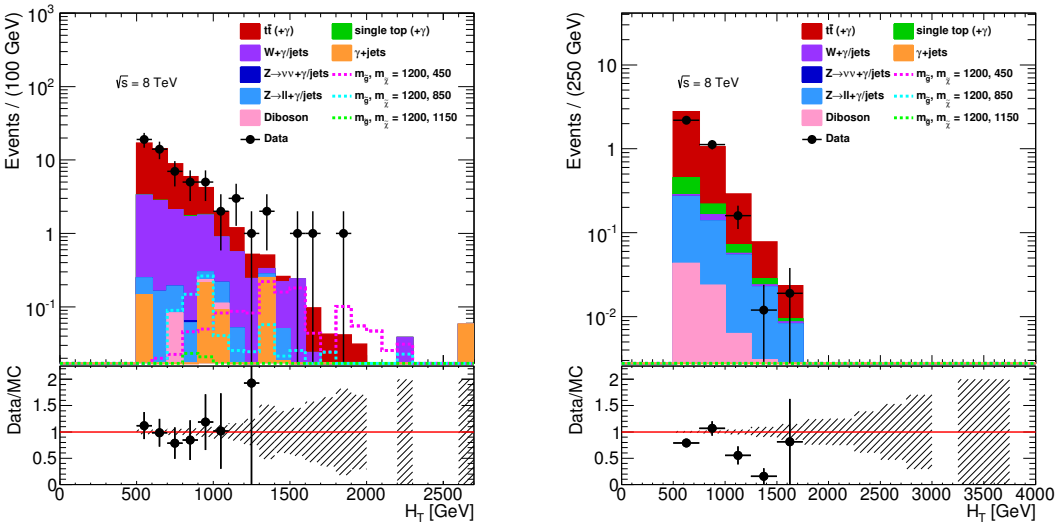

Figure 10.12: The H_{T} distribution in LCR2H (left) and eLCR2H (right) in data and MC. The integral of the right histogram is subtracted from the left before applying the transfer factor. MC samples are normalized to 20.34 fb^{-1}.

Table 10.19: Prompt and jet faking photon background with electron faking photon removed in the high mass signal and control regions as predicted for data, $t\bar{t}$,$W+\gamma$/jets, and single top samples. The label 'L' stands for a lepton requirement in the event. The control regions require that either $E_{\mathrm{T}}^{\mathrm{miss}} < 200$ GeV or $H_{\mathrm{T}} < 1000$ GeV in order to be orthogonal to the signal region. The transfer factor is calculated by dividing the MC in SRL by the MC in LCRL, with electron faking photon contribution subtracted in each region. The transfer factor is then multiplied by the data measured in the LCR, also with the electron faking photon contribution subtracted.

Sample	SRH - eCRH	LCR1H - eLCR1H	LCR2H - eLCR2H	LCR3H - eLCR3H	LCR4H - eLCR4H
$t\bar{t}$	0.18 ± 0.15	0.36 ± 0.28	2.35 ± 0.49	0.28 ± 0.22	1.14 ± 0.35
$t\bar{t}$ +γ	0.97 ± 0.14	13.98 ± 0.53	35.05 ± 0.84	6.54 ± 0.36	15.48 ± 0.56
single top	-0.04 ± 0.01	-0.03 ± 0.04	-0.07 ± 0.07	0.01 ± 0.04	0.02 ± 0.06
single top+γ	0.17 ± 0.03	2.40 ± 0.10	4.40 ± 0.14	0.89 ± 0.06	1.58 ± 0.08
W+jets	0.03 ± 0.07	0.06 ± 0.05	0.54 ± 0.40	0.04 ± 0.04	0.12 ± 0.07
$W + \gamma$	1.84 ± 0.30	6.83 ± 0.55	11.99 ± 0.72	2.61 ± 0.34	4.57 ± 0.44
Total MC	3.16 ± 0.37	23.60 ± 0.82	54.3 ± 1.3	10.36 ± 0.55	22.91 ± 0.80
Combined Data, 20.34 fb^{-1}		26.4 ± 5.3	57.5 ± 7.8	11.3 ± 3.5	21.4 ± 4.8
Transfer Factor		0.13 ± 0.02	0.058 ± 0.007	0.30 ± 0.04	0.14 ± 0.02
Prediction		3.53 ± 0.83	3.35 ± 0.60	3.4 ± 1.1	2.95 ± 0.75

10.1.4 QCD Events

QCD processes may give rise to a significant background due to their high cross section, despite the fact that the signal selection cuts strongly suppress QCD induced final states. The low rate of signal-like events makes the MC study unreliable, first because only a handful of such events can be simulated, and second because it is based on very rare cases of the simulation. This makes a data-driven verification of the background estimation of paramount importance.

Photons are relatively rare in QCD events, but the γ+jet contribution is still dominant. In addition, photons can be faked by jets that hadronize to a well-isolated

π^0 that passes tight photon requirements.

High $E_{\mathrm{T}}^{\mathrm{miss}}$ is also rare in QCD events and can be produced by mis-measuring jet p_T or by heavy flavor decays involving neutrinos. In either of these cases, the $E_{\mathrm{T}}^{\mathrm{miss}}$ is likely to be in the direction of the leading or sub-leading jet, and the $E_{\mathrm{T}}^{\mathrm{miss}}$ isolation cut is effective in reducing the background.

Since b-jets are relatively rare in QCD events and QCD events without b-jets are much more common, a low b-tag fake rate is extremely important. As discussed in Section 9.2, the optimization resulted in the requirement of a single tag in SRH and two tags in SRL.

Despite the rarity of QCD events with these features, it still may contribute significantly to the total background. In order to estimate the amount, a data-driven ABCD method utilizing control regions containing events that fail the b-tag requirement and events with low $E_{\mathrm{T}}^{\mathrm{miss}}$ are used. A scale factor between the tagged and untagged samples is obtained by looking at the low $E_{\mathrm{T}}^{\mathrm{miss}}$ region. This scale factor is then applied to the high $E_{\mathrm{T}}^{\mathrm{miss}}$ region of the untagged control sample. Due to contamination from events with genuine $E_{\mathrm{T}}^{\mathrm{miss}}$ in this region, Monte Carlo events from $t\bar{t}$, single top, and W/Z+jets samples are subtracted before the application of the scale factor. Because the two analyses have different cuts, the control regions have slightly different definitions. The regions for the low mass signal region are described in Table 10.20, and the regions for the high mass signal region are described in Table 10.21. The calculation for the signal regions is described by Equation 10.10.

Table 10.20: Definition of control samples for low mass signal region

$\geq$ 2 b-tag @ 0.7 OP	QCR1L	SRL
1 b-tag @ 0.7 OP	QCR2L	QCR3L
	$E_{\mathrm{T}}^{\mathrm{miss}} < 75$ GeV	$E_{\mathrm{T}}^{\mathrm{miss}} > 100$ GeV

Table 10.21: Definition of control samples for high mass signal region

$\geq$ 1 b-tag @ 0.7 OP	QCR1H	SRH
0 b-tag @ 0.7 OP	QCR2H	QCR3H
	$E_{\mathrm{T}}^{\mathrm{miss}} < 150$ GeV	$E_{\mathrm{T}}^{\mathrm{miss}} > 200$ GeV

Table 10.22: Definition of control samples for low mass validation region

$\geq$ 2 b-tag @ 0.7 OP	QCR1L	VR1L
1 b-tag @ 0.7 OP	QCR2L	QCR4L
	$E_{\mathrm{T}}^{\mathrm{miss}} < 75$ GeV	75 GeV $< E_{\mathrm{T}}^{\mathrm{miss}} < 100$ GeV

Table 10.23: Definition of control samples for high mass validation region

$\geq$ 1 b-tag @ 0.7 OP	QCR1H	VR1H
0 b-tag @ 0.7 OP	QCR2H	QCR4H
	$E_{\mathrm{T}}^{\mathrm{miss}} < 150$ GeV	150 GeV $< E_{\mathrm{T}}^{\mathrm{miss}} < 200$ GeV

$$N_{\mathrm{SR}}^{\mathrm{Pred}} = \left(N_{\mathrm{QCR3}}^{\mathrm{Data}} - N_{\mathrm{QCR3}}^{\mathrm{MC,Non-QCD}}\right) \times \left[\frac{N_{\mathrm{QCR1}}}{N_{\mathrm{QCR2}}}\right] \tag{10.10}$$

In order to check the effectiveness and accuracy of this method, the calculations were done in validation regions that have $E_{\mathrm{T}}^{\mathrm{miss}}$ between the values used for the signal region calculation. The regions used for validation are described by Tables 10.22 and 10.23, and the calculation is described by Equation 10.11.

$$N_{\mathrm{VR1}}^{\mathrm{Pred}} = \left(N_{\mathrm{QCR4}}^{\mathrm{Data}} - N_{\mathrm{QCR4}}^{\mathrm{MC,Non-QCD}}\right) \times \left[\frac{N_{\mathrm{QCR1}}}{N_{\mathrm{QCR2}}}\right] \tag{10.11}$$

In order to use the ABCD method, it is important that the variables inverted be uncorrelated so that no bias is introduced. The plots in Figure 10.13 show the $E_{\mathrm{T}}^{\mathrm{miss}}$ in the tagged and untagged region of the γ+jet MC sample for each analysis. There is an obvious correlation in both histograms. The $E_{\mathrm{T}}^{\mathrm{miss}}$ has a larger tail in the tagged region than in the untagged region, which, if ignored, would result in an underestimate of the QCD background. To compensate for this correlation, data events in QCR2, QCR3, and QCR4 are weighted bin-by-bin in $E_{\mathrm{T}}^{\mathrm{miss}}$ by the ratio of events in the 2-tag (1-tag) region compared to the 1-tag (0-tag) region in the γ+jet MC sample for the low mass (high mass) analysis.

This can be described by the following equation, for each $E_{\mathrm{T}}^{\mathrm{miss}}$ bin i:

$$N_i^{\text{no tag,corr}} = \left(N_i^{\text{no tag,uncorr}}\right) \times \left[\frac{N_i^{\mathrm{MC,no\ tag}}}{N_i^{\mathrm{MC,tag}}} \times \frac{N^{\mathrm{MC,tag}}}{N^{\mathrm{MC,no\ tag}}}\right] \tag{10.12}$$

In Equation 10.12, 'tag' means the tagging required for the signal region (2 tags for low mass region, and 1 tag for high mass region), and 'no tag' means the tagging in the control regions (1 tag for low mass region and 0 tag for high mass region).

The $E_{\mathrm{T}}^{\mathrm{miss}}$ dependent correction factors are shown in Tables 10.24 and 10.25. These correction factors are calculated in regions that do not have the $\Delta\phi_{\mathrm{min}}$ cut applied in order to increase statistics. Interestingly, although the high mass correction factor is near 2 for $E_{\mathrm{T}}^{\mathrm{miss}}$ between 100 and 200 GeV, it is almost exactly 1 in the region with $E_{\mathrm{T}}^{\mathrm{miss}} > 200$ GeV. It is hypothesized that this may be because heavy flavor decays can often produce a moderate amount of $E_{\mathrm{T}}^{\mathrm{miss}}$between 50 and 200 GeV, but very high $E_{\mathrm{T}}^{\mathrm{miss}}$ values are typically due to mismeasured jets. However, due to this background being extremely small, this effect was not investigated further.

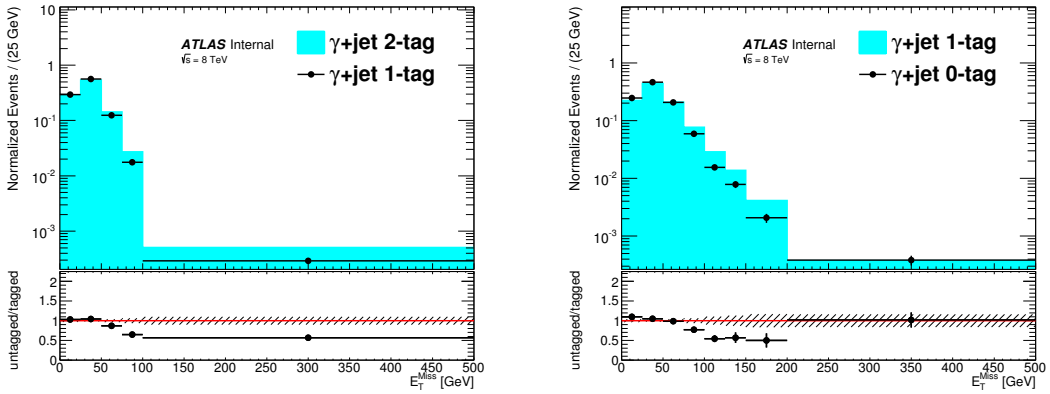

Figure 10.13: The $E_{\mathrm{T}}^{\mathrm{miss}}$ distributions for the tagged and untagged regions are plotted for the low mass region (left) and the high mass region (right). The histograms are normalized to unity. Both plots show a significant deviation between the two samples at higher $E_{\mathrm{T}}^{\mathrm{miss}}$.

Table 10.24: QCD low mass region scale factor corrections. No $\Delta\phi_{\mathrm{min}}$ cut is applied in the regions used to calculate the correction factors in order to increase statistics.

	Correction factor
0 GeV $< E_{\mathrm{T}}^{\mathrm{miss}} <$ 25 GeV	0.98 ± 0.03
25 GeV $< E_{\mathrm{T}}^{\mathrm{miss}} <$ 50 GeV	0.97 ± 0.02
50 GeV $< E_{\mathrm{T}}^{\mathrm{miss}} <$ 75 GeV	1.17 ± 0.05
75 GeV $< E_{\mathrm{T}}^{\mathrm{miss}} <$ 100 GeV	1.56 ± 0.11
100 GeV $< E_{\mathrm{T}}^{\mathrm{miss}}$	1.78 ± 0.20

Table 10.25: QCD high mass region scale factor corrections. No $\Delta\phi_{\text{min}}$ cut is applied in the regions used to calculate the correction factors in order to increase statistics.

	Correction factor
0 GeV $< E_{\text{T}}^{\text{miss}} <$ 25 GeV	0.92 ± 0.04
25 GeV $< E_{\text{T}}^{\text{miss}} <$ 50 GeV	0.96 ± 0.03
50 GeV $< E_{\text{T}}^{\text{miss}} <$ 75 GeV	1.02 ± 0.04
75 GeV $< E_{\text{T}}^{\text{miss}} <$ 100 GeV	1.30 ± 0.10
100 GeV $< E_{\text{T}}^{\text{miss}} <$ 125 GeV	1.86 ± 0.25
125 GeV $< E_{\text{T}}^{\text{miss}} <$ 150 GeV	1.77 ± 0.33
150 GeV $< E_{\text{T}}^{\text{miss}} <$ 200 GeV	2.01 ± 0.49
200 GeV $< E_{\text{T}}^{\text{miss}}$	0.99 ± 0.25

The results for each signal region are shown in Table 10.26, with and without the correction factor applied. The result for the high mass region is actually slightly negative due to the subtraction of non-QCD MC, but it is consistent with 0. With the correction factor uncertainty and theory systematics (shown in Appendix C) included, the final results are 2.24 ± 1.51 (stat.) ± 1.47 (syst.) for the low mass region and -.19 ± 0.59 (stat.) ± 0.27 (syst.) for the high mass region. The result for the high mass region is truncated to 0, since the number of events cannot be negative.

Table 10.26: QCD signal region predictions with statistical uncertainties. Results are shown with and without the correction factor applied.

	Low Mass	Corr. Low Mass	High Mass	Corr. High Mass
N_{CR1}	1661 ± 41	1661 ± 41	610 ± 25	610 ± 25
$N_{\text{CR1}}^{\text{MC,Non-QCD}}$	18.64 ± 0.77	18.64 ± 0.77	15.78 ± 0.89	15.78 ± 0.89
N_{CR2}	16420 ± 130	16370 ± 160	1992 ± 45	1975 ± 47
$N_{\text{CR2}}^{\text{MC,Non-QCD}}$	91.7 ± 2.6	96.5 ± 2.7	16.2 ± 1.0	20.2 ± 1.3
Scale Factor $\frac{N_{\text{CR1}}}{N_{\text{CR2}}}$	0.101 ± 0.003	0.101 ± 0.003	0.30 ± 0.01	0.30 ± 0.01
$N_{\text{CR3}}^{\text{Data}}$	70.0 ± 8.4	124 ± 15	4.0 ± 2.0	3.9 ± 2.0
$N_{\text{CR3}}^{\text{MC,Non-QCD}}$	57.5 ± 1.4	102.2 ± 3.1	4.64 ± 0.44	4.58 ± 0.46
$N_{\text{CR3}}^{\text{Data}} - N_{\text{CR3}}^{\text{MC,Non-QCD}}$	12.5 ± 8.5	22 ± 16	-0.6 ± 2.0	-0.6 ± 2.1
$N_{\text{SR}}^{\text{Pred}}$	1.26 ± 0.85	2.2 ± 1.6	-0.19 ± 0.62	-0.19 ± 0.63

10.1.5 $Z \to \nu\nu$ background

Events with $E_{\mathrm{T}}^{\mathrm{miss}}$ resulting from Z$\to \nu\nu$ decays cannot be estimated using techniques from the previous sections, so must be estimated in a different way. Events with Z$\to \nu\nu$ produced with a photon and a b-jet are rare, but also nearly indistinguishable from signal events. For this reason, the estimation is done from Monte Carlo simulation.

The largest contribution for each signal region comes from the Sherpa Z($\to \nu\nu$)+γ dataset with DSID 126022. In the low mass region, it contributes 0.73 $\pm$ 0.06 events. In the high mass region, it contributes 0.29 $\pm$ 0.04 events. There is no additional contribution from Z($\to \nu\nu$)+jets in the high mass region, but there is an additional 0.03 $\pm$ 0.02 events in the low mass region from Z+jets. There are no scale variation samples available to test the theoretical uncertainties, so a conservative 50 % uncertainty is applied. This has very little effect on the outcome of the analysis because it is such a small background. The total Z$\to \nu\nu$ background estimate including systematics is 0.76 $\pm$ 0.38 (syst.) events in the low mass region and 0.29 $\pm$ 0.15 (syst.) events in the high mass region.

10.1.6 Total backgrounds

The background predictions modeled in Section 10.1 for SRL and SRH are summarized in Table 10.27. The backgrounds are broken into four separate contributions, from events with electrons faking photons, events with leptons that have prompt photons or jets faking photons, events with fake $E_{\mathrm{T}}^{\mathrm{miss}}$, and events with $E_{\mathrm{T}}^{\mathrm{miss}}$ from

$Z \to \nu\nu$.

Table 10.27: Background predictions for the signal regions.

	e$\to \gamma$	Lepton	QCD	Z$\to \nu\nu$	Total Bkg.
SRL	3.21 $\pm$ 0.42	12.6 $\pm$ 4.9	2.3 $\pm$ 2.1	0.76 $\pm$ 0.38	18.8 $\pm$ 5.3
SRH	0.18 $\pm$ 0.08	3.35 $\pm$ 1.05	0 $\pm$ 0.65	0.29 $\pm$ 0.15	3.82 $\pm$ 1.25

10.2 Validation Regions

In order to test the background estimation techniques, four validation regions are defined for each signal region. For each signal region, there is a validation region that uses an $E_{\mathrm{T}}^{\mathrm{miss}}$ sideband region, one that reverses the M_{T} cut, and one that reverses the $\Delta\phi_{\mathrm{min}}(E_{\mathrm{T}}^{\mathrm{miss}},$ jet) cut. Additionally, there is a validation region for the low mass region that inverts the $M_{b\bar{b}}$ cut, and a validation region for the high mass region that uses an H_{T} sideband.

The cuts for the low mass regions are summarized in Table 10.28. The results are summarized in Table 10.29. There are some discrepancies between the predicted and observed values, but no region has a discrepancy over 2σ. Plots of the variables $E_{\mathrm{T}}^{\mathrm{miss}}$, $M_{b\bar{b}}$, M_{T}, and $\Delta\phi_{\mathrm{min}}$ are shown for each of the four low mass validation regions in Figures 10.14-10.17. Each variable is shown without any cut on that variable, but with cuts on each of the other variables.

Table 10.28: Cuts used for the low mass signal region and validation regions.

Cut	SRL	VRL1 $E_{\mathrm{T}}^{\mathrm{miss}}$	VRL2 $M_{b\bar{b}}$	VRL3 M_{T}	VRL4 $\Delta\phi_{\mathrm{min}}$
p_T^{γ} [GeV]	> 125	> 125	> 125	> 125	> 125
N_{jets}	$\geq 2, \leq 4$	$\geq 2, \leq 4$	$\geq 2, \leq 4$	$\geq 2, \leq 4$	$\geq 2, \leq 4$
N_{bjets}	≥ 2	≥ 2	≥ 2	≥ 2	≥ 2
N_{leps}	0	0	0	0	0
$E_{\mathrm{T}}^{\mathrm{miss}}$ [GeV]	> 100	**[75, 100]**	> 100	> 100	> 100
M_{T} [GeV]	> 90	> 90	> 90	$<$ **90**	> 90
$\Delta\phi_{\mathrm{min}}(E_{\mathrm{T}}^{\mathrm{miss}}, \mathrm{j}_{1,2})$	> 0.3	> 0.3	> 0.3	> 0.3	$<$ **0.3**
$M_{b\bar{b}}$ [GeV]	[75, 150]	[75, 150]	$<$ **75 or** $>$ **150**	[75, 150]	[75, 150]

Table 10.29: Background estimation and results for the low mass signal and validation regions.

	e$\rightarrow \gamma$	Lepton	QCD	Z$\rightarrow \nu\nu$	Total Bkg.	Obs. Events
SRL	3.21 ± 0.42	12.6 ± 4.9	2.3 ± 2.1	0.76 ± 0.38	18.8 ± 5.3	
VRL1 – $E_{\mathrm{T}}^{\mathrm{miss}}$	2.45 ± 0.23	5.1 ± 1.5	25.4 ± 3.0	0.14 ± 0.02	33.2 ± 3.3	35
VRL2 – $M_{b\bar{b}}$	5.90 ± 0.35	21.6 ± 6.0	5.9 ± 2.4	1.58 ± 0.08	35.0 ± 6.5	36
VRL3 – M_{T}	2.80 ± 0.23	4.2 ± 3.0	1.44 ± 0.96	0.04 ± 0.01	8.5 ± 3.2	4
VRL4 – $\Delta\phi_{\mathrm{min}}$	0.76 ± 0.14	3.6 ± 1.9	9.3 ± 1.9	0.09 ± 0.02	13.8 ± 2.7	15

The cuts for the high mass regions are summarized in Table 10.30. The results are summarized in Table 10.31. There are some discrepancies between the predicted and observed values, but no region has a discrepancy much over 1σ. Plots of the variables $E_{\mathrm{T}}^{\mathrm{miss}}$, $M_{b\bar{b}}$, M_{T}, and $\Delta\phi_{\mathrm{min}}$ are shown for each of the four high mass validation regions in Figures 10.18-10.21.

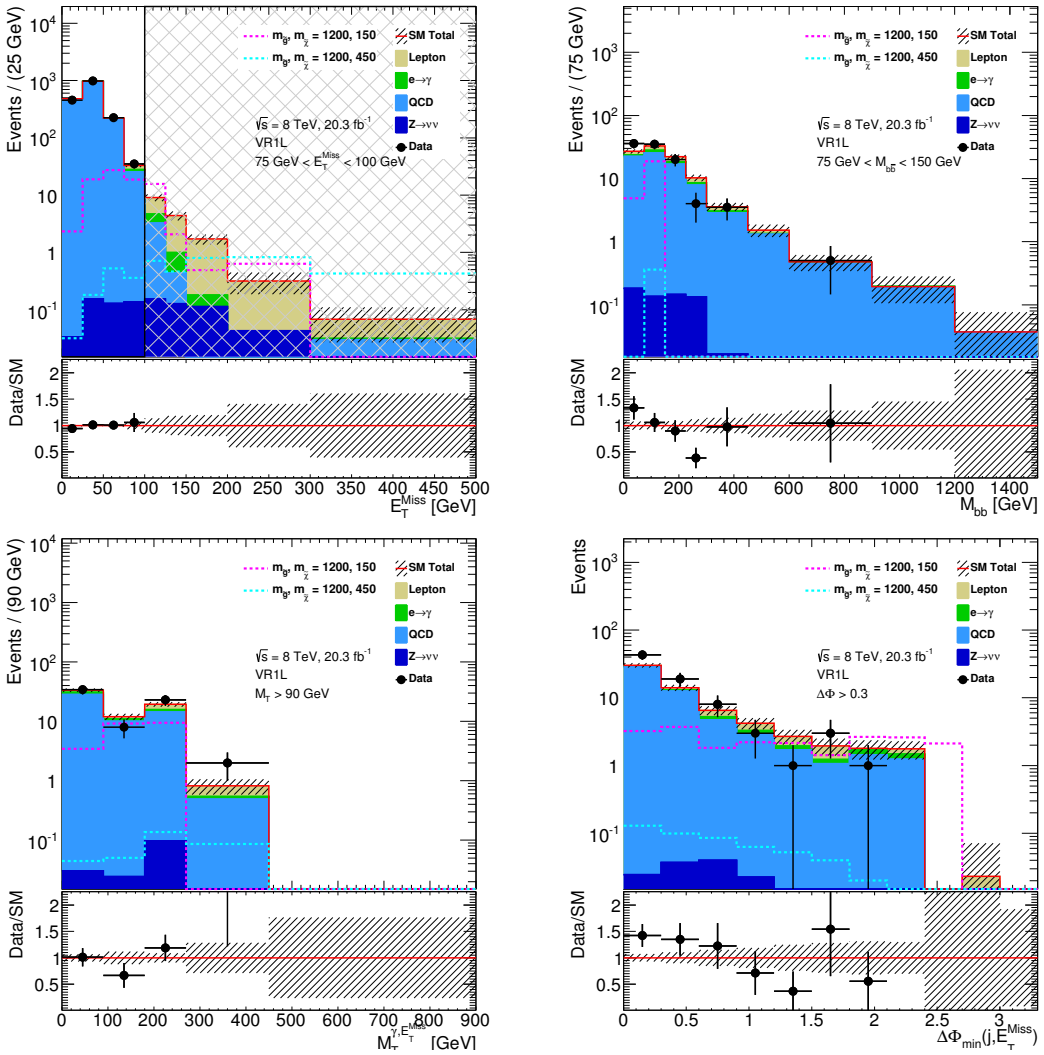

Figure 10.14: Predicted SM backgrounds and observed events for the low mass $E_{\mathrm{T}}^{\mathrm{miss}}$ validation region in $E_{\mathrm{T}}^{\mathrm{miss}}$ (upper left), $M_{b\bar{b}}$ (upper right), M_{T} (lower left), and $\Delta\phi_{\mathrm{min}}$ (lower right). The region with $E_{\mathrm{T}}^{\mathrm{miss}} > 100$ GeV is the signal region, and therefore blinded. Each variable is shown over its full range without the cut on that variable that defines the validation region. In this validation region, the cuts on these four variables are 75 GeV $< E_{\mathrm{T}}^{\mathrm{miss}} < 100$ GeV, 75 GeV $< M_{b\bar{b}} < 150$ GeV, $M_{\mathrm{T}} > 90$ GeV, and $\Delta\phi_{\mathrm{min}} > 0.3$.

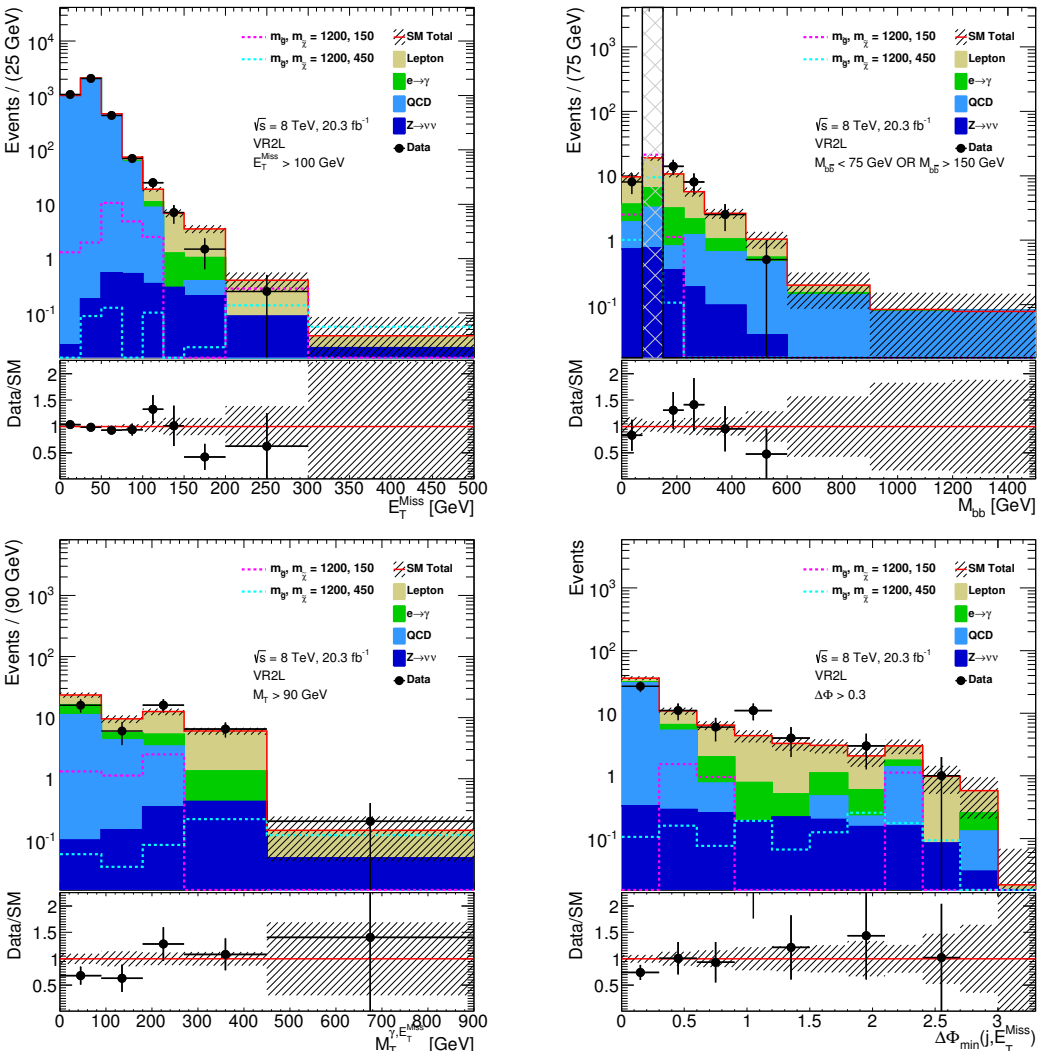

Figure 10.15: Predicted SM backgrounds and observed events for the low mass $M_{b\bar{b}}$ validation region in $E_{\mathrm{T}}^{\mathrm{miss}}$ (upper left), $M_{b\bar{b}}$ (upper right), M_{T} (lower left), and $\Delta\phi_{\mathrm{min}}$ (lower right). The region with 75 GeV $< M_{b\bar{b}} <$ 150 GeV is the signal region, and therefore blinded. Each variable is shown over its full range without the cut on that variable that defines the validation region. In this validation region, the cuts on these four variables are $E_{\mathrm{T}}^{\mathrm{miss}} > 100$ GeV, $M_{b\bar{b}} < 75$ GeV or $M_{b\bar{b}} > 150$ GeV, $M_{\mathrm{T}} > 90$ GeV, and $\Delta\phi_{\mathrm{min}} > 0.3$.

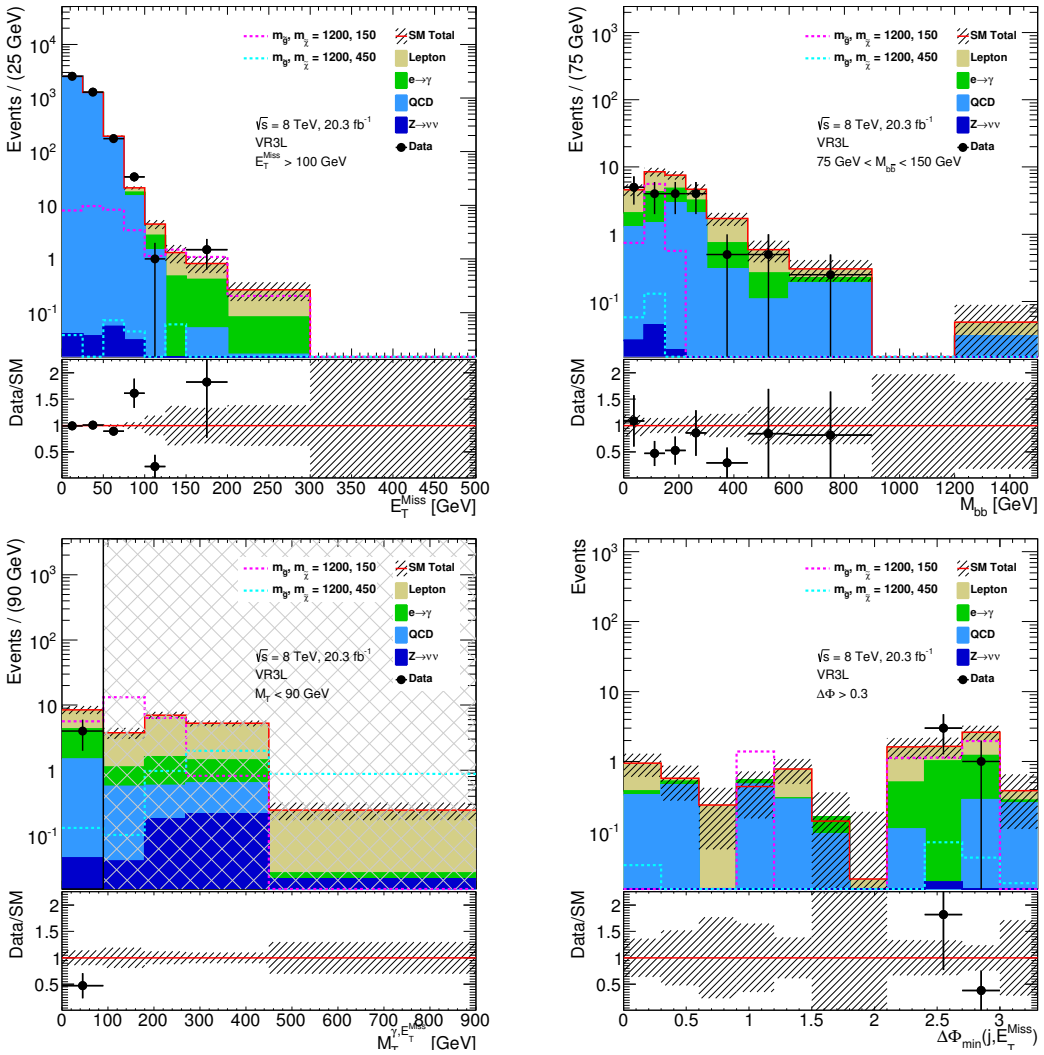

Figure 10.16: Predicted SM backgrounds and observed events for the low mass M_{T} validation region in $E_{\mathrm{T}}^{\mathrm{miss}}$ (upper left), $M_{b\bar{b}}$ (upper right), M_{T} (lower left), and $\Delta\phi_{\mathrm{min}}$ (lower right). The region with $M_{\mathrm{T}} > 90$ GeV is the signal region, and therefore blinded. Each variable is shown over its full range without the cut on that variable that defines the validation region. In this validation region, the cuts on these four variables are $E_{\mathrm{T}}^{\mathrm{miss}} > 100$ GeV, 75 GeV $< M_{b\bar{b}} <$ 150 GeV, $M_{\mathrm{T}} < 90$ GeV, and $\Delta\phi_{\mathrm{min}} > 0.3$.

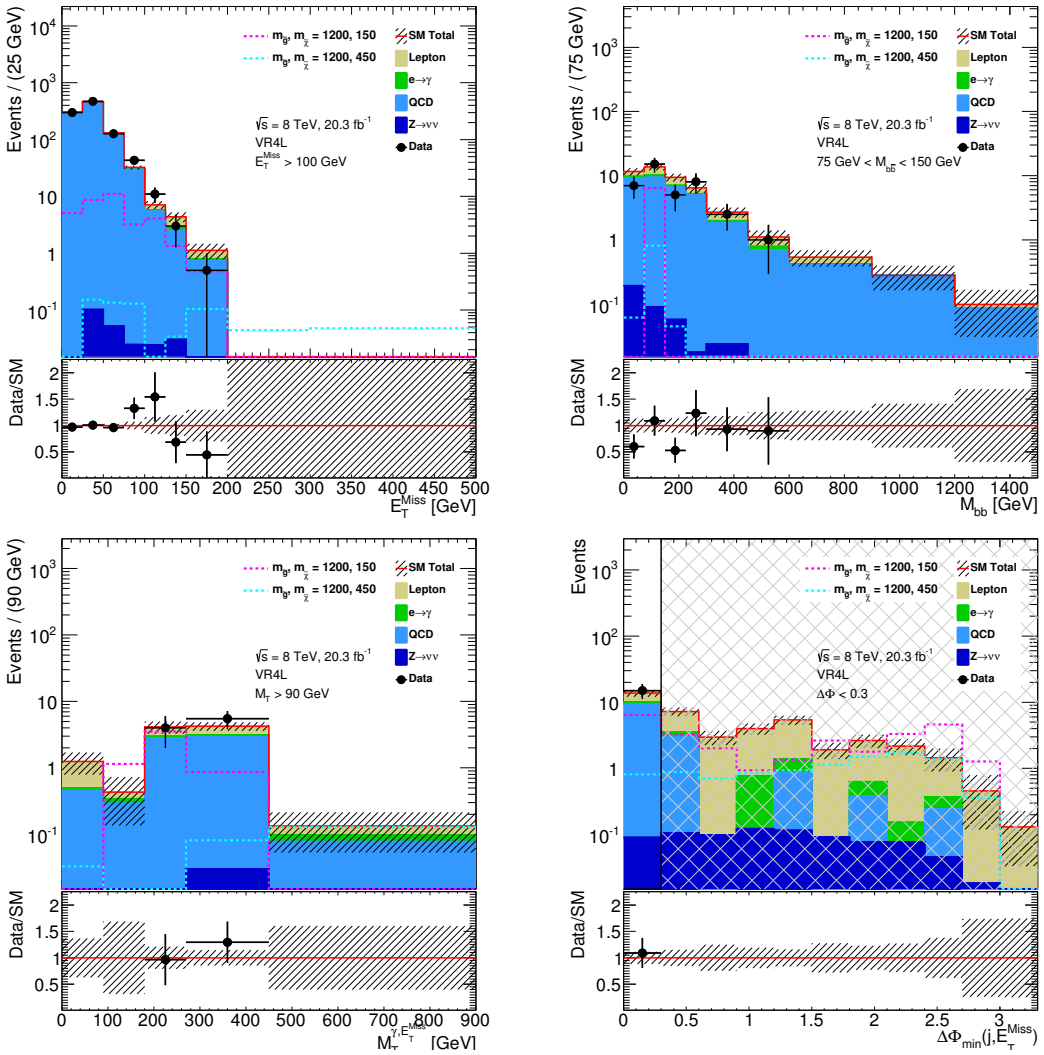

Figure 10.17: Predicted SM backgrounds and observed events for the low mass $\Delta\phi_{\text{min}}$ validation region in $E_{\text{T}}^{\text{miss}}$ (upper left), $M_{b\bar{b}}$ (upper right), M_{T} (lower left), and $\Delta\phi_{\text{min}}$ (lower right). The region with $\Delta\phi_{\text{min}} > 0.3$ is the signal region, and therefore blinded. Each variable is shown over its full range without the cut on that variable that defines the validation region. In this validation region, the cuts on these four variables are $E_{\text{T}}^{\text{miss}} > 100$ GeV, 75 GeV $< M_{b\bar{b}} <$ 150 GeV, $M_{\text{T}} > 90$ GeV, and $\Delta\phi_{\text{min}} < 0.3$.

Table 10.30: Cuts used for the high mass signal region and validation regions.

Cut	SRH	VRH1 $E_{\mathrm{T}}^{\mathrm{miss}}$	VRH2 H_{T}	VRH3 M_{T}	VRH4 $\Delta\phi_{\mathrm{min}}$
p_T^{γ} [GeV]	> 150	> 150	> 150	> 150	> 150
N_{jets}	≥ 4	≥ 4	≥ 4	≥ 4	≥ 4
N_{bjets}	≥ 1	≥ 1	≥ 1	≥ 1	≥ 1
$E_{\mathrm{T}}^{\mathrm{miss}}$ [GeV]	> 200	**[150, 200]**	> 200	> 200	> 200
M_{T} [GeV]	> 90	> 90	> 90	$<$ **90**	> 90
$\Delta\phi_{\mathrm{min}}(E_{\mathrm{T}}^{\mathrm{miss}}, \mathrm{j}_{1\ldots4})$	> 0.3	> 0.3	> 0.3	> 0.3	$<$ **0.3**
H_{T} [GeV]	> 1000	> 1000	**[500, 1000]**	> 1000	> 1000

Table 10.31: Background estimation and results for the high mass signal and validation regions.

	e$\rightarrow\gamma$	Lepton	QCD	Z$\rightarrow\nu\nu$	Total Bkg.	Obs. Events
SRH	0.18 ± 0.08	3.35 ± 1.05	-0.19 ± 0.65	0.29 ± 0.15	3.63 ± 1.25	
VRH1 – $E_{\mathrm{T}}^{\mathrm{miss}}$	0.27 ± 0.07	1.65 ± 0.35	3.4 ± 2.0	0.09 ± 0.02	5.4 ± 2.0	6
VRH2 – H_{T}	1.33 ± 0.16	12.3 ± 1.8	3.3 ± 2.0	1.37 ± 0.08	18.3 ± 2.7	15
VRH3 – M_{T}	1.08 ± 0.13	2.14 ± 0.64	-0.01 ± 0.65	0.024 ± 0.010	3.24 ± 0.92	2
VRH4 – $\Delta\phi_{\mathrm{min}}$	0.21 ± 0.06	1.94 ± 0.48	2.6 ± 1.2	0.14 ± 0.03	4.9 ± 1.3	4

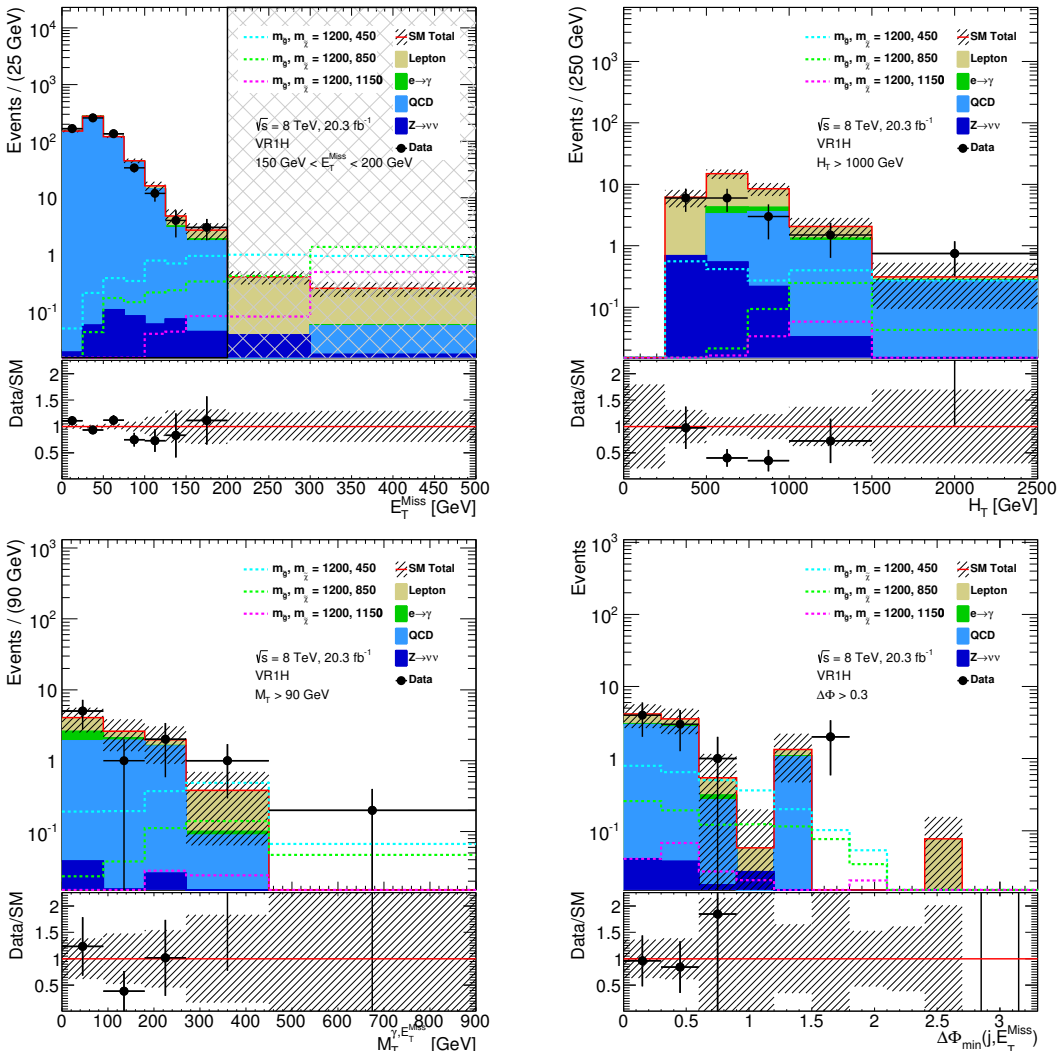

Figure 10.18: Predicted SM backgrounds and observed events for the high mass $E_{\mathrm{T}}^{\mathrm{miss}}$ validation region in $E_{\mathrm{T}}^{\mathrm{miss}}$ (upper left), H_{T} (upper right), M_{T} (lower left), and $\Delta\phi_{\mathrm{min}}$ (lower right). The region with $E_{\mathrm{T}}^{\mathrm{miss}} > 200$ GeV is the signal region, and therefore blinded. Each variable is shown over its full range without the cut on that variable that defines the validation region. In this validation region, the cuts on these four variables are 150 GeV $< E_{\mathrm{T}}^{\mathrm{miss}} < 200$ GeV, $H_{\mathrm{T}} > 1000$ GeV, $M_{\mathrm{T}} > 90$ GeV, and $\Delta\phi_{\mathrm{min}} > 0.3$.

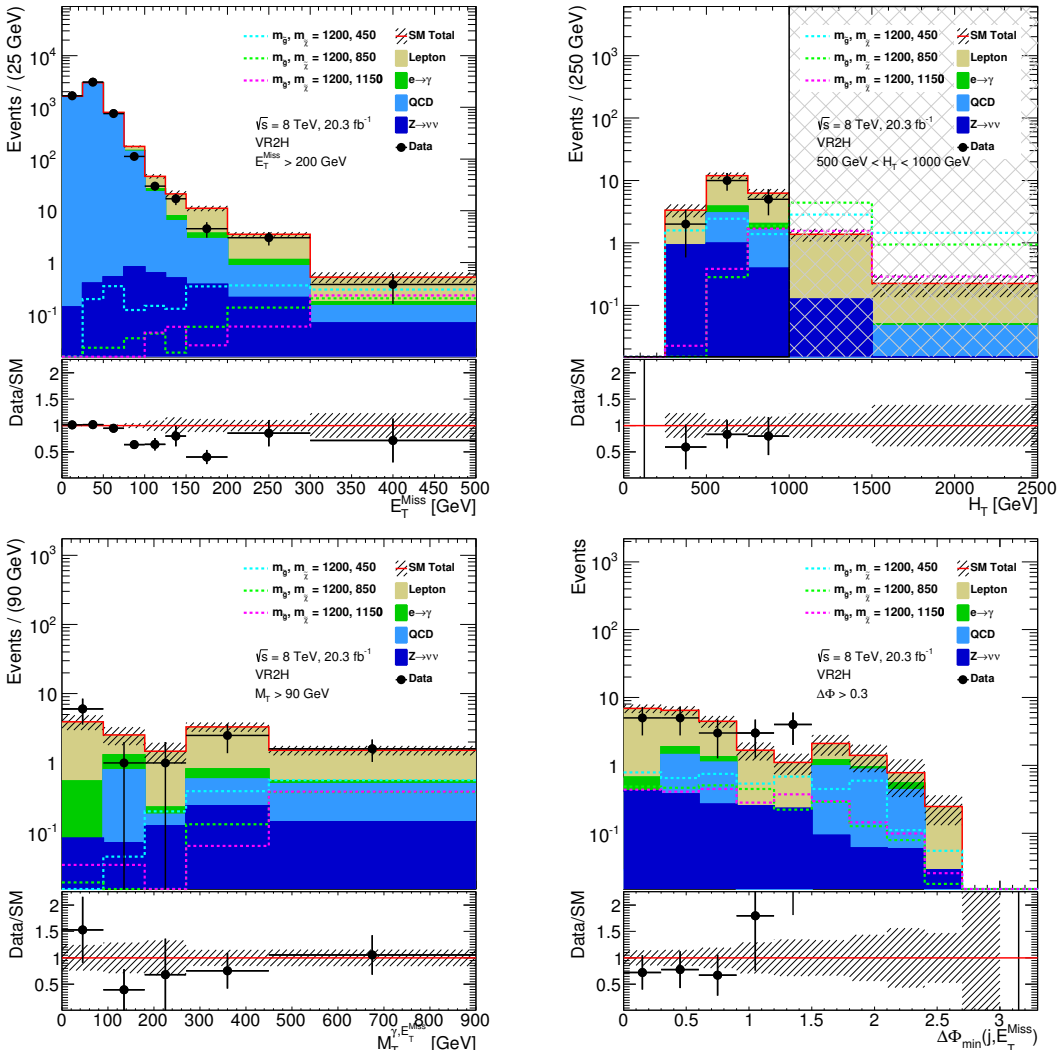

Figure 10.19: Predicted SM backgrounds and observed events for the high mass H_{T} validation region in $E_{\mathrm{T}}^{\mathrm{miss}}$ (upper left), H_{T} (upper right), M_{T} (lower left), and $\Delta\phi_{\mathrm{min}}$ (lower right). The region with $H_{\mathrm{T}} > 1000$ GeV is the signal region, and therefore blinded. Each variable is shown over its full range without the cut on that variable that defines the validation region. In this validation region, the cuts on these four variables are $E_{\mathrm{T}}^{\mathrm{miss}} > 200$ GeV, 500 GeV $< H_{\mathrm{T}} < 1000$ GeV, $M_{\mathrm{T}} > 90$ GeV, and $\Delta\phi_{\mathrm{min}} > 0.3$.

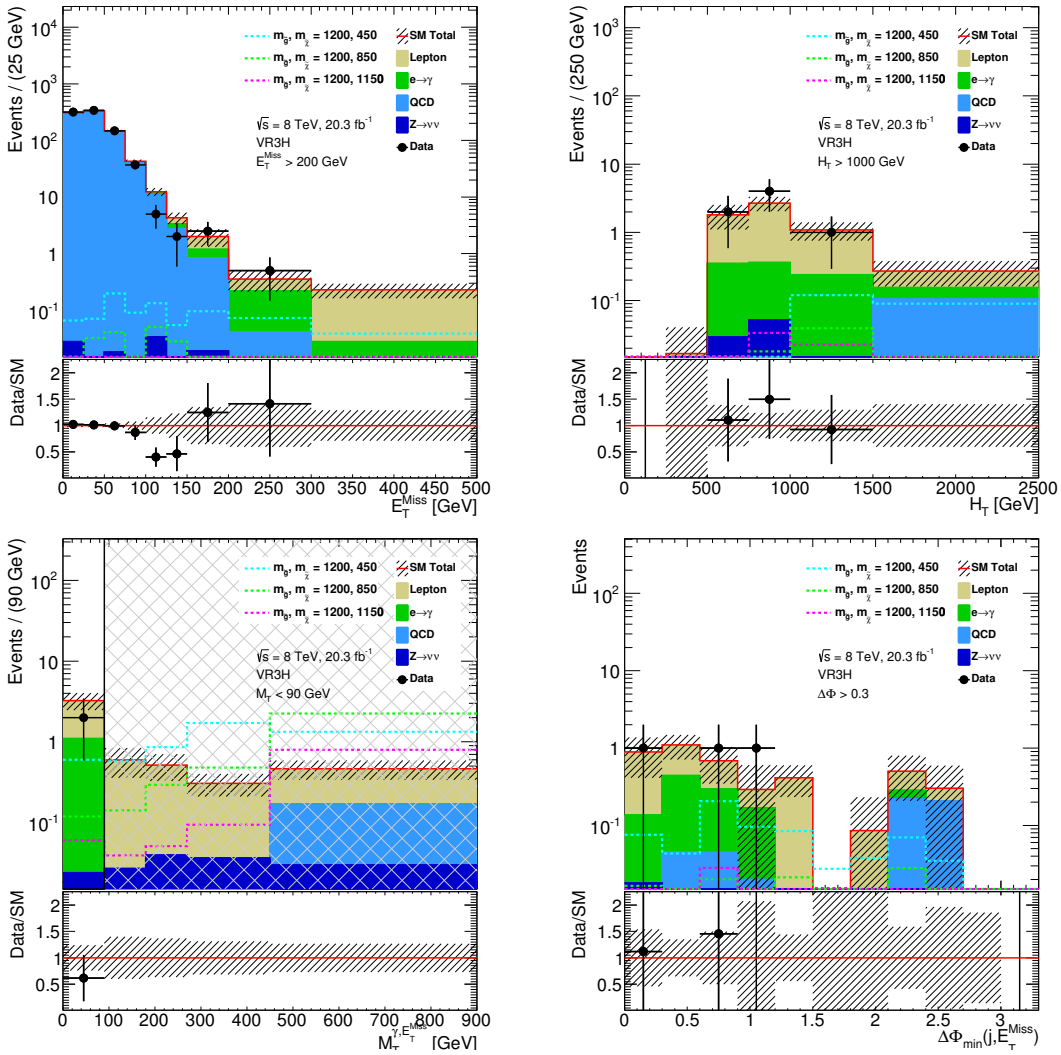

Figure 10.20: Predicted SM backgrounds and observed events for the high mass M_{T} validation region in $E_{\mathrm{T}}^{\mathrm{miss}}$ (upper left), H_{T} (upper right), M_{T} (lower left), and $\Delta\phi_{\mathrm{min}}$ (lower right). The region with $M_{\mathrm{T}} > 90$ GeV is the signal region, and therefore blinded. Each variable is shown over its full range without the cut on that variable that defines the validation region. In this validation region, the cuts on these four variables are $E_{\mathrm{T}}^{\mathrm{miss}} > 200$ GeV, $H_{\mathrm{T}} > 1000$ GeV, $M_{\mathrm{T}} < 90$ GeV, and $\Delta\phi_{\mathrm{min}} > 0.3$.

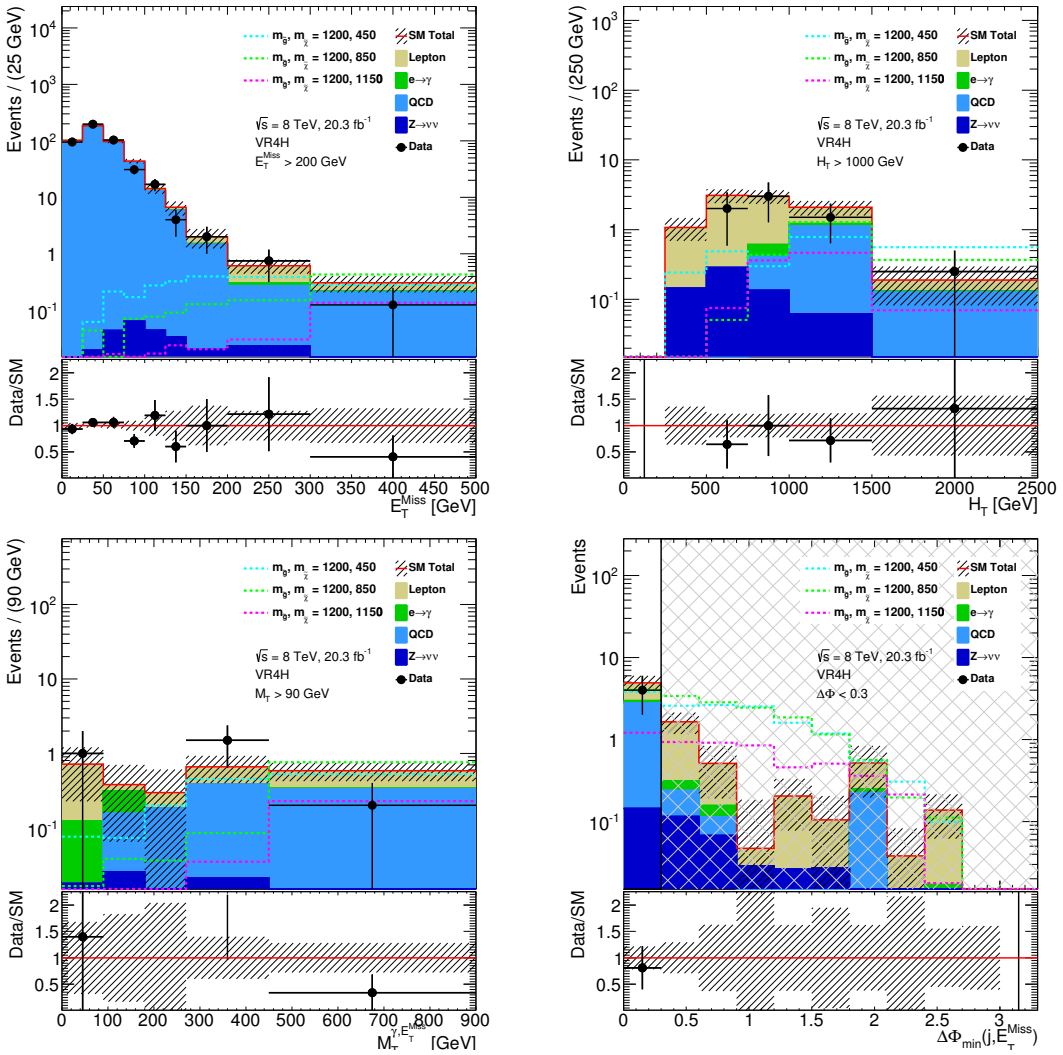

Figure 10.21: Predicted SM backgrounds and observed events for the high mass $\Delta\phi_{\text{min}}$ validation region in $E_{\text{T}}^{\text{miss}}$ (upper left), H_{T} (upper right), M_{T} (lower left), and $\Delta\phi_{\text{min}}$ (lower right). The region with $\Delta\phi_{\text{min}} > 0.3$ is the signal region, and therefore blinded.Each variable is shown over its full range without the cut on that variable that defines the validation region. In this validation region, the cuts on these four variables are $E_{\text{T}}^{\text{miss}} > 200$ GeV, $H_{\text{T}} > 1000$ GeV, $M_{\text{T}} > 90$ GeV, and $\Delta\phi_{\text{min}} < 0.3$.

Chapter 11

Systematic Uncertainties

This section discusses the experimental and theoretical uncertainties associated with the signal and background Monte Carlo used in this analysis. Experimental uncertainties are discussed in Section 11.1. Theoretical uncertainties are discussed in Section 11.2.

11.1 Experimental Uncertainties

In the following, a description of the procedures to evaluate experimental uncertainties is discussed. The tools are implemented using the SUSYTools package (version 00-03-24-02). The systematic uncertainties on the data-driven estimates have been discussed in previous sections.

Pileup uncertainty

The uncertainty on the pileup scale factor is determined by changing the average number of interactions per crossing, μ, by $\pm 10\%$.

Luminosity uncertainty

The uncertainty on the integrated luminosity is ±2.8%. It is derived, following the same methodology as that detailed in Ref. [69], from a preliminary calibration of the luminosity scale derived from beam-separation scans performed in November 2012.

Photon identification, energy scale and resolution

The uncertainty on the photon scale factors applied to MC is propagated through the analysis, as in Ref. [70]. The scale factors take into account various data-driven measurements. The central values and uncertainties are provided by the Egamma combined performance working group. However, the isolation requirement applied to derive the scale factors (topoEtcone40 < 4 GeV) is different from the requirement used for this analysis. To account for this, the tight identification efficiency was evaluated after each isolation criteria for photons with $p_{\mathrm{T}} > 125$ GeV in both signal and γ+jets MC. The effect is found to be very small ($< 1\%$), so it is neglected. Uncertainties on the photon energy scale and resolution are also applied, as described in Ref. [71].

Lepton identification, energy scale and resolution

Similar to photons, the uncertainty on the identification efficiency, energy scale and resolution are considered, following Ref. [72], [71], and [73].

Jet energy scale

The jet energy scale is varied using the recommendations of the Jet/$E_{\mathrm{T}}^{\mathrm{miss}}$ combined performance group, as described in Ref. [74].

Jet energy resolution

An additional jet smearing is applied to MC based on the p_{T} and η of the jet to account for a possible underestimate of the jet energy resolution, as described in Ref. [74].

$E_{\mathrm{T}}^{\mathrm{miss}}$ soft terms

The impact of the scale uncertainties on the $E_{\mathrm{T}}^{\mathrm{miss}}$ soft terms is estimated by varying these scales up and down. The resolution of the soft terms is also varied, as described in [75].

b-tagging efficiency

The uncertainty on the b-tagging efficiency in MC is estimated using the techniques discussed in Ref. [76]. A scale factor is calculated for each jet based on the p_{T}, η, and flavor of the jet. This scale factor is varied to reflect the uncertainty on the measured tagging efficiency and mistag rate. It is varied separately for B-jets, C-jets and light jets, leading to three uncorrelated systematic uncertainties.

11.1.1 Experimental signal uncertainties

Table 11.1 shows the experimental systematic uncertainties on the signal efficiency. The largest uncertainties are due to photon identification, jet energy resolution, jet energy scale, $E_{\mathrm{T}}^{\mathrm{miss}}$ soft terms, and b-tagging. These uncertainties are shown for each gluino grid point in Figures 11.1, 11.2, 11.3, 11.4, and 11.5.

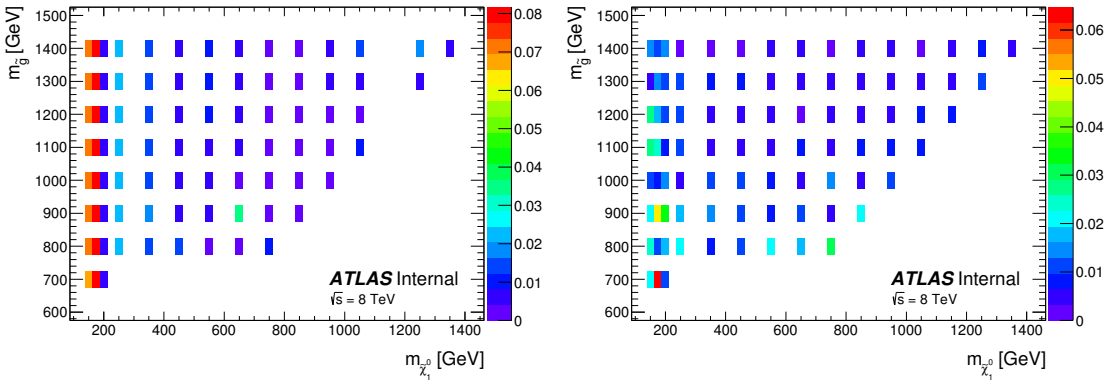

Figure 11.1: The photon identification uncertainty as a fraction of the nominal yield in the gluino-neutralino plane for the low mass signal region (left) and the high mass signal region.

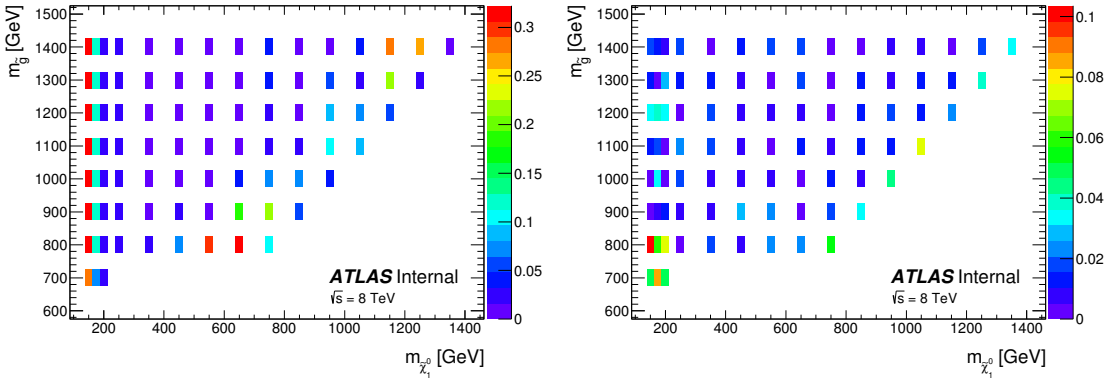

Figure 11.2: The jet energy resolution uncertainty as a fraction of the nominal yield in the gluino-neutralino plane for the low mass signal region (left) and the high mass signal region.

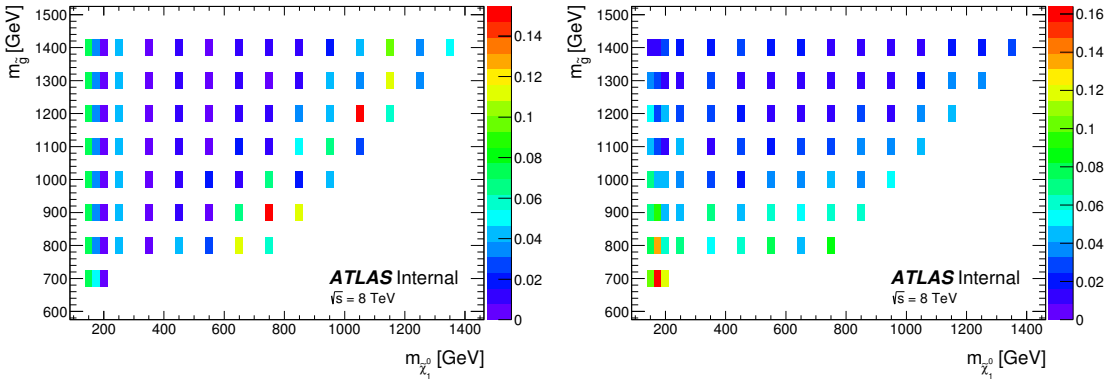

Figure 11.3: The jet energy scale uncertainty as a fraction of the nominal yield in the gluino-neutralino plane for the low mass signal region (left) and the high mass signal region.

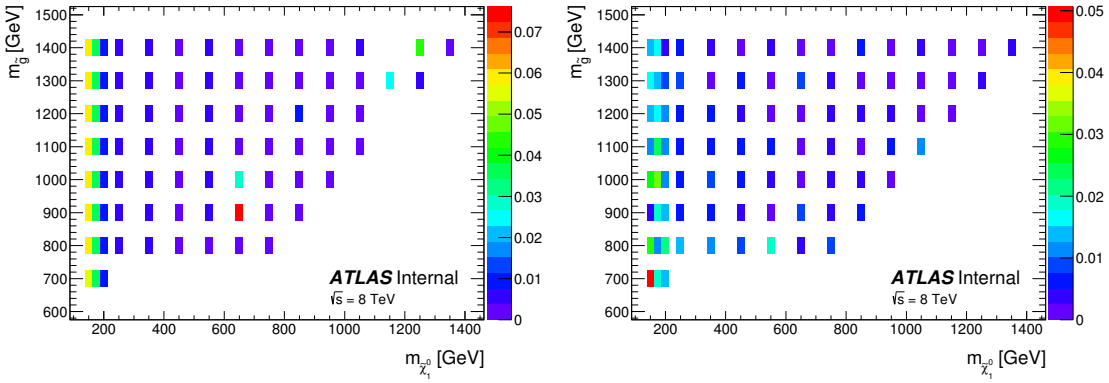

Figure 11.4: The $E_{\mathrm{T}}^{\mathrm{miss}}$ soft terms uncertainty as a fraction of the nominal yield in the gluino-neutralino plane for the low mass signal region (left) and the high mass signal region .

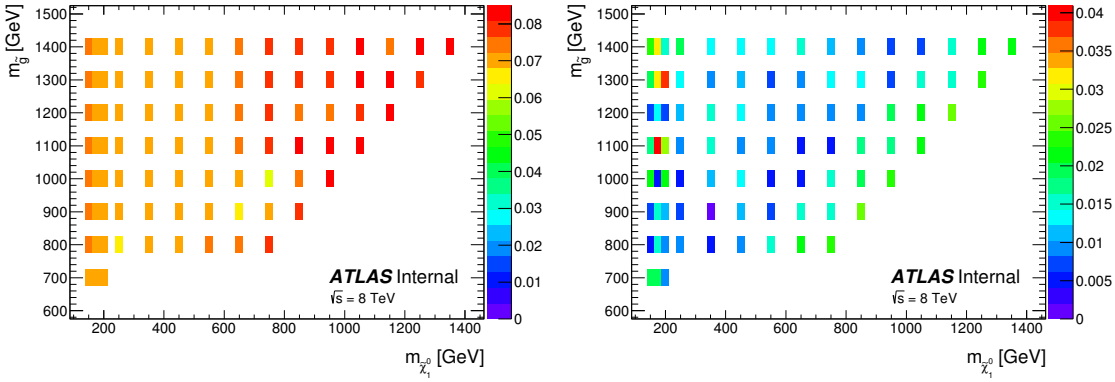

Figure 11.5: The b-tagging uncertainty as a fraction of the nominal yield in the gluino-neutralino plane for the low mass signal region (left) and the high mass signal region.

Table 11.1: Systematic errors for signal efficiency in the gluino grid.

	SRL Uncertainty	SRH Uncertainty
Pileup	0-3%	0-3%
Photon ID	0-8%	0-7%
Electron ID	<1%	<2%
Muon ID	<1%	<1%
Jet Energy Resolution	1-32%	0-10%
Jet Energy Scale	1-15%	1-16%
$E_{\mathrm{T}}^{\mathrm{miss}}$ Soft Terms	0-8%	0-5%
B-tagging	6-9%	1-4%
JVF	0-5%	<1%

11.1.2 Experimental background uncertainties

Table 11.2 shows the systematic uncertainties due to the use of Monte Carlo in the background calculations. For the low mass signal region, the systematic error is dominated by the JES uncertainty. For the high mass signal region, the systematic error is dominated by JES, JER, $E_{\mathrm{T}}^{\mathrm{miss}}$ soft terms, and flavor-tagging uncertainties. None of these experimental uncertainties are comparable in magnitude to the background technique uncertainties discussed in Section 10.1, which are dominated by statistical uncertainties.

Table 11.2: Systematic errors for backgrounds.

	SRL Uncertainty	SRH Uncertainty
Pileup	0.35 %	0.43 %
Photon ID	0.58 %	1.57 %
Electron ID	0.88 %	1.43 %
Muon ID	0.17 %	0.85 %
Jet Energy Resolution	0.78 %	1.87 %
Jet Energy Scale	4.15 %	3.53 %
$E_{\mathrm{T}}^{\mathrm{miss}}$ Soft Terms	1.35 %	2.53 %
B-tagging	1.00 %	3.75 %
JVF	0.77 %	1.13 %

11.2 Theoretical Uncertainties

GGM cross section uncertainties

The standard ATLAS SUSY `SignalUncertaintiesUtils` tools are used to calculate the signal cross section uncertainties due to PDF, scale and α_s uncertainties. Because there are several strong and weak production processes for each point in the signal grid, the uncertainties must be calculated separately for each process and combined into an overall uncertainty. According to the SUSY group recommendations, only one symmetric uncertainty value should be assigned for each process, representing the combination of the PDF, scale, and α_s uncertainties.

The PDF uncertainties are calculated with the CTEQ6.6m (or MSTW) error sets, a set of 44 (40) PDF sets that represent the uncertainties of the PDF global fit. Specifically, these error sets represent the 90% CL upper and lower bound in the variation of the PDF with respect to each eigenvector of the fit. These 90% CL uncertainty bands are converted to 68% CL bands within the SUSY `SignalUncertaintiesUtils`

tool.

The scale uncertainty of the NLO calculations is evaluated by changing the renormalization and factorization scales in Prospino by a factor of 0.5 and 2.0. The resulting cross sections are compared to the result obtained at the nominal scale.

The signal cross section uncertainty resulting from α_s uncertainty is calculated by using CTEQ PDF sets with different values of α_s.

These procedures can give asymmetric uncertainties for all three uncertainty calculations. The three uncertainties are combined to derive a central value and symmetric total uncertainty according to the following:

$$CTEQ_{\mathrm{error_{up}}} = \sqrt{CTEQ^2_{\mathrm{PDF_{up}}} + CTEQ^2_{\mathrm{scale_{up}}} + \alpha^2_{s_{\mathrm{up}}}} \tag{11.1}$$

$$CTEQ_{\mathrm{error_{down}}} = \sqrt{CTEQ^2_{\mathrm{PDF_{down}}} + CTEQ^2_{\mathrm{scale_{down}}} + \alpha^2_{s_{\mathrm{down}}}} \tag{11.2}$$

$$MSTW_{\mathrm{error_{up}}} = \sqrt{MSTW^2_{\mathrm{PDF_{up}}} + MSTW^2_{\mathrm{scale_{up}}}} \tag{11.3}$$

$$MSTW_{\mathrm{error_{down}}} = \sqrt{MSTW^2_{\mathrm{PDF_{down}}} + MSTW^2_{\mathrm{scale_{down}}}} \tag{11.4}$$

$$A = \max(CTEQ + CTEQ_{\mathrm{error_{up}}}, MSTW + MSTW_{\mathrm{error_{up}}}) \tag{11.5}$$

$$B = \min(CTEQ - CTEQ_{\mathrm{error_{down}}}, MSTW - MSTW_{\mathrm{error_{down}}}) \tag{11.6}$$

The central value for the cross section is then defined to be $0.5*(A+B)$, and the symmetric total uncertainty on this cross section is defined to be $(A-B)/(A+B)$. The central cross section values and the total uncertainties are summarized in Tables 7.10 and 7.11. For gluino production, uncertainties range from 18.7% at 700 GeV to 39.0%

at 1400 GeV. For gaugino production, uncertainties range from 2.8% at 150 GeV to 10.0% at 1350 GeV.

Background Theory Uncertainties

The primary MC samples used to calculate the background are W+γ and $t\bar{t}$ +γ. Each of these samples had samples produced with scale variations that were used to measure these uncertainties. In addition, PDF uncertainties were calculated by testing three different PDFs and their accompanying error PDFs. More details on these calculations are located in Appendix C.

Chapter 12

Results and Interpretation

12.1 Summary of background predictions and observed data events

For the low mass region, 18.8 ± 3.7 (stat.) ± 3.9 (syst.) events are expected, and 12 are observed. The breakdown of the contributions to the expected background are shown in Table 12.1. Plots of the variables $E_{\mathrm{T}}^{\mathrm{miss}}$, $M_{b\bar{b}}$, M_{T}, and $\Delta\phi_{\mathrm{min}}$ are shown for the low mass signal region in Figure 12.1.

Table 12.1: Background estimation and results for the signal regions.

	e→ γ	Lepton	QCD	Z→ $\nu\nu$	Total Bkg.	Obs. Events
SRL	3.21 ± 0.42	12.6 ± 4.9	2.3 ± 2.1	0.76 ± 0.38	18.8 ± 5.3	12
SRH	0.18 ± 0.08	3.35 ± 1.05	0 ± 0.65	0.29 ± 0.15	3.82 ± 1.25	2

For the high mass region, 3.63 ± 0.75 (stat.) ± 0.99 (syst.) events are expected, and 2 are observed. The breakdown of the contributions to this background are shown in Table 10.31. Plots of the variables $E_{\mathrm{T}}^{\mathrm{miss}}$, H_{T}, M_{T}, and $\Delta\phi_{\mathrm{min}}$ are shown for the high mass signal region in Figure 12.2.

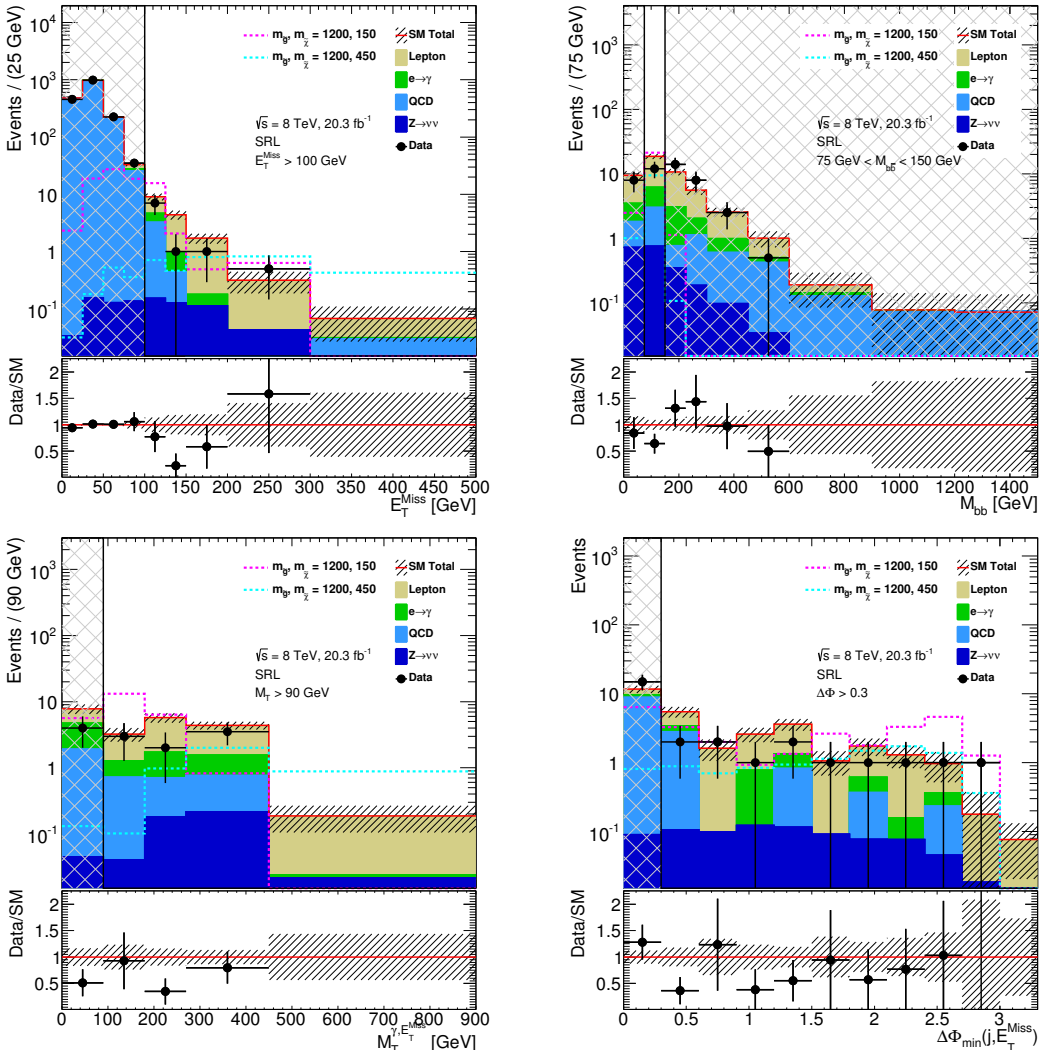

Figure 12.1: Predicted SM backgrounds and observed events for the low mass signal region in $E_{\mathrm{T}}^{\mathrm{miss}}$ (upper left), $M_{b\bar{b}}$ (upper right), M_{T} (lower left), and $\Delta\phi_{\mathrm{min}}$ (lower right). The signal region is unshaded in each histogram.

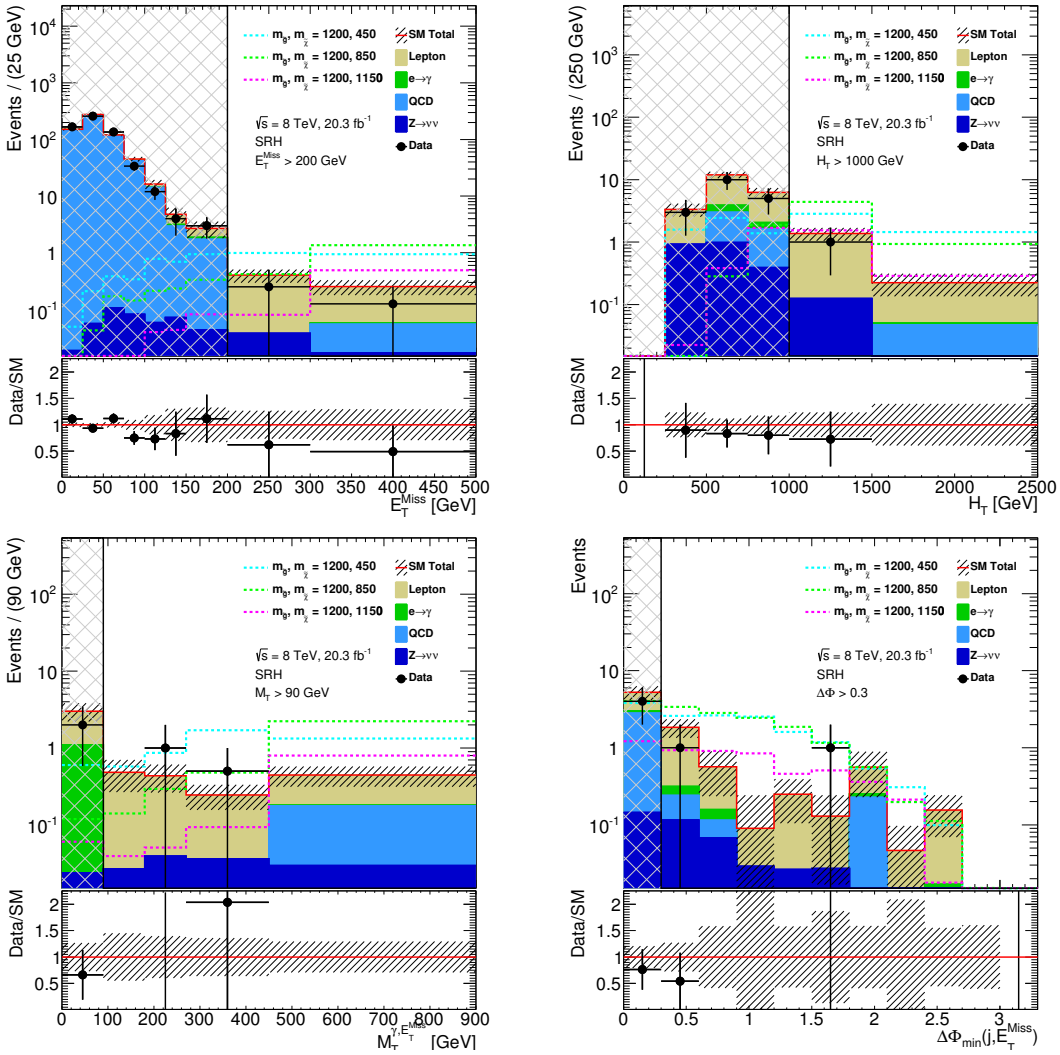

Figure 12.2: Predicted SM backgrounds and observed events for the high mass signal region in $E_{\mathrm{T}}^{\mathrm{miss}}$ (upper left), H_{T} (upper right), M_{T} (lower left), and $\Delta\phi_{\mathrm{min}}$ (lower right). The signal region is unshaded in each histogram.

12.2 Interpretation

This section discusses the interpretation of the experimental results in terms of the GGM scenario investigated in this analysis. As discussed in the previous section, no excess is observed in either of the signal regions relative to the predicted Standard Model background. The frequentist CL_s limit setting technique [77] is used to interpret the results. Upper limits are set on the number of non-SM events and visible cross section, and lower limits are set on the supersymmetric particle masses.

Details of the limit setting formalism are presented in Section 12.2.1. The upper limit on the number of non-SM events is presented in Section 12.2.2. Finally, the GGM mass exclusion limits are presented in Section 12.2.3.

12.2.1 Limit Setting Formalism

The CL_s method is based upon a profile likelihood ratio technique. The likelihood function is written as

$$L(n|\mu,\sigma) = P_{\text{signal}} \times P_{\text{syst}} = P(n_S|\lambda_S(\mu,b,\theta)) \times P_{\text{syst}}(\theta), \tag{12.1}$$

where P_{signal} is a Poisson distribution representing the signal and P_{syst} is a probability distribution incorporating the systematics. In the expression for P_{signal}, n_S is the observed number of signal events, μ defines the hypothesized signal strength (0 for a background only fit and 1 for a signal+background fit), b is the expected number of background events, and θ are the nuisance parameters from various systematic uncertainties. This distribution represents the likelihood of observing n_S, based on a Poisson distribution with expected mean λ_S.

It is assumed that there are no correlations between the various components of systematic uncertainties and thus use a simple product of gaussians to estimate $P_{\text{syst}}(\theta)$:

$$P_{\text{syst}}(\theta^0, \theta) = \prod_{j \in SU} G(\theta_j, \theta_j^0, \sigma_j), \tag{12.2}$$

where θ_j^0 and σ_j are the mean and estimated standard deviation, respectively, of the jth systematic uncertainty. The various systematic uncertainties considered have been discussed in Chapters 10 and 11, with data-driven background uncertainties described in the former and experimental and theoretical uncertainties described in the latter. Note that the signal uncertainties, in general, vary across the GGM grid and are taken into account properly for each point in the grid.

In order to extract a limit from this likelihood function, a large number of toy Monte Carlo pseudoexperiments are thrown. For each toy experiment, the value $\hat{\mu}$ that maximizes the likelihood function is found, taking the nuisance parameters θ as free parameters of the fit along with a fixed signal strength μ. The one-sided test statistic q_μ of a single test is approximated by a χ^2 function. If the approximation is not perfect, toys are needed to compute the final p-value. The p-value of the full set of toy experiments is computed from the test statistic q_μ of a single toy experiment:

$$p = \int_0^{q_{\text{obs}}} f(q_\mu | \mu, b, \hat{\hat{\theta}}) dq_\mu, \tag{12.3}$$

where $f(q_\mu | \mu, b, \hat{\hat{\theta}})$ is the distribution of q_μ and q_{obs} is the q-value of the observed dataset. A test statistic of $p = 0.05$ corresponds to a 95% CL exclusion of the new physics model represented by a specific grid point.

The p-value p' in the CL_s method is obtained with the equation

$$p' = \frac{p_{s+b}}{1 - p_b}, \tag{12.4}$$

where p_{s+b} is the p-value of the signal plus background hypothesis and p_b is the p-value of the background-only hypothesis.

12.2.2 Upper Limit on the Number of Non-SM Events

Table 12.2 shows the expected and observed limits on the number of beyond-the-SM events, using the frequentist CL_s approach with 5000 toy MC experiments. This calculation includes no signal uncertainties except for luminosity, and thus the 95% confidence-level upper limits on the number of signal events is a model independent result. Also shown are the one and two standard deviation ranges, and the 95% confidence-level upper limits on the visible cross section, derived by simply dividing the number of event limits by the integrated luminosity.

Table 12.2: Expected and observed limits on the number of beyond-the-SM events, using the frequentist CL_s approach with 5000 toy MC experiments. This calculation includes no signal uncertainties other than luminosity, and thus the limits are model independent results. Also shown are the one and two standard deviation ranges and the observed 95% confidence-level upper limits on the visible cross section.

	SRL	SRH
Expected background	18.8 ± 3.7 (stat.) ± 3.9 (syst.)	3.63 ± 0.75 (stat.) ± 0.99 (syst.)
Observed events	12	2
Observed UL on non-SM events	8.06 ± 0.34	4.26 ± 0.16
Expected UL on non-SM events	11.49	5.17
Expected -1σ	8.15	4.01
Expected +1σ	16.27	7.15
Expected -2σ	6.66	3.58
Expected +2σ	21.11	10.10
Observed UL on non-SM visible cross section (fb)	0.397 ± 0.017	0.210 ± 0.008

12.2.3 GGM Mass Exclusion Limits

Figure 12.3 shows the efficiency of SRL for strong and weak productions separately in the gluino-neutralino grid. It is seen that this low mass analysis has much better efficiency for weak production, as expected. Figure 12.4 shows the overall efficiency and the total yield in the gluino-neutralino grid. The yield plot shows that the highest sensitivity will be at low neutralino masses, and a 150 GeV neutralino should be (at least) nearly ruled out.

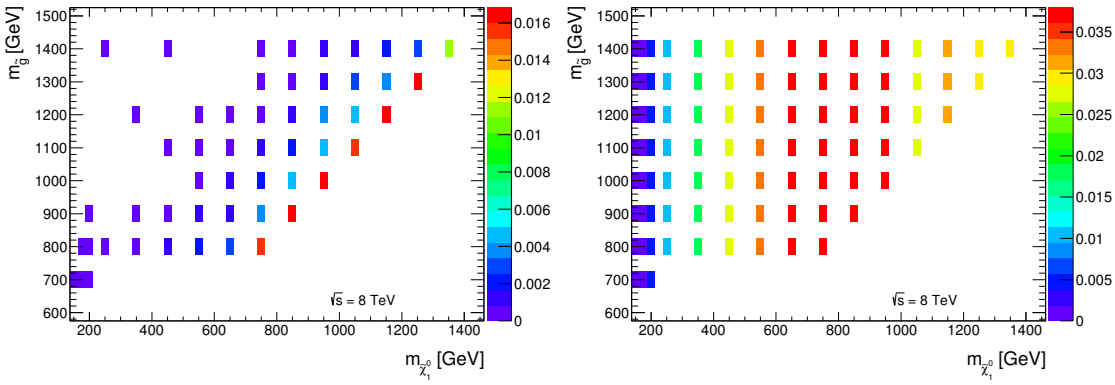

Figure 12.3: The efficiency for the low mass region for all strongly produced events at each point in the gluino, neutralino mass plane (left) and the efficiency for the low mass region for all weakly produced events at each point in the gluino, neutralino mass plane (right). For strong production, there are many points for which there are no events selected.

Figure 12.5 shows the efficiency of SRH for strong and weak productions separately in the gluino-neutralino grid. It is seen that this high mass analysis has much better efficiency for strong production, as expected. Figure 12.6 shows the overall efficiency and the total yield in the gluino-neutralino grid. The yield plot shows that the highest sensitivity will be at moderate neutralino masses, with sensitivity falling off for very high or very low mass neutralinos.

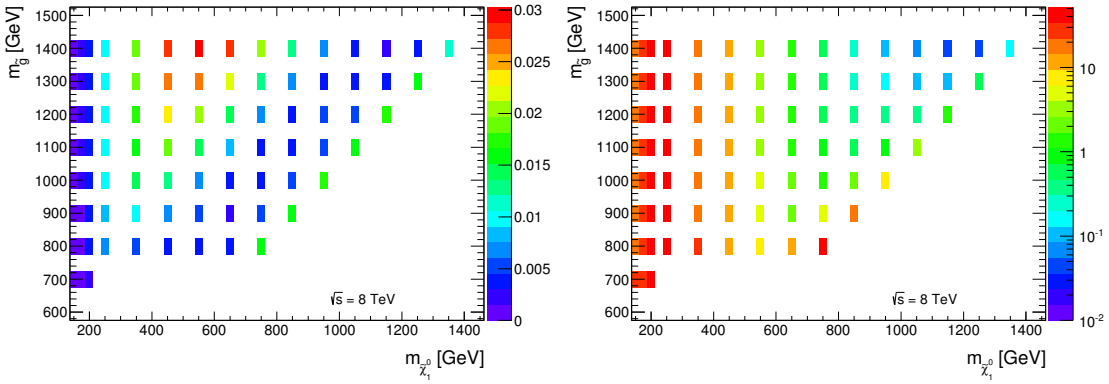

Figure 12.4: The total efficiency for the low mass region for all events produced at each point in the gluino, neutralino mass plane (left) and the total event yield for the low mass region for each point (right).

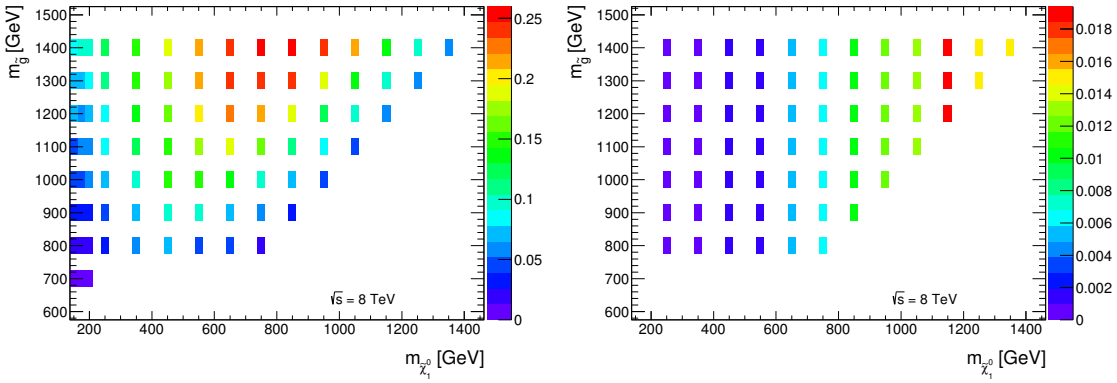

Figure 12.5: The efficiency for the high mass region for all strongly produced events at each point in the gluino, neutralino mass plane (left) and the efficiency for the high mass region for all weakly produced events at each point in the gluino, neutralino mass plane (right). For weak production, the lowest neutralino mass points ($\leq$ 200 GeV) have no events selected.

The gauge mediation signal cross sections, selection efficiencies, and background predictions are used to calculate the expected CL_s inside the SUSY `HistFitter` framework [78]. This framework implements the ATLAS recommendation for frequentist interpretation in the presence of systematic uncertainties. The configuration is a single-bin counting analysis, and the uncertainties are treated as nuisance parameters. All results are calculated in the benchmark $m_{\tilde{g}}$ vs. $m_{\tilde{\chi}_1^0}$ plane and shown as color contours to provide extra information.

Figure 12.7 shows the expected CL_s for the SRH analysis, intended to maintain sensitivity for the strong production with extra jet activity and large H_T. In all of the figures, the points with $CL_s < 0.05$ are excluded at 95% C.L. The SRH analysis has only limited expected sensitivity to weak production, but it is presented for the sake of completeness. Figure 12.8 shows the expected CL_s for the SRL analysis, intended to maintain sensitivity for the weak production mechanisms with light neutralinos and little jet activity. In contrast with the SRH analysis, the SRL analysis has only limited

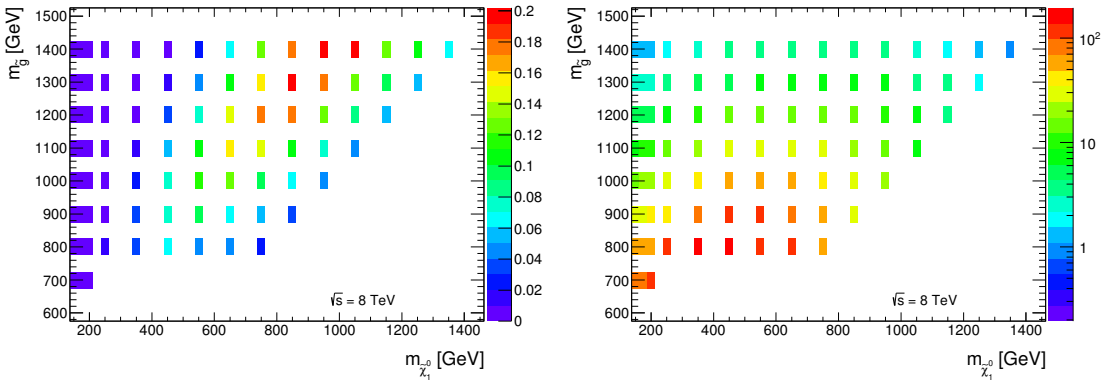

Figure 12.6: The total efficiency for the high mass region for all events produced at each point in the gluino, neutralino mass plane (left) and the total event yield for the high mass region for each point (right).

sensitivity to strong production.

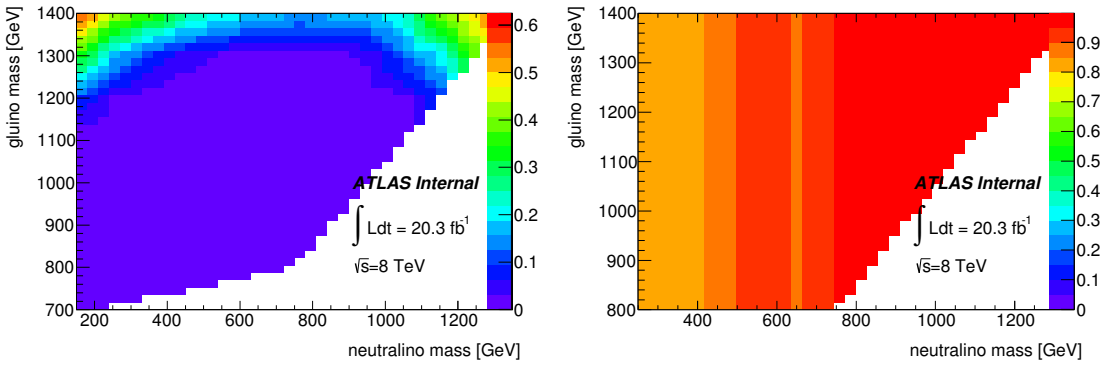

Figure 12.7: Expected CL_s contours for the SRH ("high" signal region). The expected results are shown separately for the purely strong signal production mechanism (left) and the purely weak signal production mechanism (right).

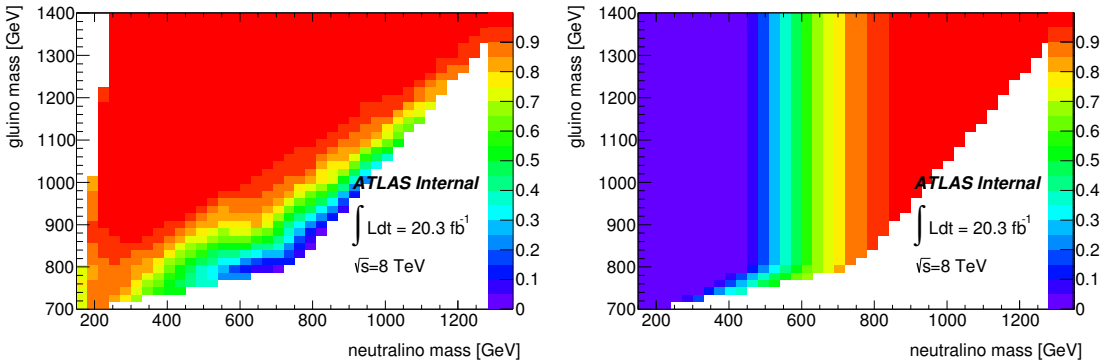

Figure 12.8: Expected CL_s contours for the SRL ("low" signal region). The expected results are shown separately for the purely strong signal production mechanism (left) and the purely weak signal production mechanism (right).

Figure 12.9 shows the expected CL_s, while Figure 12.10 shows the observed CL_s, for the SRL and SRH analyses, for all production mechanisms combined in the benchmark higgsino scenario. As designed, the analyses complement each other in the low and high neutralino mass regions, respectively. Figure 12.11 shows the expected and observed limits for the two signal regions individually. A scan over the benchmark plane is performed to find the analysis having the better expected sensitivity at each

mass point, and the resulting map, shown in Figure 12.12 is used to merge the two analysis results into a single result, shown in Figure 12.13.

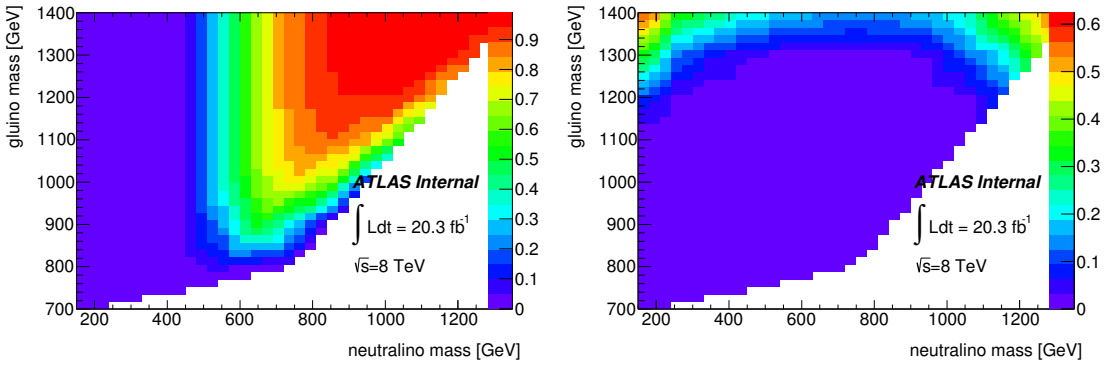

Figure 12.9: Expected CL_s contours for the SRL (left) and SRH (right) analyses. The expected 95% C.L. exclusion region can be found by following the contour corresponding to a value of 0.05.

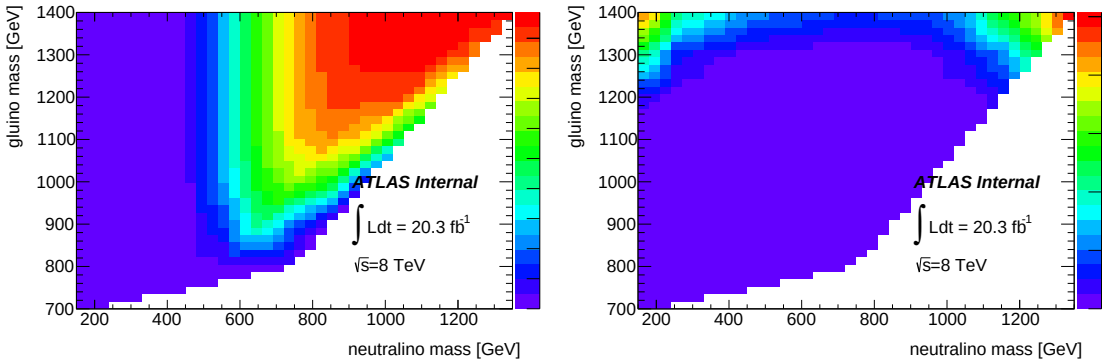

Figure 12.10: Observed CL_s contours for the SRL (left) and SRH (right) analyses. The observed 95% C.L. exclusion region can be found by following the contour corresponding to a value of 0.05 (purple bins excluded since scale is missing).

Neutralinos with mass less than 450 GeV are excluded on the basis of weak production alone. For more massive neutralinos, gluinos with mass up to 1340 GeV are excluded for neutralinos up to 950 GeV, while the sensitivity is reduced in the compressed scenario, with the limit on gluinos lowering to 1200 GeV for 1150 GeV neutralinos. These exclusions hold in the case of $m_{\tilde{g}} - m_{\tilde{\chi}_1^0} > 50$ GeV, where the event

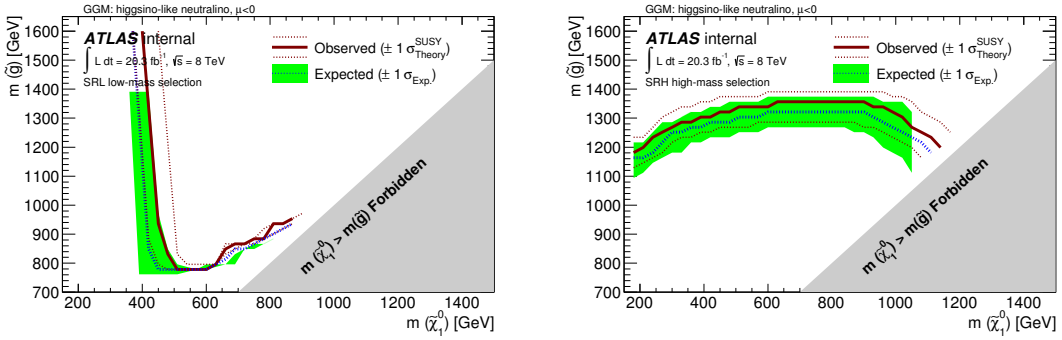

Figure 12.11: Expected (and $\pm 1\sigma$) and observed CL_s exclusion limit for the SRL (left) and SRH (right) analyses. In addition, the observed exclusion has $\pm 1\sigma$ uncertainties on the SUSY signal theory.

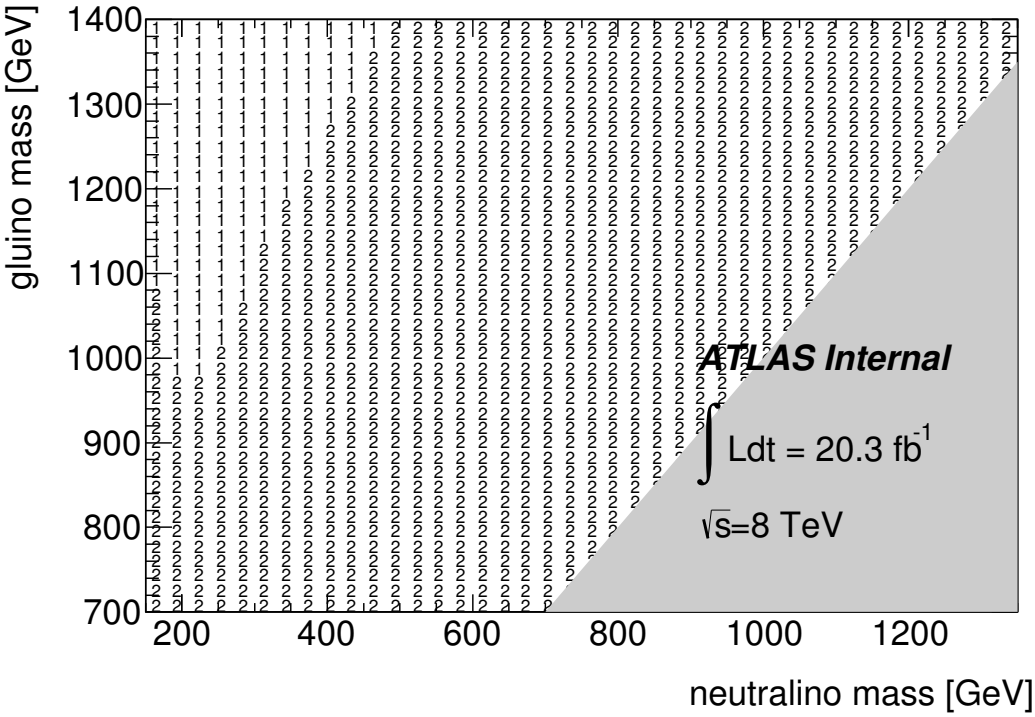

Figure 12.12: Selection of analysis for combined limit by region of the gluino grid. SRL is denoted by 1 and SRH is denoted by 2.

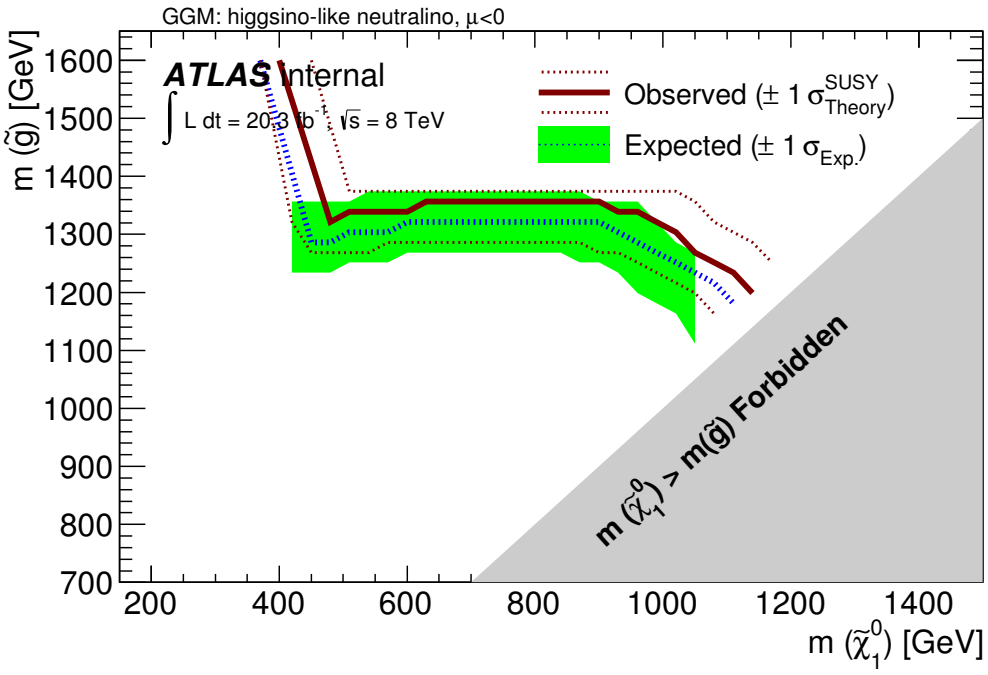

Figure 12.13: Expected (and $\pm$ 1σ) and observed CL_s exclusion limit for the merged SRL and SRH analyses. In addition, the observed exclusion has $\pm 1\sigma$ uncertainties on the SUSY signal theory.

selection efficiency is large enough to guarantee exclusion.

12.3 Conclusion

No excess over Standard Model expectations were observed in this analysis. The number of background events predicted for the two signal regions were 18.8 $\pm$ 3.7 $\pm$ 3.9 and 3.63 $\pm$ 0.75 $\pm$ 0.99 for SRL and SRH, respectively. There were 12 events observed for SRL and 2 events observed for SRH. The lack of excess was interpreted in a GGM scenario with both gluino and gaugino production processes and an NLSP neutralino that can decay to either a photon or a Higgs boson plus a gravitino. Due to the deficit of events relative to the predictions in the signal regions, the observed limits are significantly stronger than the expected limits. Gluino production is excluded with mass up to 1340 GeV for neutralinos up to 950 GeV, with reduced sensitivity at higher neutralino masses; the limit lowers to 1200 GeV for 1150 GeV neutralinos. Gaugino production is excluded for NLSP mass up to 450 GeV.

Bibliography

[1] **ATLAS** Collaboration, G. Aad *et al.*, "Observation of a new particle in the search for the Standard Model Higgs boson with the ATLAS detector at the LHC," *Phys.Lett.* **B716** (2012) 1–29, `arXiv:1207.7214 [hep-ex]`.

[2] **CMS** Collaboration, S. Chatrchyan *et al.*, "Observation of a new boson at a mass of 125 GeV with the CMS experiment at the LHC," *Phys.Lett.* **B716** (2012) 30–61, `arXiv:1207.7235 [hep-ex]`.

[3] D. Griffiths, *Introduction to Elementary Particles*. Physics textbook. Wiley, 2008.

[4] S. P. Martin, "A Supersymmetry Primer," `arXiv:hep-ph/9709356 [hep-ph]`.

[5] A. Seiden, *Particle Physics: A Comprehensive Introduction*. Addison Wesley, 2005.

[6] F. Englert and R. Brout, "Broken Symmetry and the Mass of Gauge Vector Mesons," *Phys.Rev.Lett.* **13** (1964) 321–323.

[7] P. W. Higgs, "Broken symmetries, massless particles and gauge fields," *Phys.Lett.* **12** (1964) 132–133.

[8] G. Guralnik, C. Hagen, and T. Kibble, "Global Conservation Laws and Massless Particles," *Phys.Rev.Lett.* **13** (1964) 585–587.

[9] S. Weinberg, "A Model of Leptons," *Phys.Rev.Lett.* **19** (1967) 1264–1266.

[10] A. Salam, "Weak and electromagnetic interactions," in *Elementary particle theory*, N. Svartholm, ed., pp. 367–377. Almquist & Wiksell, Stockholm, 1968.

[11] S. Glashow, J. Iliopoulos, and L. Maiani, "Weak Interactions with Lepton-Hadron Symmetry," *Phys.Rev.* **D2** (1970) 1285–1292.

[12] M. E. Peskin and D. V. Schroeder, *An Introduction to Quantum Field Theory*. Perseus Books, Cambridge, Massachusetts, 1995.

[13] **ATLAS** Collaboration, G. Aad *et al.*, "Evidence for the spin-0 nature of the Higgs boson using ATLAS data," *Phys.Lett.* **B726** (2013) 120–144, arXiv:1307.1432 [hep-ex].

[14] **ATLAS** Collaboration, G. Aad *et al.*, "Evidence for the Higgs-boson Yukawa coupling to tau leptons with the ATLAS detector," arXiv:1501.04943 [hep-ex].

[15] **CMS** Collaboration, S. Chatrchyan *et al.*, "Evidence for the direct decay of the 125 GeV Higgs boson to fermions," *Nature Phys.* **10** (2014) 557–560, arXiv:1401.6527 [hep-ex].

[16] **CMS** Collaboration, S. Chatrchyan *et al.*, "Study of the Mass and Spin-Parity of the Higgs Boson Candidate Via Its Decays to Z Boson Pairs," *Phys.Rev.Lett.* **110** no. 8, (2013) 081803, arXiv:1212.6639 [hep-ex].

[17] **Particle Data Group** Collaboration, K. Olive *et al.*, "Review of Particle Physics," *Chin.Phys.* **C38** (2014) 090001.

[18] F. Zwicky, "Die Rotverschiebung von extragalaktischen Nebeln," *Helvetica Physica Acta* **6** (1933) 110–127.

[19] D. Clowe, M. Bradac, A. H. Gonzalez, M. Markevitch, S. W. Randall, *et al.*, "A direct empirical proof of the existence of dark matter," *Astrophys.J.* **648** (2006) L109–L113, arXiv:astro-ph/0608407 [astro-ph].

[20] **WMAP Collaboration** Collaboration, G. Hinshaw *et al.*, "Five-Year Wilkinson Microwave Anisotropy Probe (WMAP) Observations: Data Processing, Sky Maps, and Basic Results," *Astrophys.J.Suppl.* **180** (2009) 225–245, arXiv:0803.0732 [astro-ph].

[21] H. Pagels and J. R. Primack, "Supersymmetry, cosmology, and new physics at teraelectronvolt energies," *Phys. Rev. Lett.* **48** (Jan, 1982) 223–226. http://link.aps.org/doi/10.1103/PhysRevLett.48.223.

[22] P. Meade, M. Reece, and D. Shih, "Prompt Decays of General Neutralino NLSPs at the Tevatron," *JHEP* **1005** (2010) 105, arXiv:0911.4130 [hep-ph].

[23] **Super-Kamiokande Collaboration** Collaboration, K. Abe *et al.*, "Search for proton decay via $p \to \nu K^+$ using 260 kiloton-year data of Super-Kamiokande," *Phys.Rev.* **D90** no. 7, (2014) 072005, arXiv:1408.1195 [hep-ex].

[24] P. Meade, N. Seiberg, and D. Shih, "General Gauge Mediation," *Prog. Theor. Phys. Suppl.* **177** (2009) 143, arXiv:0801.3278 [hep-ph].

[25] K. T. Matchev and S. D. Thomas, "Higgs and Z boson signatures of supersymmetry," *Phys.Rev.* **D62** (2000) 077702, arXiv:hep-ph/9908482 [hep-ph].

[26] **ATLAS** Collaboration, "Search for supersymmetry in events with photons, bottom quarks, and missing transverse momentum in proton-proton collisions at a centre-of-mass energy of 7 TeV with the ATLAS detector," *Phys.Lett.* **B719** (2013) 261–279, arXiv:1211.1167 [hep-ex].

[27] L. Evans and P. Bryant, "LHC Machine," *Journal of Instrumentation* **3** no. 08, (2008) S08001.

[28] M. Bajko *et al.*, "Report of the Task Force on the Incident of 19th September 2008 at the LHC," Tech. Rep. CERN-LHC-PROJECT-Report-1168, CERN, Geneva, Mar, 2009.

[29] F. Bertinelli *et al.*, "Towards a Consolidation of LHC Superconducting Splices for 7 TeV Operation," Tech. Rep. CERN-ATS-2010-144, CERN, Geneva, Jun, 2010.

[30] "LHC Commissioning with Beam." http://lhc-commissioning.web.cern.ch/lhc-commissioning/, 2015.

[31] ATLAS Collaboration, "The ATLAS Experiment at the CERN Large Hadron Collider," *JINST* **3** (2008) S08003.

[32] ATLAS Collaboration, "Luminosity Determination in pp Collisions at $\sqrt{s} = 7$ TeV Using the ATLAS Detector at the LHC," *Eur. Phys. J.* **C 71** (2011) 1630, arXiv:1101.2185 [hep-ex].

[33] S. van der Meer, "Calibration of the effective beam height in the ISR," Tech. Rep. CERN-ISR-PO-68-31. ISR-PO-68-31, CERN, Geneva, 1968.

[34] **GEANT4** Collaboration, S. Agostinelli *et al.*, "GEANT4: A Simulation toolkit," *Nucl. Instrum. Meth.* **A 506** (2003) 250.

[35] ATLAS Collaboration, "The ATLAS Simulation Infrastructure," *Eur. Phys. J.* **C 70** (2010) 823, arXiv:1005.4568 [physics.ins-det].

[36] T. Sjostrand, S. Mrenna, and P. Z. Skands, "A Brief Introduction to PYTHIA 8.1," *Comput.Phys.Commun.* **178** (2008) 852–867, arXiv:0710.3820 [hep-ph].

[37] S. Alioli, P. Nason, C. Oleari, and E. Re, "A general framework for implementing NLO calculations in shower Monte Carlo programs: the POWHEG BOX," *JHEP* **1006** (2010) 043, arXiv:1002.2581 [hep-ph].

[38] J. Ferrando and D. Wendland, "Reference $t\bar{t}$ production cross sections for use in ATLAS analyses," Tech. Rep. ATL-COM-PHYS-2014-112, CERN, Geneva, Feb, 2014.

[39] T. Sjostrand, S. Mrenna, and P. Z. Skands, "PYTHIA 6.4 Physics and Manual," *JHEP* **0605** (2006) 026, arXiv:hep-ph/0603175 [hep-ph].

[40] P. Z. Skands, "Tuning Monte Carlo Generators: The Perugia Tunes," *Phys.Rev.* **D82** (2010) 074018, arXiv:1005.3457 [hep-ph].

[41] P. M. Nadolsky *et al.*, "Implications of cteq global analysis for collider observation," *Phys. Rev.* **D 78** (2008) 013004, arXiv:0802.0007 [hep-ph].

[42] J. Alwall *et al.*, "MadGraph/MadEvent v4: The New Web Generation," *JHEP* **09** (2007) 028, arXiv:0706.2334 [hep-ph].

[43] K. Melnikov, M. Schulze, and A. Scharf, "QCD corrections to top quark pair production in association with a photon at hadron colliders," *Phys.Rev.* **D 83** (2011) 074013, arXiv:1102.1967 [hep-ph].

[44] T. HSG1 Group, "Search for ttH production in the diphoton channel with 20.3 fb-1 of data at 8 TeV," Tech. Rep. ATL-COM-PHYS-2013-866, CERN, Geneva, Jun, 2013.

[45] B. P. Kersevan and E. Richter-Was, "The Monte Carlo event generator AcerMC version 2.0 with interfaces to PYTHIA 6.2 and HERWIG 6.5," tech. rep., 2004. arXiv:hep-ph/0405247 [hep-ph].

[46] W. Kilian, T. Ohl, and J. Reuter, "WHIZARD: Simulating Multi-Particle Processes at LHC and ILC," *Eur. Phys. J.* **C 71** (2011) 1742, arXiv:0708.4233 [hep-ph].

[47] T. Gleisberg *et al.*, "Event Generation With SHERPA 1.1," *JHEP* **10** (2009) 007, arXiv:0811.4622 [hep-ph].

[48] J. T. Ruderman and D. Shih, "General Neutralino NLSPs at the Early LHC," *JHEP* **1208** (2012) 159, arXiv:1103.6083 [hep-ph].

[49] A. Djouadi, J.-L. Kneur, and G. Moultaka, "SuSpect: A Fortran code for the Supersymmetric and Higgs particle spectrum in the MSSM," *Computer Physics Communications* **176** no. 6, (2007) 426 – 455.

[50] M. Muhlleitner, "SDECAY: A Fortran code for SUSY particle decays in the MSSM," *Acta Phys.Polon.* **B35** (2004) 2753–2766, arXiv:hep-ph/0409200 [hep-ph].

[51] A. Djouadi, J. Kalinowski, and M. Spira, "HDECAY: A Program for Higgs boson decays in the standard model and its supersymmetric extension," *Comput.Phys.Commun.* **108** (1998) 56–74, arXiv:hep-ph/9704448 [hep-ph].

[52] A. Djouadi, M. Muhlleitner, and M. Spira, "Decays of supersymmetric particles: The Program SUSY-HIT (SUspect-SdecaY-Hdecay-InTerface)," *Acta Phys. Polon.* **B 38** (2007) 635, arXiv:hep-ph/0609292 [hep-ph].

[53] M. Bahr *et al.*, "Herwig++ Physics and Manual," *Eur.Phys.J.* **C 58** (2008) 639, arXiv:0803.0883 [hep-ph].

[54] W. Beenakker *et al.*, "Squark and gluino hadroproduction," *Int. J. Mod. Phys.* **A 26** (2011) 2637, arXiv:1105.1110 [hep-ph].

[55] Available at http://www.thphys.uni-heidelberg.de/.

[56] M. Kramer *et al.*, "Supersymmetry production cross sections in pp collisions at $\sqrt{s} = 7$ TeV," Tech. Rep. CERN-PH-TH-2012-163, 2012. arXiv:1206.2892 [hep-ph].

[57] M. Cacciari, G. P. Salam, and G. Soyez, "The anti-k_t jet clustering algorithm," *JHEP* **04** (2008) 063, arXiv:0802.1189 [hep-ph].

[58] W. Lampl *et al.*, "Calorimeter Clustering Algorithms: Description and Performance," Tech. Rep. ATL-LARG-PUB-2008-002, 2011.

[59] **ATLAS** Collaboration, "Jet energy measurement with the ATLAS detector in proton-proton collisions at $\sqrt{s} = 7$ TeV," *Eur.Phys.J.* **C73** (2013) 2304, arXiv:1112.6426 [hep-ex].

[60] **ATLAS** Collaboration, "Jet energy measurement with the ATLAS detector in proton-proton collisions at $\sqrt{s} = 7$ TeV," Tech. Rep. ATLAS-CONF-2010-038, 2010.

[61] ATLAS Collaboration, "Measurement of the b-tag Efficiency in a Sample of Jets Containing Muons with 5 fb^{-1} of Data from the ATLAS Detector," Tech. Rep. ATLAS-CONF-2012-043, Mar, 2012. http://cdsweb.cern.ch/record/1435197.

[62] ATLAS Collaboration, "Measurement of the inclusive isolated prompt photon cross section in pp collisions at $\sqrt{s} = 7$ TeV with the ATLAS detector," *Phys. Rev.* **D 83** (2011) 052005, arXiv:1012.4389 [hep-ex].

[63] **ATLAS** Collaboration, L. Carminati *et al.*, "Reconstruction and Identification

Efficiency of Inclusive Isolated Photons," Tech. Rep. ATL-PHYS-INT-2011-014, 2011.

[64] ATLAS Collaboration, "Electron performance measurements with the ATLAS detector using the 2010 LHC proton-proton collision data," *Eur. Phys. J.* **C 72** (2012) 1909, arXiv:1110.3174 [hep-ex].

[65] **ATLAS** Collaboration, "Measurement of the $W \to \ell\nu$ and $Z/\gamma^* \to \ell\ell$ production cross sections in proton-proton collisions at $\sqrt{s} = 7$ TeV with the ATLAS detector," *JHEP* **1012** (2010) 060, arXiv:1010.2130 [hep-ex].

[66] https://twiki.cern.ch/twiki/bin/viewauth/AtlasProtected/SusyObjectDefinitionsr17#Muons.

[67] ATLAS Collaboration, "Performance of Missing Transverse Momentum Reconstruction in Proton-Proton Collisions at 7 TeV with ATLAS," *Eur. Phys. J.* **C 72** (2012) 1844, arXiv:1108.5602 [hep-ex].

[68] G. M. Phillips, *Interpolation and approximation by polynomials*, vol. 14. Springer Science & Business Media, 2003.

[69] ATLAS Luminosity Group, "Preliminary Luminosity Determination in pp Collisions at $\sqrt{s} = 8$ TeV using the ATLAS Detector in 2012," Tech. Rep. ATL-COM-LUM-2012-013, CERN, Geneva, Nov, 2012.

[70] https://twiki.cern.ch/twiki/bin/view/AtlasProtected/PhotonID2012.

[71] https://twiki.cern.ch/twiki/bin/view/AtlasProtected/EGammaCalibrationGEO20.

[72] https://twiki.cern.ch/twiki/bin/viewauth/AtlasProtected/EfficiencyMeasurements.

[73] https://twiki.cern.ch/twiki/bin/viewauth/AtlasProtected/MCPAnalysisGuidelinesData2012.

[74] https://twiki.cern.ch/twiki/bin/viewauth/AtlasProtected/JetEtmissRecommendations2012.

[75] https://twiki.cern.ch/twiki/bin/view/AtlasProtected/METUtilSystematics.

[76] https://twiki.cern.ch/twiki/bin/view/AtlasProtected/BTaggingCalibrationDataInterface.

[77] A. L. Read, "Presentation of search results: the cl s technique," *Journal of Physics G: Nuclear and Particle Physics* **28** no. 10, (2002) 2693. http://stacks.iop.org/0954-3899/28/i=10/a=313.

[78] M. Baak, G. Besjes, D. Cote, A. Koutsman, J. Lorenz, *et al.*, "HistFitter software framework for statistical data analysis," arXiv:1410.1280 [hep-ex].

Part IV

Appendices

Appendix A

Monte Carlo Sample Details

$W/Z/\gamma$+jets samples

The details of W simulation samples used in the analysis are shown in Tables A.1,A.2, and A.3. The details of $Z \to \nu\nu$ simulation samples used in the analysis are shown in Table A.4. All samples are generated using the SHERPA generator.

Table A.1: List of $W \to e\nu$ datasets that are used for background evaluation in the analysis. All samples are generated using SHERPA. The inclusive p_{T} samples have a cut placed on the truth p_{T} of the W boson at 40 GeV to remove overlap with the other samples.

Flavor	p_{T} range [GeV]	DSID	Number of events	σ [pb]	$\int \mathscr{L} dt$ [fb^{-1}]	Fast/FullSim
B Filter	Inclusive	167740	4360265	156	28.0	Fast
C Filter, B Veto	Inclusive	167741	3045740	597	5.10	Fast
C Veto, B Veto	Inclusive	167742	27967824	11400	2.44	Fast
B Filter	40-70	180534	676639	25.0	27.1	Fast
C Filter, B Veto	40-70	180535	1144418	124	9.21	Fast
C Veto, B Veto	40-70	180536	4794822	575	8.34	Fast
B Filter	70-140	167761	427907	12.8	33.5	Fast
C Filter, B Veto	70-140	167762	692309	55.9	12.4	Fast
C Veto, B Veto	70-140	167763	3801393	209	18.2	Fast
B Filter	140-280	167770	1034032	2.18	473	Fast
C Filter, B Veto	140-280	167771	430968	7.68	56.1	Fast
C Veto, B Veto	140-280	167772	465651	24.7	18.9	Fast
B Filter	280-500	167779	20349	.169	120	Full
C Filter, B Veto	280-500	167780	41504	.478	86.8	Full
C Veto, B Veto	280-500	167781	107638	1.39	77.2	Full
B Filter	500+	167788	2022	.0113	179	Full
C Filter, B Veto	500+	167789	2044	.0274	74.6	Full
C Veto, B Veto	500+	167790	2113	.0737	28.7	Full

Table A.2: List of $W \to \mu\nu$ datasets that are used for background evaluation in the analysis. All samples are generated using SHERPA. The inclusive p_{T} samples have a cut placed on the truth p_{T} of the W boson at 40 GeV to remove overlap with the other samples.

Flavor	p_{T} range [GeV]	DSID	Number of events	σ [pb]	$\int \mathscr{L} dt$ [fb^{-1}]	Fast/FullSim
B Filter	Inclusive	167743	4356602	156	27.9	Fast
C Filter, B Veto	Inclusive	167744	2875673	518	5.55	Fast
C Veto, B Veto	Inclusive	167745	27938336	11500	2.43	Fast
B Filter	40-70	180537	675967	25.0	27.0	Fast
C Filter, B Veto	40-70	180538	1142160	120	9.49	Fast
C Veto, B Veto	40-70	180539	4791708	580	8.26	Fast
B Filter	70-140	167764	427465	12.8	33.5	Fast
C Filter, B Veto	70-140	167765	690605	55.3	12.5	Fast
C Veto, B Veto	70-140	167766	3812976	211	18.1	Fast
B Filter	140-280	167773	1033014	2.18	473	Fast
C Filter, B Veto	140-280	167774	427120	7.49	57.0	Fast
C Veto, B Veto	140-280	167775	464374	24.9	18.6	Fast
B Filter	280-500	167782	20351	0.169	120	Full
C Filter, B Veto	280-500	167783	41407	0.466	88.8	Full
C Veto, B Veto	280-500	167784	109731	1.41	78.0	Full
B Filter	500+	167791	2022	0.0113	179	Full
C Filter, B Veto	500+	167792	2038	0.0270	75.4	Full
C Veto, B Veto	500+	167793	10522	0.0744	141	Full

Table A.3: List of $W \to \tau\nu$ datasets that are used for background evaluation in the analysis. All samples are generated using SHERPA. The inclusive p_{T} samples have a cut placed on the truth p_{T} of the W boson at 40 GeV to remove overlap with the other samples.

Flavor	p_{T} range [GeV]	DSID	Number of events	σ [pb]	$\int \mathscr{L} dt$ [fb^{-1}]	Fast/FullSim
B Filter	Inclusive	167746	4339792	156	27.9	Fast
C Filter, B Veto	Inclusive	167747	2971796	561	5.30	Fast
C Veto, B Veto	Inclusive	167748	27956488	11500	2.44	Fast
B Filter	40-70	180540	676611	25.1	27.0	Fast
C Filter, B Veto	40-70	180541	1142934	123	9.32	Fast
C Veto, B Veto	40-70	180542	4795896	577	8.31	Fast
B Filter	70-140	167767	427839	12.8	33.5	Full
C Filter, B Veto	70-140	167768	692286	55.3	12.5	Full
C Veto, B Veto	70-140	167769	3813924	210	18.2	Full
B Filter	140-280	167776	206729	2.18	94.7	Full
C Filter, B Veto	140-280	167777	430367	7.61	56.5	Full
C Veto, B Veto	140-280	167778	465881	24.8	18.8	Full
B Filter	280-500	167785	20326	0.169	120	Full
C Filter, B Veto	280-500	167786	41462	0.475	87.3	Full
C Veto, B Veto	280-500	167787	109737	1.39	78.7	Full
B Filter	500+	167794	2022	0.0113	179	Full
C Filter, B Veto	500+	167795	2040	0.0273	74.9	Full
C Veto, B Veto	500+	167796	10624	0.0747	142	Full

Table A.4: List of $Z \to \nu\nu$ datasets that are used for background evaluation in the analysis. All samples are generated using SHERPA. The inclusive p_{T} samples have a cut placed on the truth p_{T} of the Z boson at 70 GeV to remove overlap with the other samples.

Flavor	p_{T} range [GeV]	DSID	Number of events	σ [pb]	$\int \mathscr{L}\,dt$ [fb^{-1}]	Fast/FullSim
B Filter	Inclusive	167758	6814329	197	34.6	Fast
C Filter, B Veto	Inclusive	167759	9487896	1880	5.05	Fast
C Veto, B Veto	Inclusive	167760	14019960	4630	3.02	Fast
B Filter	70-140	167806	1274123	15.7	81.2	Fast
C Filter, B Veto	70-140	167807	720752	65.7	11.0	Fast
C Veto, B Veto	70-140	167808	1276035	105	12.1	Fast
B Filter	140-280	167818	1031912	2.44	423	Fast
C Filter, B Veto	140-280	167819	445631	9.28	48.0	Fast
C Veto, B Veto	140-280	167820	700134	13.5	51.9	Fast
B Filter	280-500	167830	40657	0.165	246	Full
C Filter, B Veto	280-500	167831	53096	0.583	91.1	Full
C Veto, B Veto	280-500	167832	219647	0.768	286	Full
B Filter	500+	167842	10088	0.00964	1050	Full
C Filter, B Veto	500+	167843	10367	0.0326	318	Full
C Veto, B Veto	500+	167844	42375	0.0398	1070	Full

Appendix B

Signal Contamination

B.1 Signal contamination in the lepton control region

Due to extra decay products and decay chains that do not result in the desired signature, signal events can end up in the lepton control regions and potentially reduce sensitivity. Figure B.1 shows the signal contamination in LCR5L as a fraction of the number of data events in LCR5L (left) and ratio of the additional background yield in SRL due to contamination to the predicted signal in SRL (right). Figure B.2 shows the signal contamination in LCR2H as a fraction of the number of data events in LCR2H (left) and ratio of the additional background yield in SRH due to contamination to the predicted signal in SRH (right).

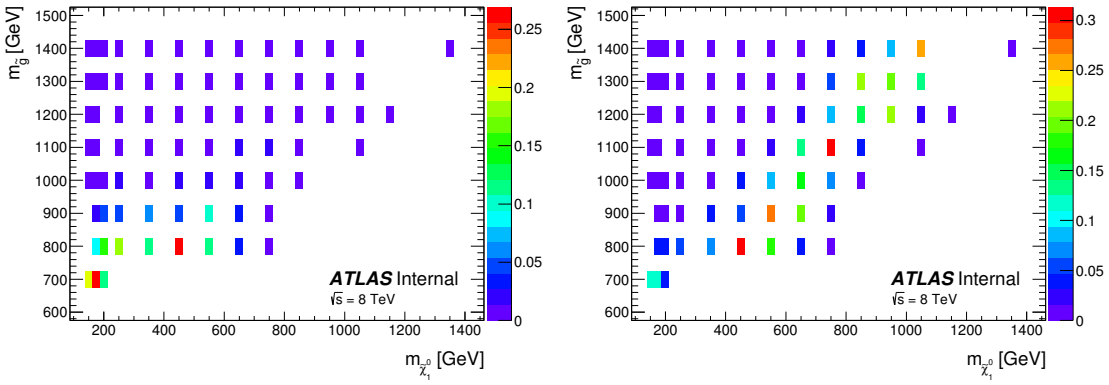

Figure B.1: The contamination as a fraction of the number of data events in LCR5L (left) and as a fraction of the number of signal events in SRL (right). The right plot applies the transfer factor calculated in Section 10.1.3.

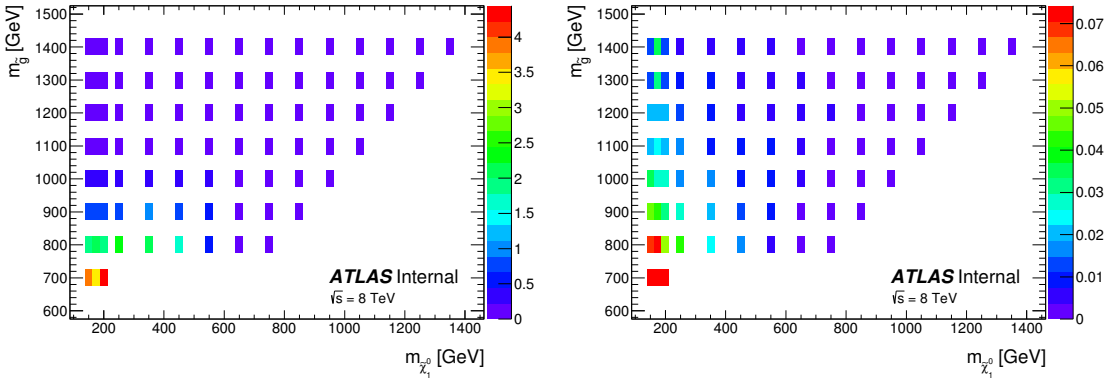

Figure B.2: The contamination as a fraction of the number of data events in LCR2H (left) and as a fraction of the number of signal events in SRH (right). The right plot applies the transfer factor calculated in Section 10.1.3.

B.2 Signal contamination in the QCD CR3 control region

Signal events can also end up in the QCD CR3 control regions due to untagged b-jets or events with no b-jets. Figure B.3 shows the signal contamination in QCR3L as a fraction of the number of data events in QCR3L (left) and ratio of the additional background yield in SRL due to contamination to the predicted signal in SRL (right). Figure B.4 shows the signal contamination in QCR3H as a fraction of the number of data events in QCR3H (left) and ratio of the additional background yield in SRH due to contamination to the predicted signal in SRH (right).

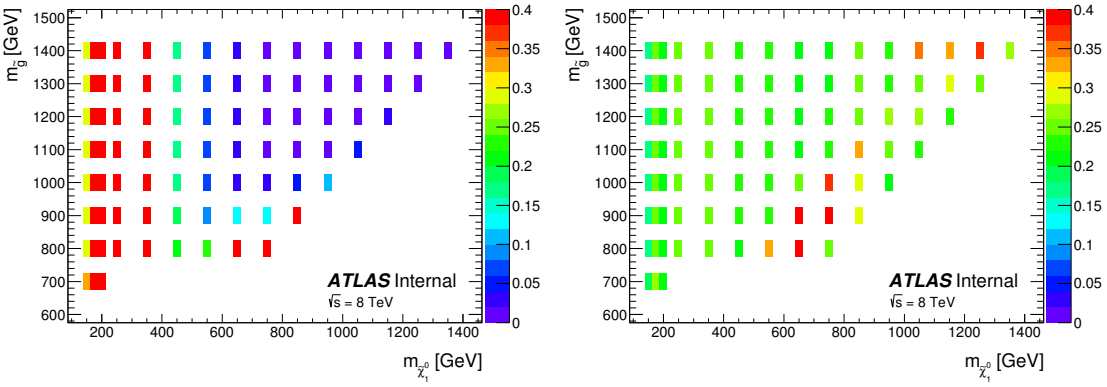

Figure B.3: The contamination as a fraction of the number of data events in QCR3L (left) and as a fraction of the number of signal events in SRL (right). The right plot applies the scale factor and correction factor calculated in Section 10.1.4.

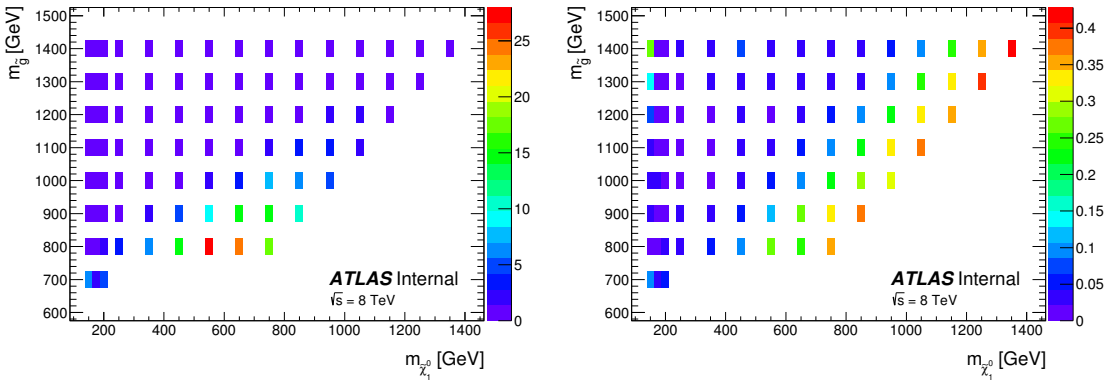

Figure B.4: The contamination as a fraction of the number of data events in QCR3H (left) and as a fraction of the number of signal events in SRH (right). The right plot applies the scale factor and correction factor calculated in Section 10.1.4.

Appendix C

Theory Systematic Uncertainties

$t\bar{t}$ $+\gamma$ and $W+\gamma$ theory uncertainties

For Monte Carlo samples that figure prominently into the background calculation, it is important to understand the theoretical uncertainties that go into producing these samples. The most prominent MC samples used in the background calculation for this analysis are $t\bar{t}$ $+\gamma$ and W+γ. Other MC samples are used, but their contributions are much smaller than the aforementioned, and even with conservatively high theoretical uncertainties are insignificant. For each of these samples, uncertainties are calculated for three varied quantities as well as the PDF. These uncertainties are calculated using truth samples that do not have the full reconstruction.

For the PDF uncertainty calculation, events are reweighted using three different PDFs and the accompanying error PDFs. The three PDF sets used are CT10nlo, MSTW2008nlo68cl, and NNPDF 2.3 NLO. The uncertainty is calculated for each of the three PDFs individually, and then combined into a full uncertainty envelope. The envelope spans from the lowest of the three PDFs varied downward to the highest of the three PDFs varied upward.

C.1 $t\bar{t}$ +γ

$t\bar{t}$ +γ is used prominently in the lepton transfer factors (SRL/LCR5L and SRH/LCR2H) and the QCD control regions for the low mass region (QCR3L). In QCR3H, the b-veto limits the contribution of $t\bar{t}$ and $t\bar{t}$ +γ. Samples were generated with variations of the scale, α_s, and final state radiation. Absolute event counts/ratios for this sample in the relevant regions are shown in Table C.1. The difference with respect to the nominal sample is shown in Table C.2.

Table C.1: Event counts/ratios for the nominal and varied $t\bar{t}$ +γ samples, after each selection cut. Cut flows are shown for SRL/LCR5L, SRH/LCR2H, and QCR3L.

Sample	NoCut	Photon	Njets	BTag	Lepton	$E_{\mathrm{T}}^{\mathrm{miss}}$	M_{T}	$\Delta\Phi$	$H_{\mathrm{T}}/M_{b\bar{b}}$
SRL/LCR5L									
Nominal	1.00	1.00	1.00	1.00	0.47	0.80	0.80	0.81	0.26
scaleUp	1.00	1.00	1.00	1.00	0.50	0.83	0.79	0.76	0.26
scaleDown	1.00	1.00	1.00	1.00	0.48	0.81	0.79	0.80	0.22
alphasUp	1.00	1.00	1.00	1.00	0.48	0.86	0.88	0.88	0.30
alphasDown	1.00	1.00	1.00	1.00	0.51	0.80	0.78	0.77	0.26
moreFSR	1.00	1.00	1.00	1.00	0.49	0.87	0.86	0.86	0.30
lessFSR	1.00	1.00	1.00	1.00	0.47	0.75	0.74	0.74	0.25
SRH/LCR2H									
Nominal	1.00	1.00	1.00	1.00	1.43	0.14	0.14	0.13	0.05
scaleUp	1.00	1.00	1.00	1.00	1.45	0.13	0.14	0.13	0.05
scaleDown	1.00	1.00	1.00	1.00	1.43	0.14	0.14	0.14	0.05
alphasUp	1.00	1.00	1.00	1.00	1.43	0.14	0.14	0.13	0.04
alphasDown	1.00	1.00	1.00	1.00	1.43	0.14	0.14	0.13	0.05
moreFSR	1.00	1.00	1.00	1.00	1.44	0.14	0.14	0.13	0.05
lessFSR	1.00	1.00	1.00	1.00	1.42	0.14	0.15	0.14	0.05
QCR3L									
Nominal	200000	52183	16610	7503	2105	794	694	619	244
scaleUp	200000	51938	15982	7301	2032	771	691	623	251
scaleDown	200000	52452	17957	8202	2251	856	762	680	292
alphasUp	200000	52091	17826	7998	2244	877	777	693	258
alphasDown	200000	52019	15594	7149	1985	737	645	566	223
moreFSR	200000	52329	16992	7753	2242	836	742	662	269
lessFSR	200000	51643	15713	7082	1927	747	677	605	240

In addition, the PDF uncertainty is calculated for the $t\bar{t}$ +γ sample. The

Table C.2: Relative differences (%) between the nominal and varied $t\bar{t}+\gamma$ samples, after each selection cut. Cut flows are shown for SRL/LCR5L, SRH/LCR2H, and QCR3L.

Systematic	NoCut	Photon	Njets	BTag	Lepton	$E_{\mathrm{T}}^{\mathrm{miss}}$	M_{T}	$\Delta\Phi$	$H_{\mathrm{T}}/M_{b\bar{b}}$
SRL/LCR5L									
scaleUp	0.00	0.00	0.00	0.00	7.14	2.76	-0.80	-5.90	-2.85
scaleDown	0.00	0.00	0.00	0.00	2.84	1.42	-0.62	-1.84	-18.47
alphasUp	0.00	0.00	0.00	0.00	2.95	7.49	9.91	8.52	12.19
alphasDn	0.00	0.00	0.00	0.00	7.79	-0.50	-2.40	-4.65	-0.28
moreFSR	0.00	0.00	0.00	0.00	5.07	8.58	7.92	6.60	14.64
lessFSR	0.00	0.00	0.00	0.00	0.85	-6.04	-7.45	-9.08	-6.52
SRH/LCR2H									
scaleUp	0.00	0.00	0.00	0.00	0.81	-2.64	-0.47	5.24	7.06
scaleDown	0.00	0.00	0.00	0.00	-0.46	0.77	0.83	8.76	3.64
alphasUp	0.00	0.00	0.00	0.00	-0.58	2.38	1.72	4.77	-0.88
alphasDn	0.00	0.00	0.00	0.00	-0.57	-0.05	0.63	3.48	1.29
moreFSR	0.00	0.00	0.00	0.00	0.31	0.53	1.52	4.78	6.78
lessFSR	0.00	0.00	0.00	0.00	-0.94	5.00	4.76	9.12	17.14
QCR3L									
scaleUp	0.00	-0.47	-3.78	-2.69	-3.47	-2.90	-0.43	0.65	2.87
scaleDown	0.00	0.52	8.11	9.32	6.94	7.81	9.80	9.85	19.67
alphasUp	0.00	-0.18	7.32	6.60	6.60	10.45	11.96	11.95	5.74
alphasDn	0.00	-0.31	-6.12	-4.72	-5.70	-7.18	-7.06	-8.56	-8.61
moreFSR	0.00	0.28	2.30	3.33	6.51	5.29	6.92	6.95	10.25
lessFSR	0.00	-1.03	-5.40	-5.61	-8.46	-5.92	-2.45	-2.26	-1.64

central value with the full envelope uncertainty is shown for the two lepton transfer factors and the QCR3L region in Table C.3. The resulting relative uncertainties are very small compared to other uncertainties measured.

Table C.3: Results of the PDF uncertainty calculation for the $t\bar{t}+\gamma$ sample.

Region	CT10	MSTW	NNPDF	Full Envelope
SRL/LCR5L	0.274 ± 0.005	0.270 ± 0.002	0.271 ± 0.002	0.274 ± 0.005
SRH/LCR2H	0.045 ± 0.002	0.0445 ± 0.0007	0.0428 ± 0.0008	0.045 ± 0.003
QCR3L	237.8 ± 4.9	238.4 ± 1.9	237.1 ± 1.7	237.8 ± 4.9

C.2 W+γ

W+γ is used prominently in the calculation of the high mass lepton transfer factor (SRH/LCR2H) and in the QCD control regions for both regions (QCR3L and QCR3H). The low mass lepton transfer factor (SRL/LCR5L) is not strongly influenced by W+γ due to the double b-tag required in these regions. Samples were generated with variations of the factorization scale, the renormalization scale, and the CKKW scale. Absolute event counts/ratios for these samples in the relevant regions are shown in Table C.4. The difference with respect to the nominal sample is shown in Table C.5.

Table C.4: Event counts/ratios for the nominal and varied W+γ samples, after each selection cut. Cut flows are shown for SRH/LCR2H, QCR3L, and QCR3H.

Sample	NoCut	Photon	Njets	BTag	Lepton	$E_{\mathrm{T}}^{\mathrm{miss}}$	M_{T}	$\Delta\Phi$	$H_{\mathrm{T}}/M_{b\bar{b}}$
SRH/LCR2H									
Nominal	1.00	1.00	1.00	1.00	1.82	0.22	0.23	0.21	0.07
ckkw15	1.00	1.00	1.00	1.00	1.80	0.23	0.24	0.21	0.08
ckkw30	1.00	1.00	1.00	1.00	1.83	0.23	0.24	0.21	0.08
fac025	1.00	1.00	1.00	1.00	1.78	0.22	0.24	0.22	0.09
fac4	1.00	1.00	1.00	1.00	1.78	0.22	0.23	0.20	0.07
renorm025	1.00	1.00	1.00	1.00	1.79	0.23	0.25	0.23	0.08
renorm4	1.00	1.00	1.00	1.00	1.81	0.22	0.25	0.22	0.09
QCR3L									
Nominal	1500000	301077	226535	15264	7323	2029	1828	1380	375
ckkw15	1500000	300432	225867	15486	7430	2057	1860	1472	413
ckkw30	1500000	305294	230586	16033	7826	2178	2000	1527	449
fac025	1500000	306886	232016	15411	7412	2013	1813	1409	386
fac4	1500000	293342	219058	15387	7346	1985	1826	1393	412
renorm025	1500000	303003	228267	15928	7547	2054	1879	1467	444
renorm4	1500000	297074	222900	14941	7223	1987	1816	1406	412
QCR3H									
Nominal	1500000	166829	55154	48304	48304	3191	2804	1826	631
ckkw15	1500000	166601	56177	49227	49227	3231	2822	1838	676
ckkw30	1500000	168726	54952	48023	48023	3120	2730	1798	656
fac025	1500000	171823	57199	50224	50224	3321	2908	1869	695
fac4	1500000	161286	54609	47628	47628	3030	2673	1743	614
renorm025	1500000	168195	58567	51268	51268	3374	2959	1904	603
renorm4	1500000	164006	50617	44385	44385	2885	2534	1655	608

Table C.5: Relative differences (%) between the nominal and varied W+γ samples, after each selection cut. Cut flows are shown for SRH/LCR2H, QCR3L, and QCR3H.

Systematic	NoCut	Photon	Njets	BTag	Lepton	$E_{\mathrm{T}}^{\mathrm{miss}}$	M_{T}	$\Delta\Phi$	$H_{\mathrm{T}}/M_{b\bar{b}}$
SRH/LCR2H									
ckkw15	0.00	0.00	0.00	0.00	-1.10	3.45	2.34	2.03	0.84
ckkw30	0.00	0.00	0.00	0.00	0.75	3.19	2.77	2.66	11.22
fac025	0.00	0.00	0.00	0.00	-2.02	2.47	4.74	4.37	25.10
fac4	0.00	0.00	0.00	0.00	-2.21	-0.04	-0.43	-3.96	-9.42
renorm025	0.00	0.00	0.00	0.00	-1.25	3.92	5.08	10.42	9.61
renorm4	0.00	0.00	0.00	0.00	-0.19	2.19	8.92	5.28	17.89
QCR3L									
ckkw15	0.00	-0.21	-0.29	1.45	1.46	1.39	1.75	6.63	10.28
ckkw30	0.00	1.40	1.79	5.04	6.87	7.34	9.40	10.63	19.88
fac025	0.00	1.93	2.42	0.96	1.21	-0.79	-0.83	2.09	3.06
fac4	0.00	-2.57	-3.30	0.81	0.31	-2.17	-0.12	0.93	10.00
renorm025	0.00	0.64	0.76	4.35	3.06	1.23	2.78	6.29	18.54
renorm4	0.00	-1.33	-1.60	-2.12	-1.37	-2.07	-0.67	1.87	10.00
QCR3H									
ckkw15	0.00	-0.14	1.86	1.91	1.91	1.26	0.67	0.67	7.19
ckkw30	0.00	1.14	-0.37	-0.58	-0.58	-2.23	-2.62	-1.54	3.98
fac025	0.00	2.99	3.71	3.98	3.98	4.07	3.73	2.35	10.16
fac4	0.00	-3.32	-0.99	-1.40	-1.40	-5.05	-4.66	-4.55	-2.68
renorm025	0.00	0.82	6.19	6.14	6.14	5.73	5.54	4.27	-4.42
renorm4	0.00	-1.69	-8.23	-8.11	-8.11	-9.59	-9.61	-9.37	-3.63

In addition, the PDF uncertainty is calculated for the W+γ samples. The central value with the full envelope uncertainty is shown for high mass lepton transfer factor and both QCR3 regions in Table C.6. While these uncertainties are not as small as those measured for $t\bar{t}$ +γ, they are still small compared to other measured uncertainties.

Table C.6: Results of the PDF uncertainty calculation for the W+γ samples.

Region	CT10	MSTW	NNPDF	Full Envelope
		$W \to e\nu + \gamma$		
SRH/LCR2H	0.066 ± 0.003	0.067 ± 0.001	0.066 ± 0.001	0.066 ± 0.003
QCR3L	8.89 ± 0.37	9.02 ± 0.11	9.18 ± 0.11	8.91 ± 0.39
QCR3H	98.7 ± 5.8	96.3 ± 1.9	95.6 ± 1.6	98.7 ± 5.8
		$W \to \mu\nu + \gamma$		
SRH/LCR2H	0.053 ± 0.003	0.052 ± 0.001	0.053 ± 0.003	0.053 ± 0.003
QCR3L	4.44 ± 0.13	4.39 ± 0.05	4.56 ± 0.05	4.46 ± 0.15
QCR3H	80.9 ± 5.1	78.2 ± 1.7	77.6 ± 1.4	80.9 ± 5.1
		$W \to \tau\nu + \gamma$		
SRH/LCR2H	0.153 ± 0.006	0.151 ± 0.003	0.16 ± 0.01	0.16 ± 0.01
QCR3L	31.12 ± 0.68	31.35 ± 0.27	31.35 ± 0.41	31.12 ± 0.68
QCR3H	85.9 ± 4.7	83.3 ± 1.7	84.0 ± 1.6	85.9 ± 4.7